2008-04-01

Quantification of the Environmental Solar Ultraviolet Radiation Field at the Human Eye and the Investigation of Peripherally Focused Rays.

David P. Fleming

Technological University Dublin

School of Physics
Dublin Institute of Technology
Kevin Street, Dublin 8

Quantification of the Environmental Solar Ultraviolet Radiation Field at the Human Eye and the Investigation of Peripherally Focused Rays.

David P Fleming B.Sc. (Hons.)

April 2008

Thesis submitted for PhD examination
Dublin Institute of Technology

Supervised by

Dr. James Walsh (DIT)

Declaration

I certify that this thesis which I now submit for examination for the award of PhD, is entirely my own work and has not been taken from the work of others save and to the extent that such work has been cited and acknowledged within the text of my work.

This thesis was prepared according to the regulations for postgraduate studies by research of the Dublin Institute of Technology and has not been submitted in whole or in part for an award in any other Institute or University.

The Institute has permission to keep, or lend or to copy this thesis in whole or in part, on condition that any such use of the material or the thesis be duly acknowledged.

Signature _____ Date ____/____/____

Abstract

The increase of terrestrial solar ultraviolet radiation (UVR) due to the reduction of the ozone layer has promoted a variety of research into establishing the impact of this elevated potential dose of UVR on biological tissues. Anterior ocular tissues such as the cornea have been found to be susceptible to damage by terrestrial solar UVR and diseases such as pterygium are commonly thought to be a direct result of absorbed UVR at the nasal limbus. There is a need for more accurate quantification and localisation of incident UVR at the anterior ocular surface. A novel solar blind photodiode sensor array system has been designed, constructed and tested for this purpose. The distribution of terrestrial solar UVR across the palpebral fissure for two test subjects has been quantified for a range of head orientations under different environmental conditions. The results herein outline the protection provided by different facial anatomies and the methodology has been proven through the repeatability of measurements over a range of cardinal point orientations.

Added to the ambient terrestrial irradiance across the palpebral fissure, the phenomenon of Peripheral Light Focusing (PLF) has been investigated. Through the incorporation of modeling software and an anatomically based artificial eye, a novel fibre optic method has been developed to measure the corneal transmission *in vivo*.

Contents

Acknowledgements

I would like to start by thanking my supervisor, Dr. James Walsh for all of his support and guidance throughout the duration of my postgraduate life in DIT. Through all the ups and downs associated with a postgraduate project, I am glad to say that James has become a very good friend, and long may it last.

I would also like to thank James' wife, Dr. Judy Harmey, for the time spent in Texas over two summers. It was a great experience and I thoroughly enjoyed spending that time with both of you. We might make a return trip sometime for nostalgias sake!

To Prof. Jan Bergmanson, Mrs. Laura Koehler, Mr. Chris Kuether and all at the Texas Eye Research and Technology Center, a word of thanks for your hospitality and help during my time spent there. In particular, Prof. Bergmanson and Laura for their academic help and Peggy for the rock concerts!

I wish to extend a special word of thanks to my two good friends, Drs. Hugh Byrne and Mary McNamara from the FOCAS Institute. You have been two very good friends to me throughout my decade (!) in DIT, and will be for many years to come. Thank you. Also, to the admin and tech support staff, namely Louisa and Andrew Hartnett, thanks for your ongoing help, it was much appreciated.

To Mr. Joe Keogh and Mr. James Callis, Dr. Siobhan Daly and Dr. Vincent Toal in the School of Physics, a sincere word of thanks for your input in the early stages of this project while our group was still in Room 115, the much needed lab hours and for the opportunity to carry out the research in the School of Physics respectively.

To Dr. Tony Betts, Dr. John Cassidy and Dr. Tom Cantwell, thank you for all the chats and advice towards the concluding stages of my time spent in FOCAS.

I would also like to thank two undergraduate students who assisted with this project, Dave McMahon and Joe Toomey.

To three of my very best friends, (Drs.!) Sharon, Ray and Luke, well at this stage we all finally got there. It was a slog at times, but I think we made it through pretty much unscathed! Cheers for the giggles inside and outside of DIT, I'm sure there'll be years more of them to come.

To Alanna, Dee, Dr. Mad Jim, Paddy and Jack in the Biomedical and Environmental Sensing Lab and the Alchemists next door, cheers for the much needed crack at various times, it was a pleasure to occupy the same space!

To Gav, Frank, Clodagh and Sinead, thanks for all the laughs through the ups and downs as undergrads, and to the lads for the all manner of planning during spring/summer 2008!

To Mam, Dad and Sinead, thanks for all of the love, support (in every sense of the word!) and encouragement during my time in DIT. I reckon you thought it might never end! None of it would have been possible without you.

And finally, to my dear wife, Dr. Christine O' Connor. What can I say? Above all, you have made the biggest impact on me receiving this Doctorate. Without your ongoing encouragement, I could have fallen very short of the mark, so thank you from the bottom of my heart. Hopefully it will stand to us in years to come.

Chapter 1

Environmental Ultraviolet Radiation and The Eye

1.1 Introduction

As one of our primary senses, vision is crucial to our everyday activities and one which is often taken for granted. The nature and enjoyment of outdoor activities can prove harmful over prolonged periods of time to both the skin and ocular tissues. Only over the last number of decades, with the thinning of the ozone layer, have people been made aware of the perils of non-ionising solar radiation and in particular short wavelength ultraviolet radiation (UVR)[1]. A UV index (UVI) forecast, based on the human erythemal action spectrum, was introduced by the World Health Organisation (WHO) in 1995 so that the public could easily discriminate between safe and acceptable ambient insolation, on a day to day basis, for a particular region through circulation in the local media. With the primary concern being skin cancer rates and an established global industry dealing in cosmetic products and UVR-blocking skin care ranges, by comparison very little information outlining solar UVR induced pathologies of the ocular surface is easily accessible to many societies. One of the most effective ways for blocking terrestrial UVR incident at the eye is to wear UVR-blocking contact lenses, but unfortunately such protection is inaccessible to many for socioeconomic and geographical reasons. Although increasingly researched over the last three decades, the incidence and effect of solar radiation at the ocular surface have not been as widely acknowledged or disseminated as the insidious

dangers the skin faces as a result of UVR exposure, such as, the erythemogenic dangers of solar radiation, premature skin-aging, wrinkling and cancer. As a result of this, many populations around the globe are unaware of the ocular dangers posed by UVR and the subsequent damage it can cause, some cases even resulting in irreversible blindness. In a survey sponsored by Transitions Optical Inc. in 2002, results showed that only 6 % of Americans randomly sampled knew of the ocular threat posed by UVR, as compared to 79 % with awareness of the link between skin cancer and UVR[2 3]. Although the pathogeneses of many ocular conditions have not been completely elucidated, UVR absorption by ocular tissues has been implicated through strong epidemiological and clinical evidence as a causative agent in a host of acute disorders such as, photokeratoconjunctivitis and chronic conditions due to extended exposure including pterygium, pingueculum, cataracts, limbal tumours and to a lesser extent, ocular melanomas[4 5 6 7 8 9 10 11 12 13 14 15 16 17 18 19].

The need to gain a fundamental understanding of the solar UVR field at the human eye and the physiological and environmental factors that influence the overall irradiance (W m^{-2}) variations at the anterior tissues is paramount in influencing the design, construction and testing of preventative methods such as contact lenses or other UVR absorbing eyewear. The aim of the research presented here was to demonstrate the first real-time quantification of the UVR field at the human eye in the field for a range of solar angles, environmental conditions and head orientations. The predilection of solar UVR induced ocular diseases to certain portions of the eye can be investigated more thoroughly and

with greater efficiency using a purpose designed and constructed solar blind photodiode sensing array. By doing so, the incidence of terrestrial solar UVR at the anterior ocular tissues, namely the cornea, conjunctiva and sclera, for these orientations and environmental conditions could be quantified in terms of assessing the irradiance across the horizontal lid margin. It has been noted that many anterior ocular manifestations, such as pterygium, occur at the nasal aspect more so than the temporal one[20 21]. As can be expected, varying environmental conditions, such as solar zenith angle (SZA), which is the angle between the zenith and the position of the sun, and highly variable cloud cover, have profound effects on the distribution of solar UVR across the palpebral fissure. Clear skies result in direct solar rays being incident at the anterior ocular surface, and as such, the main determinant in the spread of UVR across the ocular surface is the SZA. Cloudy or diffuse skies cause the ocularly incident UVR to arrive from all angles due to atmospheric scattering and should result in a more uniform distribution across the lid margin. By incorporating a novel photodiode sensor array in the field to measure the ocular irradiance, data sets are presented for different head carriages and orientations, under different atmospheric conditions, for two human test subjects and the relative nasal-temporal biases are elucidated and discussed.

Further to the distribution of solar UVR across the anterior ocular surface, aside from its role in focusing light towards the more anterior ocular structures, namely, the lens and retina, the cornea is the principle component in a phenomenon referred to as Peripheral Light Focusing (PLF). PLF occurs when environmental and physiologic factors permit radiation to strike the corneal dome

at temporally oblique angles. Such conditions can occur when the sun is low on the horizon, and a person's orientation is such that their eye is exposed to these temporally oblique rays. Depending on the temporally oblique angle of incidence at the corneal dome, solar rays can focus to a maximum intensity at the stem cell rich nasal limbus, the site of corneal regeneration[22 23]. Further still, less oblique rays can be transmitted through the cornea and reach the lens through this phenomenon. As a result of this focusing, there is a greater radiant exposure received at the nasal limbus or lens than would ordinarily be received due to normally direct or diffuse incident radiation at the hours around noon for a person standing upright. This is principally due to less anatomic shading of the anterior ocular structures when the sun is low in the sky, as the brow ridge serves to only shield the eye from direct rays originating from the sun around the hours of noon, when it is relatively high in the sky. However, when direct solar rays originate from the horizon, the cornea is completely exposed with little anatomic protection.

This thesis will outline the issues relating to the complex nature of quantification of the solar UVR field at the anterior ocular surface. The many environmental and physiological factors which influence the distribution of terrestrial solar UVR across the palpebral fissure will be outlined and a comprehensive discussion of the novel detection methods used in the field to quantify this ocular distribution is given. Specifically, it will address the distribution of solar UVR across the palpebral fissure for a range of solar zenith angles under clear and cloudy skies. An intercomparison of test subjects is also

given, highlighting the repeatability of the novel solar blind photodiode array designed, constructed and tested to quantify the ocular distribution.

Further to this, investigations of PLF through computer modelling software, in tandem with empirical measurements incorporating an anatomically modelled artificial human eye within a purposely designed *in vitro* novel fibre optic sensing system will be presented. Through development of this technique, the latter was adapted to measure the corneal transmission *in vivo*.

1.2 Solar Radiation, The Environment and The Anterior Segment

1.2.1 The Electromagnetic Spectrum

The electromagnetic radiation spectrum encompasses an extensive range of wavelengths, quantised as photons[24]. In a vacuum, all electromagnetic waves have the same velocity, $c = 3 \times 10^8$ m s^{-1}, so wavelength, λ (nm), and frequency, f (Hz), are simply related by:

$$\lambda = \frac{c}{f} \qquad \text{Eq.:1.1}$$

The energy E (J) and frequency f (Hz) of a photon can be related through a constant of proportionality known as Planck's constant, h ($6.6260755 \times 10^{-34}$ J s^{-1}):

$$E = hf \qquad \text{Eq.:1.2}$$

The sun, which can be considered a black body radiator at 5800 K, emits a spectral continuum, and at ground level, this ranges from approximately 280 nm to 4000 nm, peaking at ~ 500 nm as seen in figure 1.1. This spectral continuum has been split into three defined wavebands; the UV region (100 nm to 400 nm), the visible region (400 nm to ~ 700 nm) and the infrared region (~700 nm upwards). The Commission Internationale d'Eclairage (CIE) has subdivided UVR into three convenient photobiological wavebands which are UVC, 100 – 280 nm, UVB, 280 - 315 nm and UVA, 315 – 400 nm[25]. Slight inter-disciplinary variations of these wavebands exist, such as defining the UVB as 290 nm to 320 nm, but the CIE defined sub-wavebands are used commonly for dosimetric measurements[26] [27].

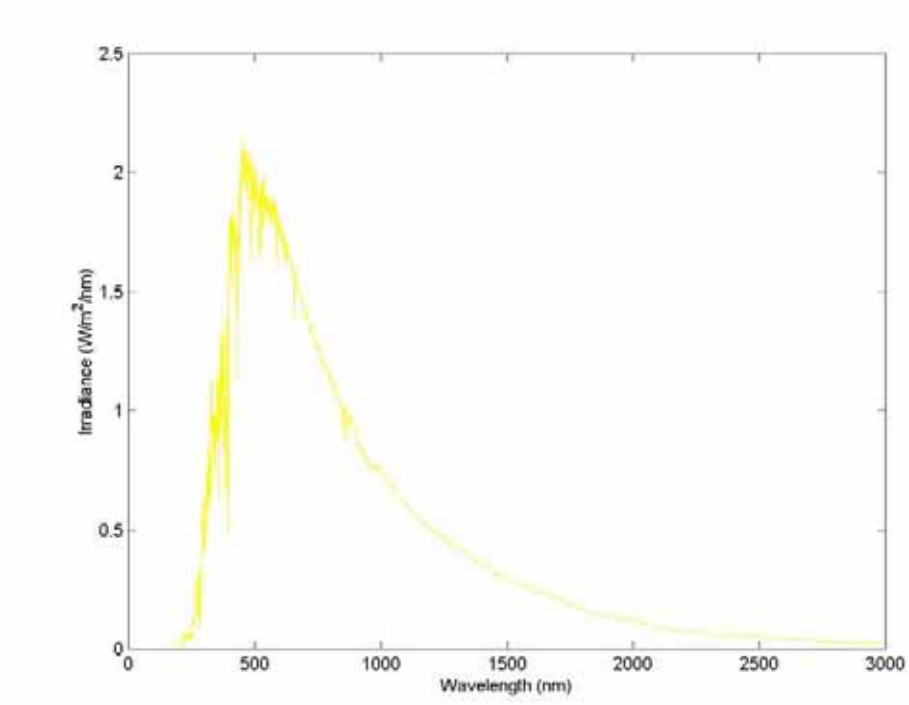

Figure 1.1:

Spectral Power Distribution of the extraterrestrial solar spectrum.

The total radiant power reaching unit area of the earth's upper atmosphere, perpendicular to the solar rays, is 1,367 W m $^{-2}$ on average[28] [29]. The solar spectral distribution is modified due to scattering and absorption by nitrogen, oxygen (O_2) and ozone (O_3) along with other absorbing particulates such as water vapour and aerosols as it passes through the atmosphere to the earth's surface[30].

The extraterrestrial solar spectrum shown in figure 1.2 highlights the relative amount of UVR with respect to the spectrally adjacent visible wavelengths, or those we perceive as 'light', beyond which the solar spectrum tails off in the adjacent infrared region. At ground level typical irradiances will be less due to absorption and scattering by the atmospheric components. From the UVR perspective, broadband absorption and specific absorption by ozone will reduce the solar irradiance to near zero below ~ 280 nm to 290 nm and the integrated irradiance in the UVA and UVB wavebands will decrease by as much as 30% from ~ 75 W m^{-2} to ~ 50 W m^{-2} for latitudes just outside the tropics (23° N and S), such as Houston, Texas (latitude: 29° 45' N) at local noon during the summer months.

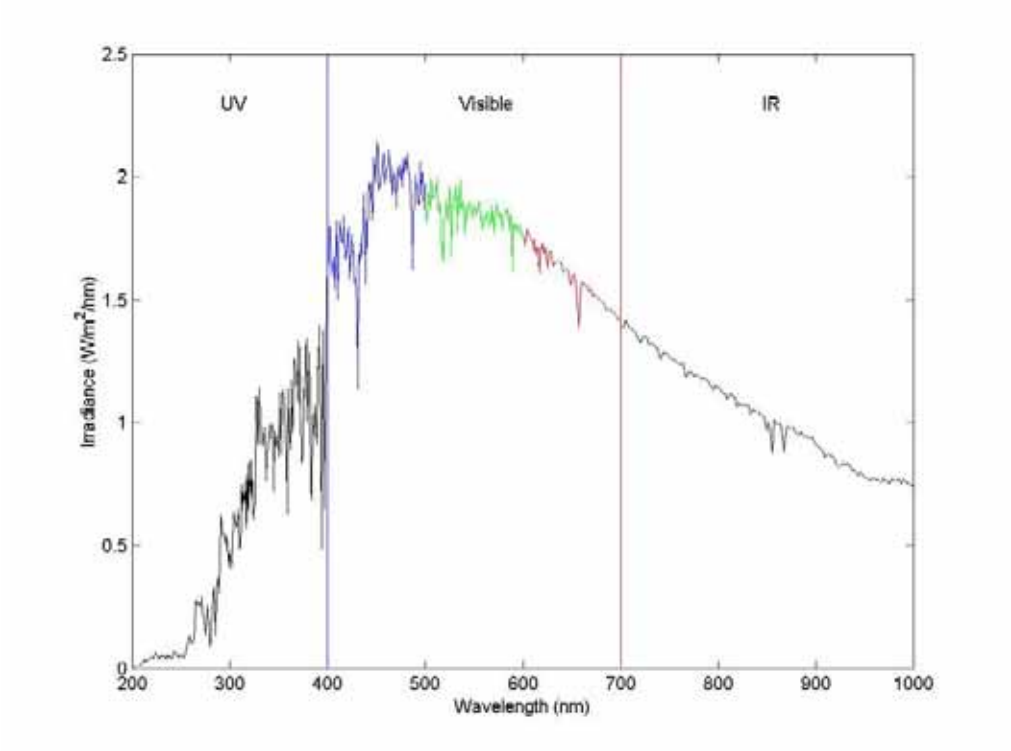

Figure 1.2:

Extraterrestrial solar irradiance highlighting UVR, visible and infrared wavebands between 200 and 1000 nm.

In terms of biological toxicity, shorter wavelength electromagnetic radiation possesses higher frequency and thus greater energy. Although there is a much greater spectral irradiance at ground level in the visible region, it is the higher energy UVR that causes most photobiological damage, comprising approximately 5 % of total terrestrial solar irradiance. Within this waveband, the most photobiologically active is the UVB, which itself comprises ~ 5 % to ~ 10 % of total terrestrial solar UVR, depending on presence and type of clouds and SZA[31 32]. In addition, the relative efficacy of shorter wavelength electromagnetic radiation in eliciting a pre-defined biological response is determined by an action spectrum, discussed in section 1.2.3[33 34] . The terrestrial UVR solar spectrum is

shown in figure 1.3 outlining the relative amounts of each UVR waveband. It must be emphasised, that there is no standard solar spectrum, as it varies with environmental factors such as season, latitude and time of day.

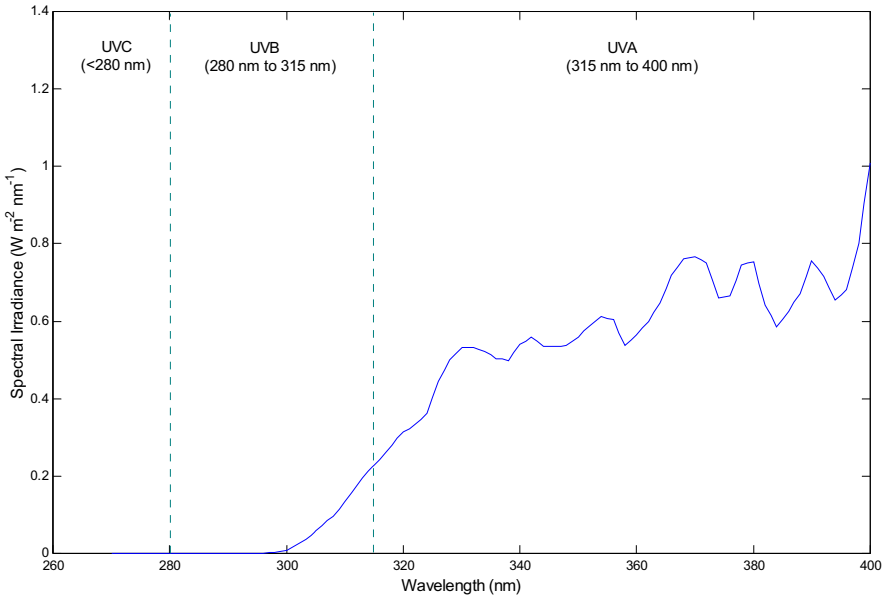

Figure 1.3:

Terrestrial Spectral Irradiance in the UVR waveband, showing typical levels of each waveband - after Diffey[35].

1.2.2 The Actinic UVR Waveband

The potential health risks of short wavelength ultraviolet electromagnetic radiation have been well documented both clinically and epidemiologically[36 37 38 39 40 41 42 43 44 45 46 47 48 49 50 51 52 53 54]. Due to the short penetration depths in skin and ocular media, ultraviolet wavelengths pose a significant risk if absorbed in sufficient quantities by exposed tissues and cause substantial photochemical and morphological changes within these tissues[55 56 57 58 59]. All three of these

sub-wavebands, UVA, UVB and UVC, are present within the extra terrestrial solar spectrum, but due to absorption by atmospheric oxygen (O_2) and ozone (O_3), the entire UVC component is blocked from the earth's surface. As a result, the most toxic wavelengths remaining at ground level are those in the UVB waveband. Due to the nature of the skin and ocular tissues response to these wavelengths, UVB radiation induces sunburn and skin pigmentation with greater efficiency than UVA, although biological effects of UVA such as skin tanning or 'melanogenesis', photoageing and ocular tissue damage should not be underestimated[60 61 62 63 64 65 66]. It has been noted that UVA penetrates the skin more deeply than UVB in the dermis and can cause greater vascular insult, while UVB is almost completely absorbed in the epidermis[67 68 69 70]. Since energy is inversely proportional to wavelength, UVB photons possess greater energy than those in the UVA and erythemal effectiveness, which is based on the skin's action spectrum, increases greatly with decreasing wavelength[71]. An action spectrum is used to describe the relative effectiveness of monochromatic light of different wavelengths in causing a pre-defined tissue response, the standard and most commonly referenced of which is the human erythemal action spectrum[72]. Indeed, the erythemal effectiveness of monochromatic UVB varies from wavelength to wavelength. It should be noted that UVA can also cause erythema effectively, but much higher radiant exposures of between 500 and 1000 times are necessary[73 74 75 76 77]. Ocular tissue action spectra are not as well established as the erythemal action spectrum discussed here. An action spectrum for photokeratoconjunctivitis was found by Pitts and Tredici and peaked at ~ 270 nm, falling off dramatically in the UVA[78]. Based on the human erythemal action spectrum and that for

photokeratoconjunctivitis, it is broadly reasonable to assume that since the ocular tissues are not as rugged as the skin, by incorporating these action spectra, and the ACGIH/ICNIRP UV action spectrum discussed in section 1.2.3, as guideline spectra relating to the biological effectiveness of UVR, one would hope to overcompensate in the pursuit of ocular protection.

The erythemogenic risk associated with solar UVR absorption is a reciprocal relationship, in that it depends on the total exposure dose delivered and absorbed by the skin which may result in sunburn, and not the dose rate. Low absorbed doses over extended periods of time will lead to the same degree of erythema or photobiological damage as high absorbed doses over shorter periods. This is known as the Bunsen-Roscoe Law and applies to the ocular tissues also[79] [80]. For complete protection from solar UVR, it is advised that sunscreens, clothing garments, sunglasses and contact lenses should contain both UVA and UVB absorbers[81]. Ideally there should be a sharp cut-off point at 400 nm for all photoprotective devices, preventing 100 % of the incident UVR from reaching all tissues, and possibly a percentage of the blue wavelengths also [82] [83] [84] [85] [86] [87] [88] [89] [90].

To standardise and raise awareness of the levels of solar UVR, the World Health Organisation (WHO), in collaboration with the World Meteorological Organisation (WMO), the United Nations Environmental Organisation (UNEP) and the International Commission on Non-Ionising Radiation Protection (ICNIRP) developed UVI measurements and forecasts to estimate and

disseminate the potential risks of solar UVR at given latitudes[91]. The dimensionless UVI is a diurnal forecast of the maximum biologically effective solar UVR in causing erythema anticipated to reach ground level at solar noon, averaged over between 10 and 30 minutes. It can range from values between 0 and ~15, where the latter would occur predominantly in the tropics under clear skies at high altitudes. By adhering to the guidelines set out in the UVI, not only is the skin afforded protection, it follows that by incorporating the recommended protection for both the skin and eyes, the ocular tissues will be safeguarded against the actinic UVR. As an internationally agreed joint recommendation of these bodies, forecasts are routinely made available through the media by meteorological agencies and are based upon burning risk for fair skinned people, thereby over-estimating the risk for people in higher skin categories[92 93 94]. Six sun-reactive skin categories have been outlined by the ICNIRP and these are[95]:

- Type I: Very fair white skin which burns but does not tan.
- Type II: White skin which burns easily and tans minimally.
- Type III: White skin which burns moderately and tans.
- Type IV: Light brown skin which burns minimally and tans easily.
- Type V: Brown skin which rarely burns; tans easily/considerably.
- Type VI: Black skin which never burns; prolifically tans.

The UVI is generally given for clear sky conditions, as there is less variability in these estimates compared to hazy or cloudy skies. The values of UVI for fair skinned people are not accurate if the forecast is incorrect regarding cloud

cover. It must also be noted that diffuse skylight can also pose a serious risk at the ocular surface in particular, as our natural aversion response and squint mechanism are disabled. Pupil constriction may also be lessened if ambient visible light levels are relatively low, allowing potentially harmful short wavelength blue radiation to pass through the crystalline lens and irradiate the retina. Exposure categories range from 'low' to 'extreme' and correspond to UVI ranges of '<2' and '11+' respectively. For the UVI range of 3-7, shade should be sought during the hours around local noon and sunscreen protection applied. For UVI values greater than 8, rigorous protection is recommended, including the use of wide-brimmed hats and UVR absorbing sunglasses/contact lenses or complete avoidance. It must be noted that the UVI represents solar erythemal induction and gives an indication of associated risk to different skin categories, and as such it does not pertain to the ocular tissues. However, due to the ocular tissues being more delicate than skin, the incorporation of UVR absorbing eyewear is implicit in the guideline for mid to extreme exposures[96 97 98 99 100]. In addition, seeking shade from direct solar rays provides less protection in the UVR than it does in the visible, so the instinctive assumption that shade reduces ambient UVR levels paralleling those in the visible can be misleading, as it only offers less protection from the direct solar rays; the scattered diffuse UVR is omnipresent[101 102].

Often given with the UVI forecast are the MED values anticipated. The unit Minimum Erythemal Dose (MED) is used widely in photobiological research and can be described as the radiant exposure of UVR which produces a barely noticeable reddening of otherwise unexposed skin with well-defined borders 24

hours after irradiation[103]. 1 MED corresponds to a radiant exposure of monochromatic radiation at the maximum spectral efficacy for erythema (~ 290 nm to ~ 300 nm), as seen in figures 1.4 and 1.5, of between approximately 150 J m^{-2} and 2000 J m^{-2} effective, depending on skin type and degree of pigmentation, since erythemal thresholds vary significantly with skin pigmentation. Values of 200 – 300 J m^{-2} effective correspond to 1 MED for white skin[104].

The discrepancy between the radiant exposures necessary to produce erythema can be attributed to variation of human skin types and, as such, has been criticised due to its variable nature of individual sensitivity. For this reason, the Standard Erythemal Dose (SED) has been proposed as a standardised measure of erythemal effective radiant exposure[105 106]. 1 SED is equivalent to a dose of 100 J m^{-2} and is weighted by the CIE erythemal action spectrum and the source's spectral power distribution[107]. It has been found that an exposure of ~ 3 to ~ 4 SED produces just minimal erythema on previously unexposed skin of type I to IV[108].

1.2.3 Action Spectra

Many environmental and physiological factors affect the distribution and receipt of solar UVR at the ocular tissues. Since UVB radiation possesses more energy per photon than UVA, it is far more detrimental to biological tissue, irrespective of the fact that UVA accounts for a much higher percentage of UVR

received at the earth's surface, although UVA can cause significant photodamage at a cellular level, and should still be considered a risk factor. As stated earlier, the ideal protection from terrestrial UVR will absorb all wavelengths below 400 nm[109].

The relative effectiveness within a wavelength region of eliciting a particular biological response is known as an action spectrum with each tissue having a unique spectrum for a specific response[110 111]. The effectiveness of terrestrial solar irradiance in causing a specified biological effect, or its biologically effective irradiance (UV [BE]), can be determined once the solar spectral irradiance and the action spectrum of a specified biological response are known across a predetermined waveband[112]. Thus, the biologically effective terrestrial solar irradiance is the product of the intensity of the solar spectrum and the action spectrum in question. The area under the resultant curve is the biologically effective irradiance (UV [BE]) and may be given as:

$$UV[BE] = \int E(\lambda)\varepsilon(\lambda)d\lambda \qquad \text{Eq.:1.3}$$

where E(λ) is the spectral irradiance distribution (W m^{-2} nm^{-1}), ε (λ) is the relative effectiveness of radiant energy at that wavelength in producing the specified biological effect (unitless), or its action spectrum and dλ is the bandwidth (nm) of the measurement interval [113 114 115 116 117 118]. UV [BE] has units of W m^{-2}.

The CIE agreed what is now the standard erythemal response function, or action spectrum, first proposed by McKinlay & Diffey in 1987, which represents a person's skin response over the entire UVB and UVA bands from 280 to 400 nm, as shown in figure 1.4[119]. The data is normalised on a logarithmic scale to the most effective wavelengths, namely the UVB. As shown, the shorter wavelength UVB radiation is significantly more effective in inducing erythema, with this effectiveness falling off towards longer UVB wavelengths and through the UVA waveband[120] [121]. The erythemal effect of UVA should not be under-estimated though, as it can be as high as ~ 40%[122] and the terrestrial solar irradiance levels are significantly higher in this waveband, compared to the UVB. In addition, the fact that the action spectrum changes by 3 orders of magnitude between 290 and 330 nm means that the spectral bandwidth of measurements made in this region needs to be precise as small uncertainties in wavelength can mean large changes in efficacy[123].

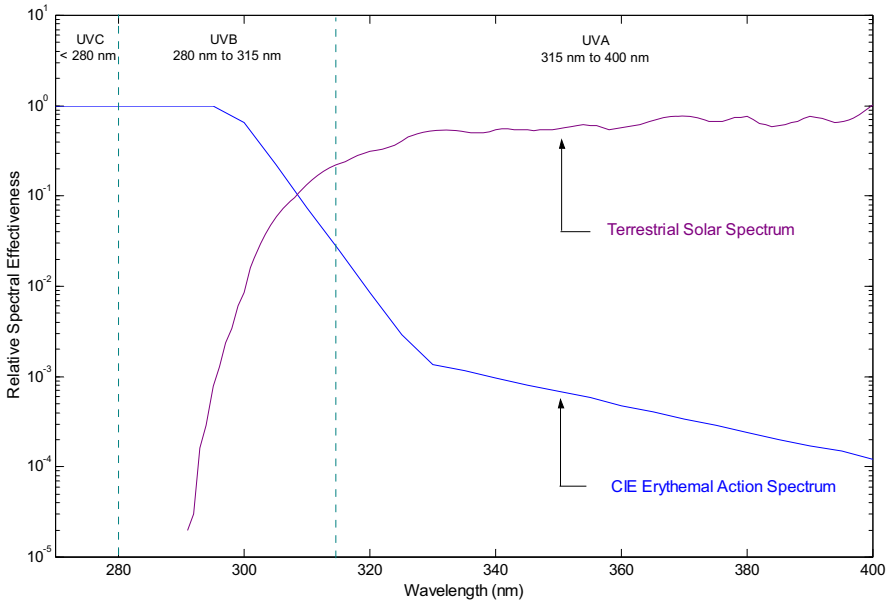

Figure 1.4:

CIE action spectrum for induced human erythema over the UVA and UVB bands and terrestrial solar spectrum[124].

A typical terrestrial solar spectrum is also shown in figure 1.4, highlighting the low relative percentage of UVB when compared to the UVA, which accounts for approximately 90 % to 95 % of the UVR at ground level. Although, accounting for only ~ 5 % to ~ 10 % of the total terrestrial UVR, it can be seen from the erythemal response that UVB is the most actinic waveband reaching ground level.

First proposed by Sliney in 1972, an envelope action spectrum combining the action spectra for skin erythema and photokeratoconjunctivitis, was later adopted and further developed by the American Conference of Governmental Industrial Hygienists (ACGIH)[125]. It is a smooth curve beneath the energies

required to cause these and other acute pathologies directly related to UVR exposure, as shown in figure 1.5[126]. Also known as the UV hazard function for evaluation of UVR sources, it highlights the UVR exposure threshold limit values recommended for protection of the skin and eyes[127 128 129 130 131].

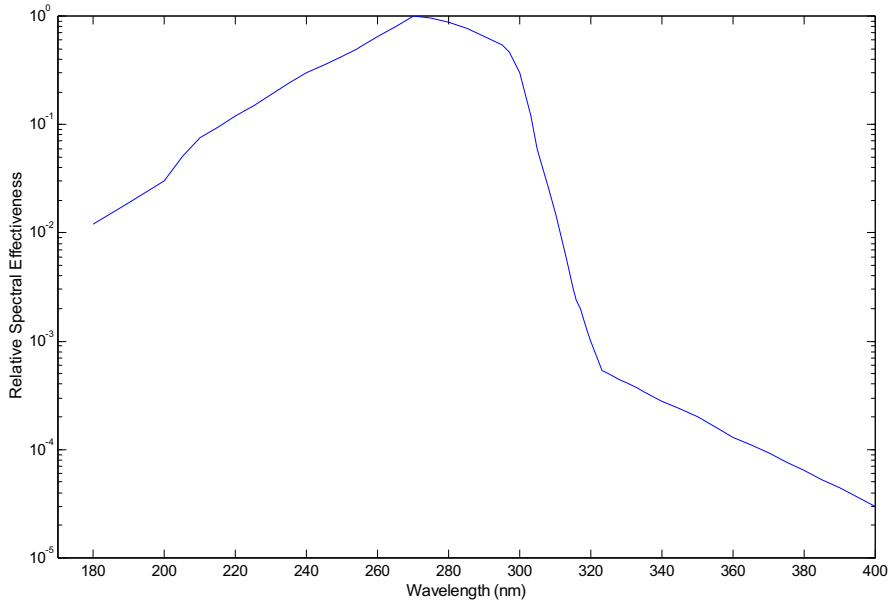

Figure 1.5:

ACGIH/ICNIRP UVR envelope action spectrum between 180 nm and 400 nm, emphasising relative exposure limits.

As an envelope spectrum of acute skin and ocular action spectrum data such as photokeratoconjunctivitis and cataract, it can be seen that similar to the CIE erythemal action spectrum, the shortest wavelength UVB wavelengths are the most effective in inducing all pathologies included under its envelope, with effectiveness falling off in the UVA[132]. Peak effectiveness was found to be ~ 270 nm to ~ 275 nm, approaching the UVB waveband. As a generic hazard function, it was later adopted as an international protection guideline by the

ICNIRP who recommend that exposure from a broadband source should not exceed 30 J m^{-2} effective over an 8 hour period[133 134 135]. This is related to MEDs in that an exposure of radiant energy at this recommended limit will result in one quarter of an MED, and no erythema should occur[136 137].

1.2.4 Factors Determining Ocular UVR Field

Individual ocular exposure to UVR can be considered to result from environmental and physiological factors. Ambient UVR levels at a given time and place depend on atmospheric and environmental conditions, and vary greatly from region to region[138]. Due to the many combined environmental and physiological variables contributing to total irradiance received by the eye, the distribution of solar terrestrial UVR across the lid margin is a significant challenge to quantify at a given time and location. Environmental factors include clear or cloudy skies, cloud distribution, SZA factors such as latitude, time of day and season, altitude, surface albedo, total ozone and physiological factors including facial structure, brow ridge prominence, skin colour, ocular orientation with respect to the solar rays, shading wear such as wide-brimmed hats, sunglasses and contact lenses and degree of lid opening or squint[139 140 141 142 143].

1.2.4.1 Environmental Factors

The most predictable condition for terrestrial solar irradiance is for that under clear skies, as the rays propagate through the atmosphere without being modified by cloud cover. Global insolation is the sum of the direct component and

that of the diffuse component, the latter comprising that insolation resulting from multiple cloud reflections and subsequent scatter[144]. When inhomogeneous cloud cover is present, the resultant insolation varies rapidly, both temporally and spatially, and is much more complex to quantify in terms of ocular receipt of solar UVR. It follows that under clear sky insolation, the distribution of ocular UVR will be highly dependent on SZA and cardinal point orientation and should result in a bias of UVR across the eye. Under cloudy skies, the spread of UVR across the ocular surface should be more uniform as UVR rays are incident from all angles. For this reason, it may be considered more challenging to reduce the irradiance at the ocular surface under diffuse insolation, than for that under direct insolation[145].

Under both clear and cloudy skies, environmental factors determining the spectral irradiance at the earth's surface are highly variable and include SZA, season, ozone column, terrain reflectivity, altitude, latitude and aerosol loading of the atmosphere[146 147 148 149]. As the SZA is the angle between the zenith and the position of the sun, with the exemption of cloud cover, it has the most profound effect on terrestrial UVR levels diurnally as the change in the relative levels of the UVR wavebands is highly dependent on the pathlength of atmosphere the rays must traverse to reach ground level[150].

1.2.4.1.1 Solar Zenith Angle

The solar zenith angle is the angle between the local vertical and the position of the sun in the sky. Directly related to latitude, season, and time of day, SZA is the most predictable influence on the spectral shape and intensity of the terrestrial solar spectrum[151 152]. To define the position of the sun in the sky, both the SZA and the Solar Azimuth (SA) coordinates are necessary. While SZA defines the position of the sun with respect to the local vertical, SA defines the position the sun is in the sky with respect to true North. SA proceeds from 0 º due North and progresses clockwise to 359 º due North. As one of the main determinants of UVB radiation at the earth's surface, SZA dominates the atmospheric pathlength of direct solar radiation falling upon an area on the earth's surface[153]. SZA is expressed as a value between 0° and 90°. The smaller the SZA, the higher the sun is in the sky and vice versa, i.e. SZA = 0° implies the sun is directly overhead, and occurs at local noon at the equator for both the vernal (spring) and autumnal equinoxes on March 21st and September 22nd respectively. The solar elevation angle (SEA) is another commonly used term and is essentially the same as SZA. In the case of SEA, the smaller the angle, the lower the sun is in the sky. It progresses from 0 º at the horizon to 90 º at the zenith.

At larger SZAs the solar beam irradiates a larger surface area. At such angles the air mass becomes greater than 1 and as a consequence of both factors, the direct irradiance is effectively decreased. As radiation passes through the atmosphere, it undergoes Rayleigh scattering. This elastic scattering shows a

strong wavelength dependency (λ^{-4}) and can be multi-directional, in that it can be forward-scattered and back-scattered. Scatter increases for decreasing wavelengths, giving the sky its blue colour, and so UVR is more strongly scattered than visible wavelengths[154 155]. As such, within the UVR waveband, the UVB is scattered considerably more so than the less toxic UVA[156 157]. The significance of SZA and changing irradiance with changing angle cannot be underestimated as the diffuse fraction of radiation from the sky increases with SZA[158 159]. Peak UVB exposures on earth are found in the tropical latitudes, which lie between 23° 30' north and south of the equator, during the summer months around local noon, as it is at these latitudes where the pathlength through the atmosphere is shortest and the SZA is smallest[160].

1.2.4.1.2 Cloud Cover

Another major factor, and the most unpredictable one, influencing UVR at the earth's surface is cloud cover[161]. The rapid temporal and spatial variability of cloud cover, along with the three dimensional character of cloud cover, make it an appreciably difficult environmental factor to qualify in terms of the impact such cover has at ground level[162 163]. As stated earlier, global or total terrestrial insolation may be categorised as being direct or diffuse, the former being radiation which permeates the atmosphere without being modified by cloud cover and reaches ground level freely. In the absence of cloud and particulate matter, Rayleigh scatter dominates the terrestrial solar spectrum, and as stated, is highly dependant on wavelength and SZA. With the presence of cloud and particulate

matter in the lower atmosphere, another type of scattering is introduced – Mie scattering. While Rayleigh scattering is highly wavelength dependant, giving the sky its blue colour, Mie scattering is inversely proportional to wavelength, and is caused by particulates on the order of, or larger than, the wavelength of interest. In the atmosphere, it is predominated by water vapour and aerosols and is the cause of diffuse isolation beneath cloudy skies[164]. Diffuse terrestrial insolation is more complex as the extraterrestrial direct solar rays pass through various atmospheric cloud densities and types, at each stage being reflected, redistributed and scattered before finally being received at ground level as illustrated schematically in figure 1.6[165].

In terms of determining whether or not a UVR bias exists across the human eye for an upright position fixing at the horizon under diffuse insolation, it could be hypothesised that a less dramatic bias would exist than that under direct insolation due to the radiation being received from all angles, thereby minimising shading effects of the brow ridge and the adjacent facial anatomy that occur for direct insolation. The resultant ocular UVR field at any moment is determined by the presence or absence of cloud cover and this UVR field is also linked inextricably to SZA and SA. It is a combination of these factors which determine the ocular UVR field for a fixed latitude, altitude and season. As can be seen in figure 1.6, direct solar rays are spectrally modified only by the atmosphere and reach the eye without undergoing scattering and reflections by clouds. These may be termed clear diffuse rays as, although they do undergo scattering in the atmosphere, they are not as randomly distributed as those rays passing through

clouds. Cloudy diffuse irradiance at the anterior ocular tissues firstly undergoes similar atmospheric scattering to clear diffuse rays, but also further undergoes multiple scattering and reflections through the cloud densities and results in a much more diffuse irradiance at the anterior ocular surface. Coupled to both are ground reflections which redirect direct and diffuse rays. Depending on the density and UVR reflectivity of upright or inclined surfaces in the surrounding terrain, these surfaces can play a very important role in the radiant exposure at the ocular surface. Inclusive of surface reflectivity, in terms of clear skies, these reflections will depend on surface inclination with respect to the eye, and surface finish, in terms of their being specularly or diffusely reflected. This is also the case under diffuse skies, but surface inclination and finish only serve to further enhance the diffuse nature of the receipt of ocular diffuse UVR, and would not be expected to cause as dramatic an effect at the ocular surface as specularly reflected radiation under clear skies from the surrounding terrain.

From here on ‘clear diffuse’ irradiance will be termed ‘clear’ or ‘direct’ irradiance and ‘cloudy diffuse’ irradiance will be termed ‘cloudy’ or ‘diffuse’ irradiance.

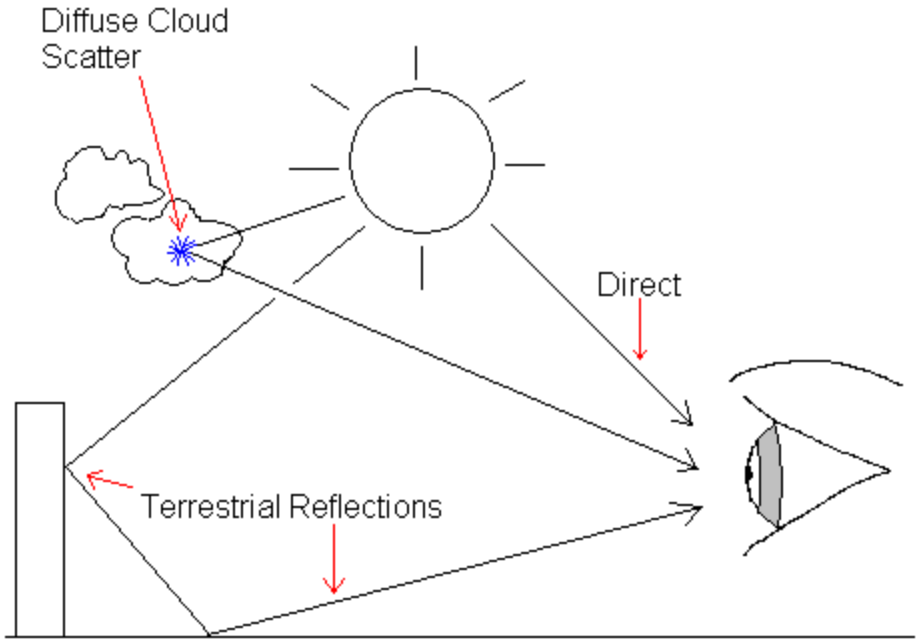

Figure 1.6:

Ocular receipt of UVR through direct, diffuse scattered and terrestrially reflected rays.

The most straightforward atmospheric condition to discuss is that of clear skies. Fluctuations of ground level irradiance are minimal for a given SZA with no cloud cover overhead and as such, the most repeatable measurements of ocular solar UVR incidence should be achievable.

Under diffuse skies, or those with perceivably constant cloud cover, similarly constant measurements should also be attainable. However, cloud cover is determined by atmospheric turbidity and local climate, and thus its temporal and spatial profile is infinitely variable, providing a greater challenge when recording UVR measurements.

One may broadly group cloud cover as follows[166]:

- Reasonably constant early morning haze which covers an observer's skyward field of view perceivably uniformly. Examples of such are the high Cirrostratus and Cirrocumulus clouds which provide little shading of the sun.
- High altitude, thin fibrous Cirrus clouds sparsely scattered across an observer's skyward field of view, not occluding the sun.
- Mid altitude Altocumulus white clouds scattered across the sky which intermittently obstructs direct rays from the sun. This type, along with Altostratus cloud cover, often appears mid-morning and early-afternoon. Such cloud cover may appear intensely white at the cloud's leading edge and can in fact possibly enhance surface irradiance momentarily.
- Low altitude, grey stratus cloud cover which appears to blanket the observable sky and which can cause dramatic fluctuations in surface irradiance. They are the lowest-forming of all clouds and may have very diffuse edges.
- Cumulus clouds which appear puffy white and are generally relatively low in altitude. When passing the sun, the surface irradiance may drop considerably, but equally, terrestrial irradiance may be enhanced depending on density and height. Similarly, low-altitude Stratocumulus clouds are patchy and can appear from bright white to dark grey. Under conditions where diffused bright white light is perceivable, enhanced terrestrial UVR may also occur.

- Cumulonimbus clouds, which appear dark and can be found at any altitude. Reaching vertical heights of thousands of meters, these are often associated with heavy showers and violent thunderstorms. As a result of their height and resultant dark bases, these essentially block all solar UVR from reaching ground level.

As mentioned above, and being strongly dependent on cloud type, height and density, a number of effects can result from the interaction of the extraterrestrial solar rays and cloud cover. Although normally such interactions cause a reducing effect, there are endlessly variable and intrinsically difficult to quantify and describe, conditions which can enhance the terrestrial UVR irradiance levels to above expected clear sky values or conversely, reduce the irradiance received[167 168 169 170]. The most influential factor in UVR enhancement is the location of the leading cloud edges with respect to the sun. Diffuse UVR irradiance can be enhanced under broken clouds when the sun is not obscured and rays are reflected by the broken cloud's leading edges[171 172 173]. Since light cloud cover is practically transparent to UVR, it can be hazardous to underestimate the levels of UVR over prolonged outdoor exposure based on the fact that the sensation of heat and visible intensity varies more significantly than UVR levels do with intermittent cloud cover[174 175 176]. It has been reported that, on average, between 30% and 50% of the total global UVB component is that of diffuse irradiance[177]. As a result, due to our natural aversion from direct sunlight, we are therefore exposed to this level of UVB irradiance unknowingly. Such diffuse exposure significantly increases our total UVR exposure, as often protective

measures are not as widely used under diffuse skies as they are under clear skies. As cloud cover is perpetually changing and modifying incident direct beam radiation, it is widely acknowledged that quantification of this variability in cloud cover and the effect it has in the field for a given application can prove very difficult[178]. The design, construction and testing of the photodiode sensor array for the research presented here aimed to make the quantification of the distribution of solar UVR at the ocular surface under both direct and diffuse skies a relatively timely, reliable and repeatable method. A major advantage in its design was its physical construction and ease of interfacing with a specifically written data acquisition program and robustness. Real time data acquisition and display on a laptop PC also aided in quick analysis of the acquired data whilst in the field, readily permitting discrimination of poor data immediately minimising the requirement for processing of information using other equipment post-acquisition. The design was such that recording and analysis of data was performed on the same laptop during measurement runs and further analysis was performed later. A problem with other dosimeter methods is that analysis is only carried out after exposure to solar irradiance and corrective measures cannot be implemented on-site.

The degree to which cloud cover can absorb, reflect or scatter radiation is a function of cloud type, density, height and the distribution of these across the observable sky. Similar to visible light, UVR is attenuated dramatically by extensive cumulonimbus dark clouds. It has been found that such clouds can attenuate UVB to approximately 1 % of clear sky levels. It has also been noted

that scattered clouds on the horizon may reduce terrestrial UVR appreciably [179] [180]. Conversely, it is also possible that low level stratus clouds or broken clouds near the sun can increase surface UV irradiance levels to higher than that of a cloudless sky due to forward reflections by cloud edges, although firm spectral dependency on such enhancement has yet to be ascertained[181] [182] [183]. As they pass closer to the sun, forward scatter and multiple reflections will increase the irradiance at ground level, momentarily increasing the diffuse component with respect to that of the direct solar component. This increased component owes itself also to the fact that a percentage of UVR striking the earth's surface is reflected skywards (depending on surface terrain reflectivity), possibly striking the base of the cloud and through this mechanism, reflecting back towards the ground, effectively reinforcing the ground level irradiance to a total irradiance exceeding a similar clear sky value[184] [185]. This scattering of radiation by diffuse clouds can also potentially increase the UVR exposure dose at different parts of the body, of particular interest here, the nose and surrounding facial features which may reflect UVR towards the ocular regions[186] [187] [188]. In general, for a clear day with direct rays arriving at the earth's surface, the head and shoulders receive the greatest amount of radiation for small zenith angles. For similar zenith angles, but with diffuse skies, the radiation is efficiently scattered across the whole sky, increasing radiation exposure to body areas which would normally not receive such exposure doses[189].

Due to global climate change, the average cloud cover on a yearly basis may be reduced in certain regions, appreciably affecting the terrestrial UVR

levels. Coupled with this is the likelihood of people spending further time outdoors pursuing recreational activities and taking holidays abroad, thereby increasing their cumulative UVR exposure. With between 65 % and 90 % of skin melanomas caused by UVR, an already increased partaking in outdoor activities and changes in head wear and hair cover, the global climate change trends indicate much higher rates than present of skin and ocular disorders in the future[190] [191]. Combining knowledge, education programmes for sun protection, individual responsibility and improving behavioural aspects towards preventive measures relating to the insidious dangers posed by terrestrial solar radiation will hopefully reduce the number of patients presenting with solar-induced pathologies of the skin and ocular media[192] [193] [194] [195] [196] [197] [198] [199] [200] [201]. The need for a better understanding of the distribution of solar UVR across the anterior ocular segment is paramount for recommending improvements in ocular protection. The research presented here provides one with a survey of the ocular distribution of terrestrial solar UVR in the field and will further enhance our understanding of the environmental and physiological variables which influence the irradiance at the ocular surface.

1.2.4.1.3 Latitude

Average ambient terrestrial solar UVR levels decrease with increasing distance from the equatorial latitudes during the year, assuming uniform ozone depth and constant altitude[202]. This is due to the equatorial latitudes having minimal air mass with respect to the direct solar rays, which is a result of the earth's axis of rotation being tilted by an angle of ~ 23.44 ° with respect to the sun[203]. Indicative of the effects of latitude and the earth's tilt is that global skin cancer rates and incidence of pterygia have been found to be among the highest globally in Australia (10° - 43° S), due to it having relatively higher levels of solar UVR throughout the year, and particularly during summer months, for its given latitude range with respect to equivalent latitudes in the Northern Hemisphere[204] [205] [206] [207]. Australia has peak summer UVI values of circa 20, which are alarmingly large by comparison with European latitudes, with peak UVI forecasts of 8-10 during the summer[208]. Due to its geographical location in the southern hemisphere, the summer months in Australia bring with them an increase of approximately 7% UVR by comparison with average levels at similar latitudes in the northern hemisphere. This can also be attributed to the fact that the southern atmosphere is cleaner and stratospheric ozone depletion has been more prevalent over the Antarctic resulting in less total ozone and thus, decreased absorption and attenuation of extraterrestrial solar UVR, resulting in an intensification of solar UVR at these southern latitudes[209] [210] [211].

1.2.4.1.4 Time of day

Between 60 % and 70 % of the daily biologically effective terrestrial solar UVR occurs two hours either side of local noon[212 213]. Diurnally, as the SZA proceeds to larger angles, pre- and post-local noon, the ratio of the UVA and UVB irradiance and the short wavelength cut-off of the terrestrial spectrum increases and decreases significantly from noon maximum also[214]. These diurnal variations are due to a longer direct pathlength and as a result of this increased pathlength, there is an increased amount of Rayleigh scattering. This can be explained in terms of 'air mass', or the amount of atmosphere the solar radiation must pass through[215].Although scattering increases with SZA and less UVR reaches ground level, forward scattering coupled with direct rays at these angles can result in a solar beam striking the temporal cornea at angles which may result in Peripheral Light Focusing effects, which will be described in detail in section 1.4.3.

1.2.4.1.5 Altitude

Solar ultraviolet levels increase with increasing altitude at a rate of approximately 3 % to 4 % for every ~300 m[216 217]. This effect is primarily due to there being less tropospheric absorption of UVR at higher altitudes than ground level due to less air mass. At small SZA's, the air mass approximates 1 at ground level and the irradiance is maximum. This occurs at local noon at a particular latitude. At the same latitude, time and SZA, but at increasing altitudes, the irradiance increases due to their being less air mass to pass through.

Similar to ground level, it is also the case that at altitudes above cloud cover, there is back-scattering of light from the upper regions of cloud cover causing a further increase in the already elevated UVR levels at a that altitude. The work detailed in later sections was performed at ground level and as such, measurement variations due to changes in altitude were an insignificant factor.

1.2.4.1.6 Season

Reasonably constant yearly averages of seasonal UVR variations exist from region to region, depending on the hemisphere. In the Northern hemisphere, terrestrial UVR irradiance increases from late spring, peaking during the middle of summer and decreases similarly towards early autumn. In the Southern hemisphere, the reverse is true; peak UVR irradiance occurs during the middle of December with irradiance decreasing through November and January. For this reason, it is vital to protect the skin and ocular tissues during peak summer months in both hemispheres around local noon.

1.2.4.1.7 Surface Albedo

Surface reflectance, or albedo, is another major determinant of ocular exposure to UVR radiation. Reflections from horizontal surfaces which are highly reflective in the ultraviolet waveband coupled with reflections from inclined surfaces effectively increase the total exposure dose a person will receive due to

the fact that UVR is now incident from above, the side and beneath[218] [219] [220]. Percentage reflectivity or 'albedo' can be broadly defined as the ratio of ambient downwelling irradiance to upwelling irradiance over a horizontal surface[221]. Since the human eye can not perceive UVR wavelengths, it is reasonable to assume that under diffuse insolation, while the squint mechanism is disabled and the pupil is relatively dilated, surfaces with high UVR albedo can only enhance the total irradiance at the ocular surface. For instance, fresh snow, with a very high blue wavelength and UVR albedo (~ 80 %), deposited on an extensive mountain range with few structures in the immediate surroundings will result in ground reflected direct rays originating from all angles[222]. Such high reflectance is a direct cause of photokeratoconjunctivitis, more commonly known as 'snow-blindness'[223]. It is an acute photochemical injury of the cornea and takes a relatively short time without protection to manifest, but symptoms generally fade between 36 to 48 hours post appearance[224] [225] [226] [227] [228] [229]. The standard preventative measure for photokeratoconjunctivitis is the use of fully wrap-around ski goggles which reduce glare and more importantly, the UVR content reaching the ocular structures. The incorporation of UV-blocking contact lenses alone or in combination with these ski goggles will also dramatically reduce the incident UVR at the anterior ocular structures. Other frequently encountered surfaces such as grass, soil and water have total UVR albedo of approximately 10 %, while dry sand and sea foam are approximately 15 % and 25 % UVR reflecting respectively[230]. In this sense, reflections from water surfaces over a defined period of time can cause a greater erythemal response than those reflections from grass for instance under similar sky conditions. Most pertinent to the work described

here is the UVR reflectance of the rooftop on which the field work was carried out. It had a UVR reflectance of approximately 5%, as measured by a broadband UVR radiometer. When compared to the other surfaces mentioned, this is a relatively low UVR surface albedo.

Another important albedo is that of human skin. Depending on skin type and colour, the percentage reflectivity from the lower brow ridge and adjacent nasal structure will vary, with some skin colours reflecting UVR from this anatomical structure more efficiently towards the nasal aspect, possibly further emphasising why many ocular conditions have a nasal predilection.

1.2.4.1.8 Ozone

The stratospheric ozone layer, stretching 10 – 50 km above the earth's surface, yet only 3 mm's thick at standard temperature and pressure (STP), contains most of the atmospheric ozone and provides a shield around the biosphere to the most toxic UVR waveband, the UVC. By absorbing all wavelengths within this waveband, the most toxic waveband reaching earth's surface is the UVB, with ozone absorption decreasing rapidly with increasing wavelength across the UVB waveband[231]. Thus, the detectable terrestrial solar spectrum begins at approximately 290 nm and increases very steeply where the ozone layer becomes completely transparent to wavelengths longer than 340 nm in the UVA waveband. Strong absorption beneath approximately 330 nm may be attributed to atmospheric ozone absorption at these wavelengths[232 233 234]. This

absorption, and thus terrestrial UVB irradiance, is highly variable and depends on stratospheric ozone thickness[235]. The strong wavelength dependency of UVB intensity at ground level on stratospheric ozone density has led to the development of a number of networks which monitor the UVR levels in both hemispheres by various methods for the reason that any destruction of atmospheric ozone enhances the UVB levels at ground level, ultimately leading to the likelihood of greater skin and ocular disease rates[236 237 238 239 240]. As has been suggested by a risk model, the incidence of cortical cataracts due to continued ozone depletion could increase by 1.3 % to 6.9 % by 2050[241].

Total ozone column is measured in Dobson units (DU) and is defined in terms of the equivalent thickness of pure ozone, the average value being about 300 DU, which, as stated, equates to approximately 3 mm of ozone at STP. This value can vary from 250 DU in the tropics to 450 DU at much higher latitudes in both hemispheres. Daily variations of ozone column are of the order of approximately 20 – 30 DU, but these are far outweighed by the seasonal and latitudinal variations that exist around the globe. The relevance of this lies in the fact that regions with lower total ozone columns will have higher levels of UVB radiation[242]. As the skin and ocular tissues are extremely susceptible to radiation damage in the UVB, any increase in terrestrial UVB will increase the incidence of related illnesses[243].

1.2.4.2 Physiological Factors

Terrestrial solar irradiance is normally expressed for a horizontal plane normal to a small SZA. However, the dose of radiation at the ocular surface is a function of the distribution of the atmospheric direct and diffuse solar components, the terrestrially reflected rays and the relative position and spatial orientation of the eye to these components. Depending on atmospheric conditions, cloud presence and density, SZA and the density of highly reflective structures in the foreground, the eye is subject to infinitely variable solar irradiance[244].

The human eye is well protected from physical insult owing to the fact that it is situated deep within a bony orbit. The protection offered to it from solar radiation by the overhang of the upper brow ridge is paramount to blocking direct rays at small SZA's, or when the sun is approximately overhead around the hours of noon. However, the extent of protection afforded by the brow ridge varies from individual to individual. Brow ridge prominence, coupled with the reflectivity of the skin, are two important factors which determine the dose received at the eye from the direct solar rays at small SZA's. In general, direct solar rays propagating at small SZA's are reflected away from or absorbed by the brow ridge before reaching the ocular tissue while standing and looking towards the horizon, a typical head carriage. A certain percentage of the incident radiation will also be reflected away by Fresnel reflection at the corneal surface, reducing the absorption by ocular tissues. The eyelids also serve to shield the delicate ocular tissues from varying degrees of direct and diffuse insult depending on ambient scene luminance. Similar to brow ridge prominence, relaxed eyelid margin

opening is individualistic and can have a marked effect on the UVR exposure dose received at the anterior surface in a diffuse environment when the instinctive squint mechanism is not enabled. This is due to the diffuse environment having a perceivably ambient scene luminance in the visible waveband, thereby minimising the effects of natural aversion, squint mechanism and pupil constriction, all of which serve to shield the ocular tissues from actinic UVR. The natural aversion of the human eye to bright areas of the sky, squint mechanism, coupled with pupil constriction and degree of lid closure, contribute largely to reducing the amount of absorbed UVR by the anterior and posterior ocular tissues respectively, from both the direct and diffuse rays[245 246 247 248 249].

The nose may also serve to shield the eye from rays reflected by the surrounding terrain, but it has been hypothesised that terrestrial reflections striking the nose and lower brow ridge may in fact be reflected back and concentrated around the nasal portion of the eye, possibly increasing the accumulative absorbed dose, and contributing to the formation of pterygia and pinguecula[250]. However, UVR selectively absorbed and transmitted by the different ocular tissues is thought to result in disorders such as pterygium, photokeratoconjunctivitis or certain types of cataract through cumulative effects. In part, it has been hypothesised that absorption of UV photons by stem cells at the limbus, a region of tissue between the corneal epithelium, conjunctival epithelium and sclera, may result in the development of pterygium[251 252 253 254].

The effects of other environmental and physiological factors such as phenotype, genotype, atmospheric aridity and turbidity, dust content etc. cannot be overlooked, but many epidemiologic studies have inferred UVR to be the only common factor between different ethnic groups, as diverse as Eskimos and Aborigines, presenting with one of the ocular conditions mentioned above[255] [256] [257] [258]. The occurrence and position of ocular UVR related disease, particularly the reported nasal bias of certain ocular pathologies, can be better understood when the ocular anatomy is considered.

1.3 Review of Ocular Anatomy

The human eye is set deeply in the orbital cavity with the upper brow ridge and eyelids providing a defence against physical injury and more appropriately here, a barrier against downwelling skylight when the head is oriented towards the horizon. The eyebrow and eyelashes serve to entrap dust particles, but also provide some additional protection against radiation striking the ocular surface by shading exposed tissues. The main ocular components that are transparent to what humans perceive as light are the cornea and conjunctiva, lens, aqueous solution and vitreous solution, and can be seen in figure 1.7. By minimising light absorbance and scattering in these tissues, maximum light transmission to the retina occurs. The other tissues presented in figure 1.7 are the limbus, sclera and iris. The limbus will be discussed in more depth in section 1.3.3.

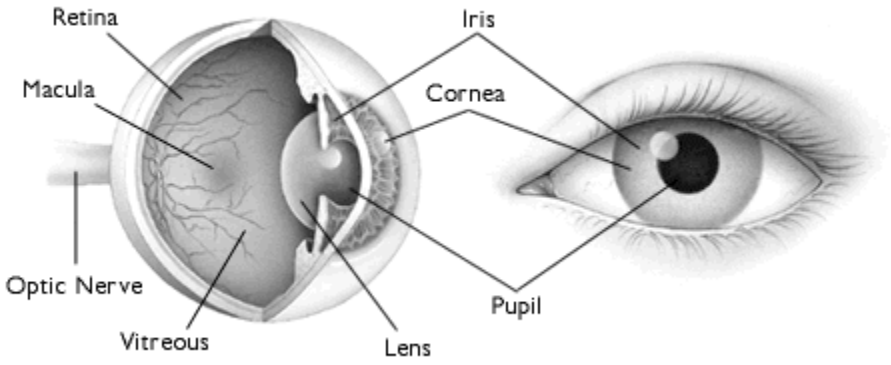

Figure 1.7:

The human eye through cross section and frontal view, showing the principal ocular components[259].

It is the cornea and the annular tissue surrounding it, known as the limbus, which were the main focus of this study. The cornea is principally involved in absorbing and transmitting incident solar UVR to more anterior tissues and is susceptible to UVR induced photobiological pathologies, including pterygium[260]. The consequences of PLF, illustrated in figure 1.8, and focusing of obliquely incident radiation at the peripheral cornea and the occurrence of such diseases as pterygium, believed to manifest at the limbal focal point, are thought to be a result of increased exposure dose received at this point.

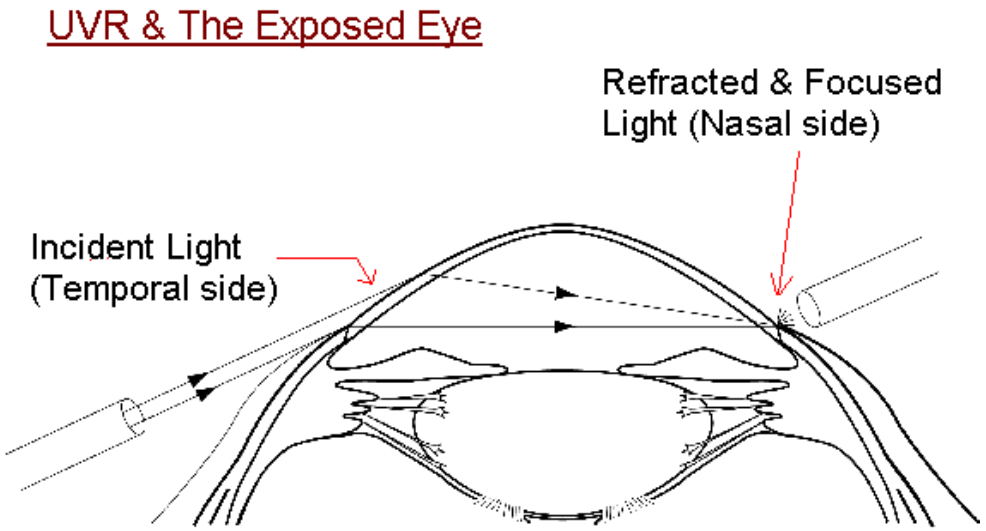

Figure 1.8:

Light delivered to temporal cornea posterior to the coronal plane and refracted to a focal point at nasal limbus.

By selective absorption of UVR wavelengths by the cornea and lens, the more posterior tissues, including the uvea and retina, receive a much lesser irradiance, as described in section 1.5.1.

1.3.1 The Cornea

The refracting power *(P)* of a spectacle or contact lens is generally given in dioptres *(D)*, as is the case with the refractive power of the cornea and human lens in optometric terms. The focusing or refractive power of a lens (m^{-1}) is

defined as the reciprocal of the focal length *(f)* in metres and is given in equation 1.4:

$$P = \frac{1}{f(m)} \qquad \text{Eq.: 1.4}$$

Due to its convex nature, and since the largest change in refractive index of the ocular system is that between air (n = 1.0003) and the anterior corneal surface (n_{cornea} = 1.376; n_{water} = 1.333), it is at this interface where most refraction occurs, providing approximately 70 %, or ~ 43 dioptres on average, of the total focusing power of the eye[261 262].

Although not insignificant, the refractive power of the cornea's posterior surface is much less (circa 10 % of anterior surface refractive power) which can be attributed to possessing a smaller radius of curvature than the anterior surface and the fact that very little refraction occurs at the posterior corneal surface since its refractive index is so closely matched to the aqueous solution ($n_{aqueous}$ = 1.336)[263]. The cornea does not have a constant radius of curvature across its diameter and flattens towards the periphery[264]. It has an average radius of curvature of 7.8 mm and 6.5 mm at the anterior and posterior surfaces respectively, with average corneal diameter of ~11.5 mm[265 266].

For the emmetropic eye, or one which forms an unaided clear image on the retina, with an average axial length of approximately 24 mm, the average dioptric

power provided is approximately 43 D of the total ~ 60 D power of the whole eye, inclusive of the lens, which contributes approximately 15 D[267 268].

Uncorrected clear image formation at the macula, better known as emmetropia, is a result of the cornea and lens structures working in unison and their combined refractive power closely matching the axial length of the eye[269]. Considerable variation exists within the emmetropic eye, with approximately 24 mm being the average axial length, as emmetropic axial lengths of between 20 mm and 30 mm are not uncommon. For those who require corrective prescriptions, by means of glasses or contact lenses, two main categories exist, myopia and hyperopia. The former will form an optical image in front of the retina due to the refractive power being too large relative to the axial length. The latter will form the same image beyond the retina due to the refractive power of the optical components being too weak with respect to the axial length.

The cornea is comprised of five adjacent tissues, each having a unique function; the epithelium (~50 μm), Bowman's membrane (~8-14 μm), stroma (~500 μm), Descemet's membrane (~5-15 μm) and endothelium (~5 μm)[270 271]. The outermost layer is the epithelium, the function of which is to protect the corneal stroma from both physical insult and radiation through absorption of toxic wavebands[272]. Fortunately the epithelium has evolved to regenerate damaged tissue in less than 24 hours. In doing so, basal epithelial cells are generated at the limbus, migrate upwards towards the outer epithelium and are shed in a continuous process. This regeneration of epithelial cells by the limbus emphasises

the importance of this tissue and the need for adequate protection from radiation insult[273] [274]. Posterior to the corneal epithelium lies Bowman's membrane. Consisting of layered collagen fibres, this membrane serves to maintain the structure of the cornea. If injured, it does not have the ability to regenerate and can cause some visual disturbances. Adjacent to this membrane and more posteriorly located is the corneal stroma. Also consisting of collagen fibres, the stroma is the thickest layer of cornea, comprising ~ 80 - 90 % of its thickness, ~ 78 % of which is water [275]. Corneal transparency is due to the spacing arrangement and good index-matching of the collagen fibres within the hydrated stroma and the fact that the collagen fibres are poor light scatterers due to the wavelength of visible light being much larger than their radius'[276]. Descemet's membrane is located posterior to the corneal stroma and serves to protect against infection and injuries. It is also comprised of collagen fibres and is self-regenerating. Most posterior is the very thin endothelium. This acts as a fluid pump maintaining osmotic pressures and protects water from entering the corneal stroma from the aqueous humor, thereby stopping stromal swelling and maintaining corneal clarity. Damage to the corneal endothelium is irreversible and thus it is a vital component in maintaining corneal clarity and refractive power[277].

1.3.2 The Conjunctiva

The conjunctiva is a vascularised transparent mucous membrane which covers the outer surface of the ocular globe and is continuous with the limbus of the cornea and the inner eyelids. At the palpebral region, the conjunctiva meets

the skin at the junction of the lid margin. The palpebral conjunctiva lines the internal eyelid, while the bulbar conjunctiva lines the globe and merges with the limbal tissue. It possesses a circulatory supply of many small blood vessels, and is the most immunologically active tissue of the external eye[278]. Although lacrimal glands produce the greatest volume of tears to bathe the external eye, secretory glands in the conjunctiva produce a tear film which help to lubricate and protect it[279].

Experimentally demonstrated by Cullen *et al.*, the conjunctiva has a similar action spectrum to that of the cornea, with a peak spectral response at approximately 270 nm in the UVC, just outside the terrestrial solar spectrum[280] [281]. The relevance of this lies in the fact that the conjunctiva is as susceptible to radiant exposure as the cornea.

1.3.3 The Limbus

This limbus forms a highly vascularised annulus of tissue approximately 1.5 mm wide around the cornea[282] [283]. Clinically and histologically, it is a distinct transitional zone where the corneal epithelium gradually develops into the sclera and conjunctival epithelium and it comprises tissue both from the limboscleral junction and the corneo-limbal junction[284] [285]. Its functional importance permits it to be considered as its own entity whose functions include: peripheral corneal nourishment, assistance in corneal epithelial regeneration and provision of an outflow for the aqueous humour. The main sources of corneal epithelial

regeneration are stem cells located in the basal epithelium at the corneo-scleral limbus[286] [287] [288] [289] [290]. Any photochemical alteration of stem cells due to phototoxic wavebands absorbed can result in loss of functionality and degeneration of adjacent healthy corneal and conjunctival tissue[291].

It has been proposed that limbal stem cell alteration as a result of chronic UVR exposure is related to the pathogenesis of pterygium. Although the corneoscleral limbus is afforded protection from UVR damage due to the presence of melanin pigmentation[292], PLF is implicated as a causative factor the aetiology of pterygium. This is best explained by the fact that the limbal basal epithelial cells are susceptible to UVR damage as they are not guarded against posteriorly concentrated refracted rays by the superficial layers of the corneal epithelium[293]. Ordinarily the epithelium would offer protection for UVR incident 'normal' to the corneal surface, but in the case of angularly dependent PLF, any UVR transmitted by the temporal cornea, focuses to a maximum concentration at the nasal limbus. This gives further insight into why pterygia are regularly found along the horizontal meridian at the nasal aspect of the cornea[294].

1.3.4 The Sclera

The sclera, or white of the eye, functions to protect the intraocular components and along with the cornea, forms a complete and almost spherical envelope of the ocular components, maintaining its shape with intraocular pressure. Composed primarily of the same collagen fibres as the cornea, the sclera

appears opaque due to the disorderly nature of these fibres. The transparent cornea is a result of these fibres being arranged in a lattice and the fact that the cornea is dehydrated.

1.3.5 The Lens

Located between the aqueous filled anterior and posterior chambers, the biconvex lens is the second and final refracting structure, providing approximately 30 % or ~ 15 dioptres of the eye's total refractive power[295]. As an adaptive refracting body, the lens changes its focal length, and thus its refractive power, by control of the nervous system, to form a clear image on the retina and it is this process of accommodation which signifies the importance of this refracting body.

It has an average refractive index of approximately 1.420, but this value can progressively increase with age[296]. Similar to the cornea, it is a very inefficient scattering tissue, and changes in its structure can cause an increase in scattering, resulting in a gradual opaqueness and cataract[297 298]. In cross section there are three main regions of the lens in which cataracts mainly occur – the cortex, nucleus and posterior pole[299 300].

While accommodation is the lens' primary function, it also efficiently absorbs approximately all UVR between 300 nm and 400 nm which is transmitted through the cornea[301 302 303]. It is the prolonged and repeated absorption of these wavelengths which is considered a risk factor in cortical cataracts[304 305 306]. As

the lens ages, it transmits lower amounts of short-wavelength visible and UVA and UVB as a result of its transmission curve being red shifted[307 308 309]. Thus the adult lens and cornea provide better filtering for these more actinic wavelengths thereby protecting the retina from UVR and the resulting pathological changes such as Age-Related Macular Degeneration (AMD) and possibly posterior uveal melanoma, both of which are epidemiologically linked to UVR absorption[310 311 312 313]. Furthermore, retinal absorption of UVR wavelengths increases with the removal of the lens during cataract treatment, and so replacement intraocular lenses (IOL's) with spectral filters mimicking the healthy natural lens are mostly fabricated from biologically compatible materials which absorb short wavelength visible radiation and UVR, without impeding visual performance[314 315 316 317].

1.4 UVR at the Anterior Segment

The intricacies of quantifying the ocular radiation field have been described with respect to the environmental and physiological factors in section 1.2.4. The phenomenon of PLF, along with direct and diffuse UVR incidence, will now be discussed with emphasis on each ocular tissue's receipt of and response to solar UVR. A literature review of experimental research to date on PLF is also given.

1.4.1 Axes of the Eye

The head and ocular structures are commonly divided into a number of orthogonal reference planes for descriptive purposes. Of particular interest here

are the coronal and sagittal planes. The coronal plane bisects the eye vertically, from front to back, or anterior to posterior, while the sagittal plane effectively bisects the eye vertically, or superiorly to inferiorly, along the primary line of sight, as can be seen in figure 1.9. The angle of PLF investigated by others and used in investigations detailed in subsequent chapters will be referred to as an angle relative to the coronal plane, i.e. 0° being at the coronal plane.

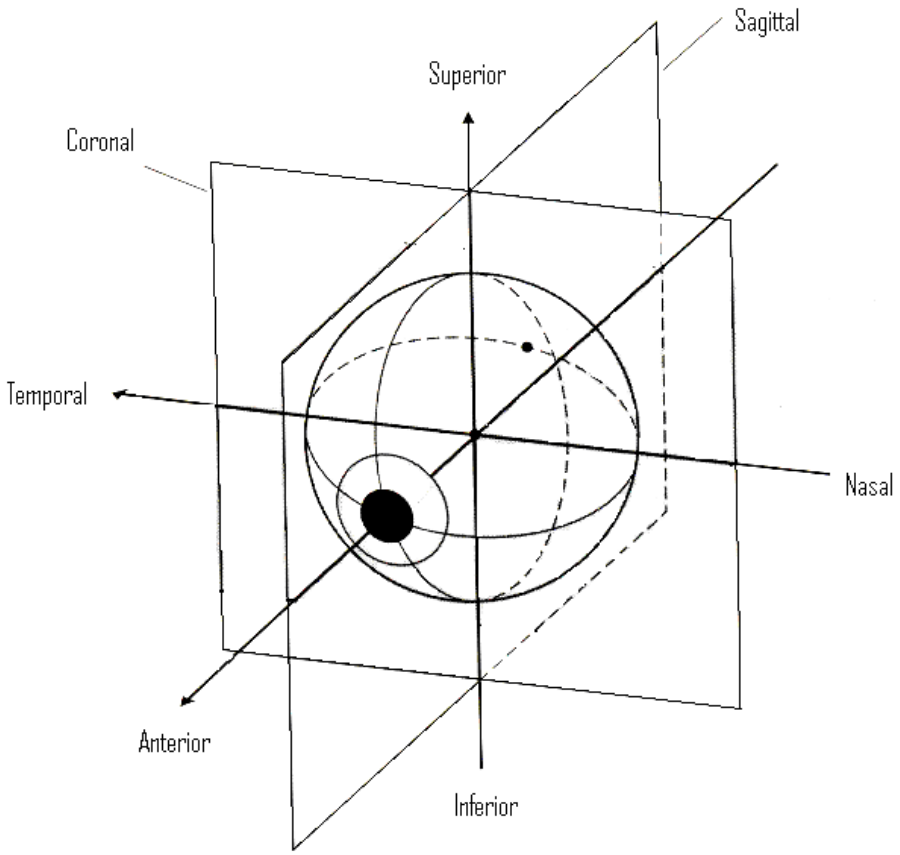

Figure 1.9:

Reference Axes for Eye and subsequent PLF descriptions (adapted from Oyster[318])

1.4.2 Incident light field

In an insolation environment, the human eye is subject to receiving solar radiation from a large range of angles depending on SZA and head orientation due to both the direct and scattered diffuse components, rendering it very difficult to determine the flux of UVR incident both temporally and spatially. As environmental conditions are changing, normally a person's position and spatial orientation with respect to the environment also changes. Monitoring the UVR irradiance at the ocular surface requires a robust and portable sensing device which can provide real-time data reflecting a person's spatial orientation to the solar radiation field and surrounding environment, encompassing environmental influences and surface reflections[319]. A sensor array was designed, constructed and tested for such field-based studies, and is detailed in section 3.3. However a refractive process can occur in certain light fields whereby direct solar rays from large SZAs, or reflections from vertical structures in a subjects surroundings, strike the temporal portion of the cornea and come to focus at the nasal aspect. This will now be discussed in section 1.4.3.

1.4.3 Peripheral Light Focusing (PLF)

In the first of a series of papers by Coroneo in 1990, the phenomenon of Peripheral Light Focusing (PLF) was hypothesised[320]. The notion of laterally focused UVR across the cornea served to reinforce the hypothesis that UVR plays a key role in the development of ocular disorders such as pterygium and other

intraocular disorders. Using a handheld penlight, his observations were captured qualitatively using photographic methods. It was noted that there are three main types of UVR concentrations refracted across the cornea and aqueous solution which coincided with sites of ocular disorders thought to be a result of solar UVR absorption, depending on incident angle, θ:

Type I: Focusing of light originating at oblique angles towards the medial limbus.

Type II: Moving more anteriorly, rays progress through the anterior chamber and are absorbed by the crystalline lens.

Type III: Moving more posterolaterally, rays leave the cornea above the limbus at the nasal aspect and strike the lid margin.

Figure 1.10 provides a depiction of the PLF effect. As the completely transparent cornea is the principle component of refraction within the eye, it emerges anteriorly from the sclera with a radius of curvature of, on average, 7.8 mm anteriorly and 6.5 mm posteriorly. Illustrating the cornea alone, figure 1.10 highlights that rays striking the corneal dome at an incident angle, θ, posterior to the coronal plane, are coupled into the cornea and aqueous solution and refracted across the anterior chamber to focus at the limbus.

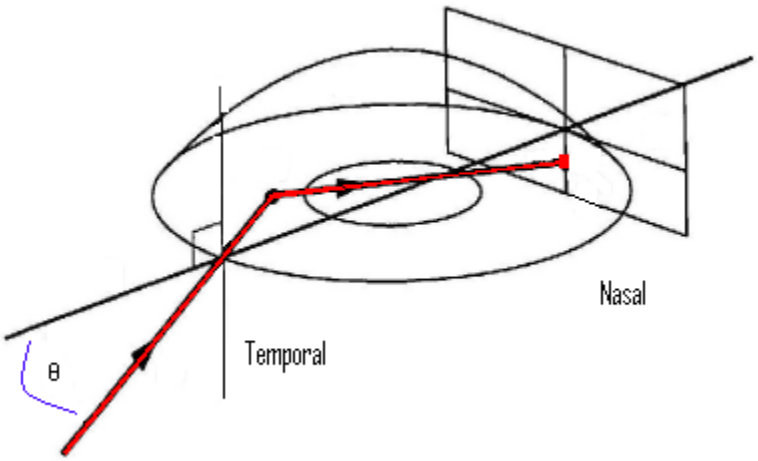

Figure 1.10:

Schematic of Peripheral Light Focusing (adapted from Maloof et al)

As shown in figure 1.10, rays generally strike the corneal dome at the more exposed temporal aspect and come to focus at the nasal aspect. Coroneo also noted that with greater corneal curvatures, the greater the likelihood of PLF occurring. As Coroneo noted, pterygium may occur at the temporal limbus also, by symmetrical PLF (UVR incident nasally may be focused temporally), but this is far less common as the prominent nose blocks these rays[321]. The implications of these findings served to initiate a host of research into these initial observations as detailed in the next section.

1.4.4 Literature Review of Peripheral Light Focusing

After the initial observations using the handheld penlight, which were photographically documented, and having described the PLF effect and hypothesising that certain ocular manifestations could be a direct result of a focal

concentration of UVR at the nasal limbus, such as pterygium, Coroneo *et al* made further investigations to quantitatively analyse the peripheral refraction phenomenon by inputting standard values for a human eye model using computer-assisted ray-tracing[322]. Through this model, it was computed that for these parameters, an incident angle of approximately 18° posterior to the coronal plane resulted in an increase of light intensity up to 20 times at the limbus. To measure the computed concentration of light at the limbus empirically, a bovine eye model was irradiated by a tungsten halogen lamp, to provide visible light, and the effects of varying incident angle were studied. Light located peripherally (angle not given) at the temporal limbus resulted in a focal concentration at the temporal limbus. By moving the source more anteriorly, it was shown that the light was refracted more posteriorly striking the inner surface of the ocular globe. In doing so, it was incident upon the crystalline lens. Similar focusing effects were demonstrated for a laser line at 308 nm.

Maloof *et al* also performed ray-tracing analysis on model corneas of various radii and various shape factors, varying the incident angle between 5° and 18° posterior to the coronal plane[323] [324]. They concluded that for all corneal models and angles modelled, the focused light was at minimum at least one order of magnitude of order greater than the incident intensity.

Narayanan *et al* designed a model eye, situated within a human skull, consisting of plano-convex lens (n = 1.473), which transmitted radiation from 340 nm upwards[325] [326]. Attached to this was a base disc of photosensitive paper. The

gap between the two components was filled with a solution of refractive index 1.333. Since there was no model iris, the entire base disc was exposed to radiation and later analysed densitometrically. They concluded that the peripheral temporal cornea concentrated incident light to the nasal aspect, due to the lid, bony orbit and nose preventing PLF from occurring from the nasal to temporal direction. A draw back was the difference in refractive index of their model cornea with that of the human cornea, 1.376.

Cullen *et al* modified a slit lamp biomicroscope to produce a collimated beam of visible light. This was passed from the temporal to nasal limbus of twenty test subjects. Minimum and maximum angles of incidence producing a focal glow at the nasal limbus was recorded. They concluded that all temporal incidence angles between 0° and 25° posterior to the coronal plane can maintain a peripherally focused spot at the nasal aspect. It was further deduced that deeper anterior chambers result in wider temporal catchment angles, thus increasing the risk of PLF, type I, II and III[327].

Findings by Kwok *et al* more recently included maximal peak intensities of UVA and UVB sensors placed at the nasal limbus of an anatomically based eye model of 28 ± 3° and 32 ± 3° from fixation respectively. These were achieved using a 350 W mercury arc source which produced a collimated beam within the 200 to 2500 nm range. The incident angle was varied between 0° and 40° posterior to the coronal plane[328].

A series of papers by Blue *et al* and Miller *et al* describe in detail the evolution of a fibre-optic sensor to take real-time measurements of drug concentrations in the anterior chamber [329] [330] [331] [332] [333] [334]. The fibre optic sensing device they fabricated was termed a scleral lens which consisted of an input and output fibre optic machined to attach to the synthetic fused silica scleral contact lens. This permitted acquisition of absorbance data of various chemicals in the human and rabbit eye *in vivo*. No investigations into the PLF phenomenon were mentioned and no actual transmittance data of the cornea *in vivo* was given without administered chemicals present in the aqueous solution.

Most recently, Twelker *et al* empirically measured the angular catchment range within which PLF occurred. A head mount apparatus consisting of a fibre optic guide which passed light from a halogen lamp was assembled and directed towards the temporal limbus of 30 human test subjects. By observation, the nasal limbal focus' peak intensity was noted at the angle it occurred for every individual. The incident angle was varied between 15° anterior and 50° posterior to the coronal plane and it was found that the range of nasal focus for the group of 30 subjects was between 14° and 31° posteriorly, with an estimated peak intensity of 27° posterior to the coronal plane[335].

For the research presented in this thesis, a photodiode array was designed, constructed, and tested to measure the direct and diffuse terrestrial solar UVR fields at the anterior ocular surface and to distinguish between the levels of each reaching the eye for a range of head angles and carriages in the field. In doing so,

the distribution of terrestrial solar UVR across the ocular surface for such varying conditions was measured. Incorporated with these measurements are investigations of modelled PLF for various incident angles and empirical measurements of PLF *in vivo* and the resultant corneal transmission spectra as measured with the novel lab-based PLF setup.

1.5 Ocular Effects of Solar UVR – The Ophthalmohelioses

1.5.1 Introduction

Ocular disorders associated with UVR insolation have been termed the 'ophthalmohelioses'. Other postulates suggest different environmental and biological conditions trigger the formation and progression of pterygia, photokeratoconjunctivitis, pinguecula and cataracts[336]. Environmental factors include heat, dust, humidity and UVR, while biological factors include genetics, pre-existing pathologies and infection[337]. Within the 'pterygium belt', which spans from the equator to approximately 30° – 40° north and south, a high proportion of globally reported pterygia have been found, further supporting the theory of UVR being implicated in its aetiology, although epidemiologic research based in Singapore, at 1º north of the Equator, by Wong *et al.* has concluded that the 'pterygium belt' hypothesis is oversimplistic and that other independent environmental factors could also be involved in its pathogenesis[338 339 340 341]. In 2007, conclusive evidence linking sun exposure to pterygium formation remains

somewhat elusive, although many clinical and epidemiological studies have concluded a definite association between UVR and pterygium formation[342 343].

Each ocular tissue selectively transmits radiation and in doing so filters radiation reaching subsequent tissues[344]. As a result of this selective absorption, the lens receives a far lesser percentage of the incident terrestrial solar UVB than the exposed cornea[345]. However, the cornea transmits a substantial percentage of UVA. Of the radiant energy incident at the corneal surface, approximately 0 % beneath 280 nm is transmitted and its subsequent transmittance is ~ 8 % at 300 nm, ~ 55 % at 320 nm, ~ 63 % at 340 nm and ~ 66 % at 360 nm. As can be seen, the crystalline lens absorbs almost all radiation between ~ 300 nm and ~ 360 nm in the UVA waveband. It has been noted that damage to the lens through UVA absorption would require prolonged and chronic exposure, far exceeding that normally encountered outdoors[346]. The selective absorption of the different ocular tissues can be seen in figure 1.11.

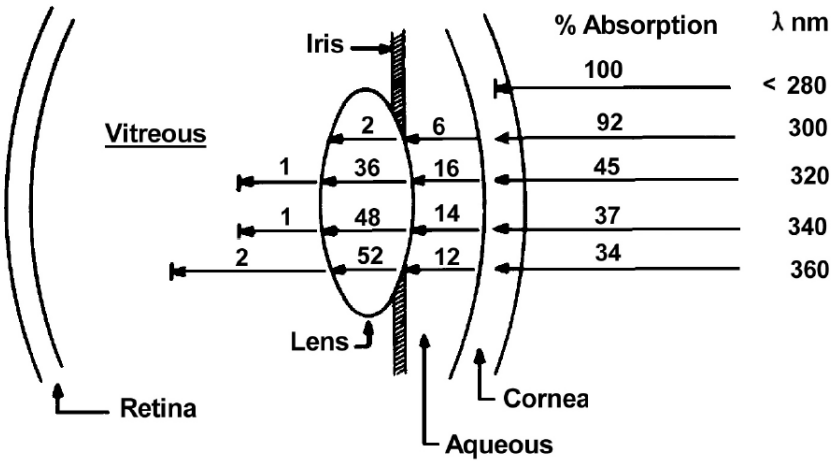

Figure 1.11:

Selective Absorption of ocular media (after Sliney[347])

As can be seen in figure 1.11, the anterior cornea is the most vulnerable tissue with respect to terrestrial solar UVR. The more posterior tissues, chiefly the lens and retina, are afforded protection from the actinic UVB wavelengths. In order to protect the exposed corneal tissue, and adjacent annular limbus, the best possible protection is that afforded by UV-blocking contact lenses which cover the entire corneal diameter and extend slightly to the conjunctiva, thereby protecting the delicate limbal cells also. In turn, less UVR reach the intraocular tissues also[348].

In order to ascertain the different photobiological effects occurring at the different ocular tissues due to the selective intraocular transmittance of the various media without protection, it is necessary to elicit an action spectrum for each tissue.

1.5.2 Acute and cumulative effects of ocular UVR Exposure

1.5.2.1 Photokeratoconjunctivitis

As indicated in figure 1.11, the cornea does not transmit radiation beneath 280 nm and absorbs approximately 92 % at 300 nm. The corneal epithelium and Bowman's membrane are responsible for this major increase in absorption between these wavelengths in the UVB band, and the clinical result is photokeratoconjunctivitis, or snow-blindness. Kolozsvári *et al* measured the UVR absorbance of freshly excised cadaver corneas from 240 to 400 nm and found that the epithelium and Bowman's membrane have significantly higher absorption coefficients than that of the stroma. It was found that although the stroma has a lower absorption coefficient, but due to its thickness it is a very significant UVR absorbing layer also. As an acute response to UVR, there is generally an average latency period of approximately 6 to 12 hours before symptoms present. These generally include erythema of the skin surrounding the eyes, irritation and discomfort of the ocular surface, photophobia and visual impairment. Generally symptoms subside 36 - 48 hours post-trauma. The scale of impairment depends on duration exposure and also the spectral nature of the UVR source. Fortunately only in rare circumstances permanent ocular injury results [349] [350] [351] [352] [353]. Arc welding can also induce this acute injury and cause insult to exposed skin if a UVR absorbing face-mask and accompanying protective measures are not utilised and is more commonly known here as 'arc eye' or 'welders flash'[354] [355]. Indeed, cases of photokeratitis, among other UVR related skin conditions, have been reported in the workplace due to faulty lighting which emitted UVR[356] [357].

1.5.2.2 Pterygium

Described as an 'ophthalmic enigma'[358], pterygium is a proliferative, invasive and fibrovascular 'conjunctivalisation' of the cornea, in which the conjunctiva encroaches onto the cornea, usually at the three and nine o' clock positions at the limbus[359 360 361]. It has long been recognised as occurring more at the nasal portion than the temporal and can cause a loss of transparency, dry eye and may eventually lead to visual disturbances and refractive errors such as astigmatism due to localised flattening of the cornea's apex if left untreated[362 363 364 365 366 367 368 369 370 371]. It is characterised by the encroachment of a wing of altered vascular tissue over the cornea and is considered to originate at the limbus and progress to the central cornea, through transformation of limbal stem cells[372 373 374 375]. The aetiology of pterygium has yet to be satisfactorily explained, but many population based studies and histologic studies have concluded that incidence of UVB is an actinic factor[376 377 378 379 380] . Furthermore it is also believed that pterygium is most probably a result of cumulative UVR absorption by the anterior ocular tissues and that outdoor activity in a person's formative years can bear a significant impact on pterygium formation later in life, similar to skin cancer[381 382]. Among others, alarming rates in one study showed pterygia had recurred in ~97 % of patients one year after surgical excision, re-emphasising the seriousness of this disorder[383 384 385 386].

1.5.2.3 Cataract

Considered to be age-related and characterised by a partial or complete and stationary or progressive opacity of the lens due to increasing scatter, cataracts are the result of a denaturing of lens protein structures and are a leading cause of blindness globally[387]. Risk factors associated in cataractogenesis include UVR absorption, in particular UVA wavelengths, since nearly all incident UVB is absorbed by the cornea, secondary effects of diabetes, smoking, diet and steroid use. Of all three types of age-related cataract; cortical, nuclear and posterior subcapsular (PSC), each type causes an opacity to a different region of the lens and invariably have distinct risk factors[388 389 390]. Of most interest to the research detailed here, lower nasal cortical cataracts are believed to be a result of UVR absorption for a number of reasons, namely the degree of lid opening, which is variable among different ethnic populations, and the subsequent role type II PLF may play in focusing temporal rays towards the cortex[391 392]. Radiation incident at shallow angles of incidence from the coronal plane striking the temporal cornea can be refracted through the pupil towards the nasal quadrant of the crystalline lens and it is thought that this amplification and focusing of UVR at this region may induce lenticular opacities[393]. As suggested by the Chesapeake Bay Watermen Study, there is a clear association between UVB and potential for development of cortical cataracts more so than other types. This further emphasises the need for ocular protection via UVR-absorbing contact lenses, sunglasses and the incorporation of wide-brimmed hats[394 395].

1.5.2.4 Pingueculum

Usually asymptomatic, pingueculae do not affect vision. They are characterised by an elevated yellowish growth at the limbus at either the three or nine o' clock positions. UVR is implicated in the pathology of pinguecula, but exposure to the elements may be a contributory factor in their manifestation also. They show the same predilection for nasal presentation as pterygia, possibly due to reflected UVR from the nose to the nasal aspect, but a definite link between UVR and pinguecula occurrence nasally has yet to be established[396 397].

1.5.3 Protecting the Eye in an insolation environment

1.5.3.1 Squint mechanism and natural aversion

In visibly bright conditions the natural response of the human eye is to gaze at a region in the foreground which causes relatively less sensory discomfort than the brightest visible regions. This instinctive aversion response is one of the body's mechanisms to protect the retina from intense light. Fortunately this mechanism not only protects the retina, but as a direct consequence safeguards other ocular tissues at risk from intense radiation fields such as the cornea and lens. Although there is a high degree of protection afforded by looking away from an intense source, the inability of the human eye to perceive UVR poses another threat. If the immediate foreground has a high UVR albedo, such as that of snow (~ 80%), the eye still receives reflected UVR when gazing away from the sun. Squinting can reduce received reflected rays, but proper ocular protection by means of UVR absorbing contact lenses is the most beneficial protection for everyday practical protection, with possibly the wearing of a wide-brimmed hat or other shading headwear[398]. The insidious nature of non-UVR absorbing sunglasses or UVR absorbing sunglasses with shapes that are not completely wrap-around is apparent. It has been suggested that by wearing darkly tinted sunglasses without 100 % UVR protection, one's voluntary and involuntary aversion responses are suppressed, thereby leading to a net increase in dose of solar UVR at the anterior ocular tissues[399]. The use of typical darkly tinted sunglasses with UVR absorbing properties reduces UVR exposure dose for rays

near normal to the sunglass surface, but rays can enter the ocular region temporally, or be reflected towards the eye from the back surface of the spectacle lens which does not have an anti-reflective coating, in effect limiting the functionality of such sunglasses[400]. The natural squint mechanism is suppressed under such conditions which effectively increases the field of view for diffuse and temporally incident radiation to strike the cornea and be refracted to its nasal aspect[401]. If a subject has a preference for sunglass protection over contact lens protection, the most beneficial types are those which block temporally oblique rays and absorb all UVR, such as Oakley's trademark wrap-around series of sunglasses, XYZ Optics®, incorporating Plutonite® which they claim absorbs 100 % of all UVR wavebands effectively to 400 nm[402].

1.5.3.2 UVR absorbing contact lenses and sunglasses

By covering the entire cornea, and in many cases encroaching onto the limbus and conjunctiva, a UVR absorbing contact lens provides the most beneficial protection for everyday activities without being cumbersome, as is often the case with fully wraparound sunglass protection. Most commercially available UVR absorbing sunglasses offer protection only to the rays along a person's fixation. The need for adequate lateral protection of directly, reflected and diffusely incident radiation was confounded by the discovery of the PLF effect The most beneficial protective device for such incident radiation would be a 100 % UVR absorbing contact lens in conjunction with the protection provided by fully wrap-around, UVR absorbing glasses or ski-goggles[403 404 405 406 407].

The UVR absorption properties of various contact lenses has improved extensively over the last number of years with Johnson and Johnson Vision Care (Jacksonville, FL) now providing a range of silicon hydrogel lenses which afford excellent ocular protection from these phototoxic wavelengths in the UVR waveband in the form of their daily disposable contact lenses. The functionality of such disposable lenses is no different from lenses of old; the distinguishing factor is their UVR blocking capabilities. The transmission curve of a contact lens is controlled by features such as the type of hydrogel and UVR blocker used, the water content and lens thickness across its surface.

During the research described in this thesis, the UVR transmission of a range of blocking and non-blocking contact lenses was investigated but is not directly part of the PhD research project described here[408]. However, many of the methods described by the author were applied to the contact lens research and forms part of the overall ocular research carried out in Dr. Walsh's group in conjunction with his colleague, Prof. Jan Bergmanson.

1.6 Conclusion

The insidious nature of ultraviolet radiation for both human skin and ocular tissues has been described in this chapter. The various environmental and physiological factors that influence the receipt of UVR at the ocular surface have been outlined and emphasised and the inherently difficult nature of ocular UVR

dosimetry. Also outlined were the various protective devices available currently and the merits of each. To further understand the complex nature of terrestrial solar UVR at the anterior ocular surface, novel UVR sensors are required to make real time measurements of all aspects of the radiation field at the human eye under a range of environmental conditions. As no optical sensing device currently available is capable of measuring all the distinct interacting mechanisms of UVR with the ocular surface, two different optical sensing systems have been designed, constructed and tested in this thesis, to gain further understanding of the distribution of UVR across the horizontal margin and the possible increase in UVR irradiance at the nasal aspect due to the PLF effect. By incorporating the array in field-based measurements, the repeatability, ease of use, and variations of UVR across the palpebral fissure due to different head shapes will be demonstrated together with the increased dose received at the nasal aspect due to PLF that is attenuated by the corneal transmission. Data from these two systems can then be combined to gain a better overall perspective on the human ocular UVR field and go a long way towards the implementation of the ideal ocular UVR sensor.

Chapter 2 reviews the theory of the optical instruments and components used in the design and methodology of the resulting ocular array, described in chapter 3, with its field based results in chapter 4. The design, methodology and results of PLF investigations and the related corneal transmission spectra are described in chapter 5.

Chapter 2

Radiation Detection Methods

2.1 Introduction - Radiation Detection at the Eye

Measurement of the terrestrial solar UVR field at the anterior ocular surface would ideally be performed with one detecting device. But due to the infinitely complex nature of such an environmental measurement, it is necessary to incorporate a number of different sensing devices and techniques, and subsequently present the data. By doing so, as many variables as possible can be accounted for, thereby gaining a better understanding of the incident radiation and its spatial distribution and variation for a given spatial orientation with respect to the direct solar beam. Coupled with the direct solar beam may be the diffuse, diffuse-scattered, diffuse-reflected, and resultant PLF effects due to a combination of the (aforementioned) environmental conditions discussed in Chapter 1. No single instrument is capable of accurately quantifying all of these[409].

For this reason a number of distinct sensing devices and techniques have been employed by many groups for field, in-vitro and in-vivo measurements. Included in these are the commonly used passive polysulphone dosimeters (i.e. capable of operating without an external power source), broadband radiometer and spectrometer methods, and photodiode sensors, the latter three of which were employed for the research presented in this thesis. A description of these is presented in sections 2.3 to 2.5. A description of one of the most commonly used

devices in the field for solar UVR dosimetry at different body parts is given in section 2.2, the polysulphone dosimeter.

In addition to the following optical theories of components used in the sensing systems in this thesis, the optics of the human eye and facial structure and how they have an effect on sensor design need to be considered. Some of these can be outlined as follows:

- Does the sensor see what the human tissues see in terms of field of view and spectral response?
- Can data be recorded rapidly to reflect the real time changes in solar irradiance and head carriage?
- Can the sensor record radiation incident on the ocular tissues and that refracted across it due to PLF?

While all aspects of the optical engineering of human ocular radiation field detection systems have not been resolved, the complexity of designing and implementing such systems is highlighted and subsequent results show that the research presented has progressed the science considerably.

2.2 Polysulphone Dosimetry

Polysulphone dosimeters have been employed by a number of groups at a variety of points on the body and in various contact lens and headform designs.

These have been exposed to terrestrial sunlight at different locales, head positions and orientations to investigate the whole body and ocular exposure in such conditions and the effectiveness of ocular shading provided by hats and sunglasses[410 411 412 413 414 415 416 417 418 419].

First recognised and developed by Davis *et al*[420] as a possible dosimeter for UVR and now used extensively as a means of quantifying the UVR dose at various points at the body, polymeric polysulphone dosimeters have also been used to measure the exposure dose received at the ocular tissues[421 422]. The requirement of a dosimeter such as this is that its spectral response corresponds closely to the action spectrum of a photobiological effect of the biological tissue under investigation over a pre-defined waveband. Polysulphone is predominantly employed to quantify UVR incidence at the skin as its spectral response is comparable to the human erythemal response curve[423 424 425 426]. The basis of such dosimeters is that absorbed radiation induces changes in their optical properties, and the changes in absorbance are generally measured at 330 nm by a spectrophotometer which compares an exposed and unexposed polysulphone film[427 428]. Since polysulphone responds only to wavelengths shorter than ~ 330 nm, this wavelength elicits the maximum UV-induced change in absorbance of polysulphone and increased absorbance is proportional to UVR exposure dose[429]. Due to the polysulphone manufacture process, resultant non-uniform thickness profiles and surface blemishes on the film are inherent and can lead to erroneous exposure dose-response relationships at skin locations being investigated. Although the incorporation of polysulphone as a solar ultraviolet

dosimeter is advantageous for many research applications, there are several drawbacks for ocular UVR dosimetry including repeatability, reliability of manufacture process, dosimeter calibration, response time, possibility of dark repair, and the fact that it can be used only once, providing only a cumulative erythemally weighted UVR dose[430 431 432]. It was considered that an alternative sensing device may be equally accurate, more adaptable, more robust and capable of acquisition in real-time. By continuously logging and recording data, extrapolations and quick analyses could be performed during measurement with better efficiency.

2.3 Photodiode Sensors

The principal aim behind the detection of radiation is largely similar for many different electronic photodetectors, including photomultiplier tubes, pyroelectric detectors, light dependent resistors and photodiodes. Absorbed radiant energy is converted into an electronic signal, which ideally is proportional to the intensity of the incident radiation.

Photodiodes are sensing devices that are fabricated from semiconductor materials and absorb radiation over a specific spectral band, depending on the semiconductor bandgap. The main advantages of the photodiodes used in the design and construction of the sensor array for the field-based work here was that their physically small dimensions permitted five to be placed across the exposed ocular tissue, thereby covering key points on the surface, they had a relatively

large field-of-view, similar to that of the exposed ocular tissues[433], and they had efficient photon-electron conversion. They were also solar blind, meaning that they were responsive only to photons in the UV region of the electromagnetic spectrum through utilisation of a filter which eliminated photons above 400 nm from reaching the detection region.

In order to discuss the operation of semiconductors, it is essential to briefly outline the band theory of solids. The distinguishing factor between a metal, semiconductor and insulator can be described best in terms of the energy bands within which electrons can exist. Each of these bands has a number of discrete energy levels. The valence electrons within conductors can be readily freed. Conversely, electrons are bound intensely to their constituent atoms within an insulating material and it can typically take more than 3 eV to liberate an electron and make it available for conduction. Here, there is a forbidden region between the valence and conduction bands known as the *bandgap* within which no electrons exist. This is the energy difference between the most energetic valence band and the least energetic conduction band. Providing energy to a solid by means of an electric field will cause electrons to be accelerated by the field, thereby gaining energy. This will occur only if the electrons can move from their current energy level to that of an unoccupied higher level. A material is insulating if the valence band is completely filled, with a large forbidden band between it and a higher energy band, the conduction band. At absolute zero (T = 0 K), the energy diagram for semiconductors illustrates that all energy levels in the valence band are occupied by electrons and the conduction band possesses no electrons. In

this case the material is considered insulating. The bandgap of most semiconductors is relatively small, generally of the order of 1 eV[434]. As the temperature is increased gradually above 0 K, electrons in the valence band gain sufficient energy through crystal lattice vibrations to break covalent bonds. Once free, these can contribute to increasing the electrical conductivity of the semiconductor and the process of free electron formation is known as *electron-hole generation*. In turn, these freed electrons leave behind positive charge carriers or *holes*, the sites where there were once electrons. The further the temperature is increased, the more energetic the lattice vibrations, the greater the number of electron-hole pairs are made available for conduction. The electrons promoted from the valence band to the conduction band can migrate around the empty sites known as holes, themselves leaving behind a hole at that exact moment, and the process is known as *electron-hole pair recombination*. The process increases the material's conductivity. An electron gaining enough energy to jump from the highest level in the valence band to a level within the conduction band gains kinetic energy to migrate further through an applied electric field.

By altering the structure of a semiconducting material, the conductivity of a semiconductor can be greatly changed. This is achieved by joining it with another semiconducting material with a similar crystal structure, forming one continuous crystal. The conductivity is dependant on the type of impurity and its concentration. This procedure is known as *doping*. Materials which have been *doped* (generally one part in a million) are known as impurity semiconductors.

This semiconductor photodiode device responds to photons absorbed by generating a photocurrent. In its simplest form, a photodiode is comprised of a p - n junction. An n-type semiconductor is a material which contributes mobile *electrons* and a p-type is one which introduces mobile positive *holes* when used as the dopant in another material. The diffusion of electrons from the n-type to the p-type material and holes from the p-type to the n-type develops a voltage across the junction causing a current to flow initially through an external circuit. This diffusion at the boundary results in a region known as the *depletion region* which has no free carriers. Electron-hole pairs generated at this region by absorption of light within the correct range of frequencies are swept away by drift in an external field across the depletion region and are collected by diffusion from the undepleted region. Radiation striking this semiconductor device of greater energy than the material's bandgap energy excites electrons into the conduction band, thereby creating a hole in the valence band. Within the depletion region, an electric field is thus set up by diffusion of the charge carriers. When connected to a loaded external circuit, the EMF exists across that load and an electric current flows through it proportional to the energy of the incident radiation.

2.4 Broadband Radiometry and Spectrophotometry

In order to gain quantifiable radiometric data in conjunction with UVR levels at the ocular surface as measured by the novel sensor array in the field, a UVR sensitive broadband radiometer was used to measure the downwelling global irradiance at the same time and location. Using a pre-determined

calibration factor, voltages measured from the photodiodes could be converted to irradiance data and subsequently permitted dosimetric extrapolations to be made across the anterior surface.

In vivo corneal transmission measurements taken with a novel fibre optic system were achieved through use of a spectrophotometer, which facilitated qualitative and quantitative data to be recorded. A description of the instrumentation used to accomplish field-based and in-vivo measurements is now given.

2.4.1 Broadband Radiometry

Radiometry describes the propagation and detection of radiation purely in terms of energy, power and geometry of propagation. The physical, radiometric description of electromagnetic radiation is expressed as radiant flux or power (W), irradiance (W m^{-2}), exitance or emittance (W m^{-2}). While radiometric measurements provide a quantitative irradiance value over the spectral response range of a detector, a spectroradiometer provides both qualitative (spectral) and quantitative (intensity) information about a source. The application of such data is crucial when considering the spectral response of a biological tissue across a measured spectral distribution. Radiometric quantities alone do not suffice as both qualitative and quantitative data are necessary when determining the hazard function of incident photon energy with respect to different biological tissues.

It is important to note also that the CIE has made a clear distinction between spectroradiometry and spectrophotometry. The former has now been defined as: 'Measurement of radiometric quantities in narrow wavelength intervals over a given spectral region'; the latter; 'Measurement of the ratio of two values of a radiometric quantity at the same wavelength'[435].

2.4.2 Spectrophotometry

Where a radiometer's sensing component is generally a single photodiode with a stated spectral response, incorporated with a cosine diffusing element, conventional bench-top UV-Vis spectroradiometer configurations consist of a broadband source, a scanning monochromator system with a dispersive element for wavelength selection, and a detection system. The principle dispersive element in most UV/Vis spectroradiometers nowadays is a diffraction grating[436]. A diffraction grating facilitates constructive interference of identical wavelengths to occur at specific angles depending on the wavelength of the radiation incident at its reflective surface. The dispersive power of a diffraction grating is determined by the density of grooves which have been etched onto it, generally expressed as the grating line spacing (grooves mm^{-1}). The linear dispersion of a diffraction grating describes the degree to which a spectral portion is spread across the focal field of the spectrometer and is expressed in nm mm^{-1}. Spectrophotometers with high linear dispersions will disperse a 0.1 nm spectral portion over 1 mm. The greater the spectral portion dispersed over 1 mm, the lesser the resolving power of the instrument.

The dispersion of a broadband source into its constituent wavelengths is based on the diffraction principle and as such, each wavelength is diffracted at a slightly different angle given by equation 2.1.

$$n\lambda = d\sin\theta \qquad \text{Eq.: 2.1}$$

where n is the order of diffraction, d is the grating line spacing and θ is the diffracted angle for a given wavelength, λ (nm).

The basis for the portable microspectrophotometer used in the work described in subsequent chapters is similar to conventional single monochromator UV-Vis spectrometers, except the sensing device is a charge-coupled device (CCD) array. A CCD uses a linear photodiode array and can rapidly capture multi-spectral information. The main difference between these and conventional spectrometers is the polychromatic dispersive behaviour of the former due to its Czerny-Turner design.

In this design, depicted in figure 2.1, light passing from a broadband source, A, passes through a slit (if present), B, and strikes a concave mirror, C, at its effective focus to promote collimation. A reflected beam is then delivered to a plano reflecting diffraction grating, D. Since the angle of the diffracted beam is wavelength dependent and thus each having a dissimilar diffraction angle, the now dispersed broadband beam strikes a second concave mirror, E, and is focused

on the CCD array, F. Radiations dispersed by the diffractive element and directed towards the CCD array are simultaneously detected by the CCD array. The reverse-biased photodiodes discharge a capacitor at a rate proportional to the photon flux. Once the charge has accumulated in the sensing array over the pre-set integration period, it is shifted to the transfer register where it is read out sequentially. As the data is read out, the next image is simultaneously building up on the detector array.

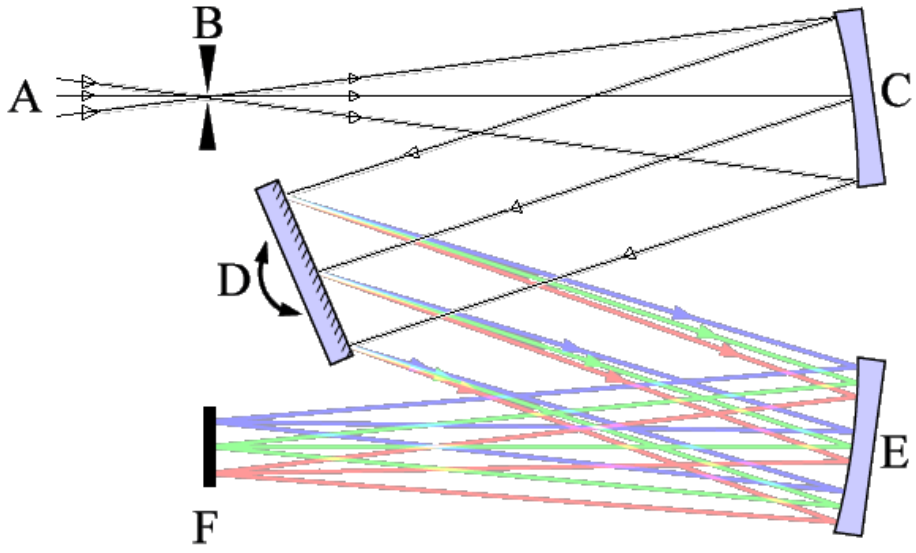

Figure 2.1:

Cross Czerny-Turner Monochromator

The advantages of such microspectrophotometer systems are the fact that they are very portable, adaptable and have no moving parts. Their main drawbacks are their stray light levels, and overlapping of diffracted orders when no blocking filter is present. Stray light can be produced by randomly scattered

light by surface imperfections on an optical surface within the monochromator or nonperiodic errors in the ruling of grating grooves and is generally eliminated by the incorporation of a double grating monochromator system. Double grating monochromator systems are generally the preferred choice above single systems described above. This is mainly due to their stray light rejection capacity. Due to their design though, radiation throughput is considerably reduced and this is an undesirable facet when measuring low light levels or more appropriately, when the detecting element has a low responsivity in a particular wavelength region.

It is important to note that any apparent wavelength feature in an extended spectrum may in fact be a second or third order effect occurring at one half and one third the wavelength of the fundamental. For example, a spectroscopic feature at 1200 nm, could also be present at 600 nm (2^{nd} order), 400 nm (3^{rd} order) or 300 nm (4^{th} order). These effects can be negated by the incorporation of a blocking filter in the optical path. It operates as a filter wheel which the spectrometer automatically sets as the correct filter for a given wavelength during a scan and limits the width of diffracted orders so they do not overlap.

To quantify the degree of light transmittance or absorbance by a material across a given waveband, a spectrophotometer is employed in tandem with a workstation which facilitates acquisition of measurements, analysis and storage of spectral data which can be analysed and interpreted more thoroughly after acquisition.

Using a broadband source, the acquisition of complete spectral information for a given sample can be accomplished by scanning across the spectral region of interest, in this study, the UV-Vis. As it is a non-invasive analytical technique, the sample under study undergoes no physical damage.

When radiation of initial intensity, I_i, passes through a homogenous medium of pathlength, x, there is a loss of initial intensity due to absorption in the medium due to the pathlength and the material's absorption coefficient, α. The transmitted intensity, I_t, is wavelength dependent. A material having a high transparency will have a small absorption coefficient so the transmitted intensity does not become appreciably less until the pathlength is very large. Visually opaque materials have large absorption coefficients for all wavelengths and so the transmitted intensity becomes very small even at the shortest pathlengths. This interaction of radiation with matter is described by the Beer-Lambert Law given in equation 2.2[437]:

$$I_t = I_i \exp^{-\alpha \cdot x} \qquad \text{Eq.: 2.2}$$

The absorbed radiation is usually converted to heat or could cause the material to fluoresce at less energetic wavelengths.

2.5 Fibre Optic Sensing

For *in vivo* PLF corneal transmittance measurements, the requirement was that the sensing device be as normal to the beam of emerging radiation at the nasal cornea. To achieve this, a fibre optic sensing technique was designed as it permitted the sensing element to be placed as close to the anterior ocular surface as possible with greater flexibility than using a photodiode, which was considered too bulky for this application.. Comprising a launch and collection fibre system, the launch fibre, along with collimating optics, allowed a defined circular beam to strike the temporal cornea at a known angle of incidence. The collecting fibre at the nasal side was linked to a spectrophotometer which permitted the acquisition of corneal transmittance data.

Generally consisting of a fused silica core and a cladding of plastic or glass with a lesser refractive index, a fibre optic transmits light by means of a phenomenon known as Total Internal Reflection (TIR). The index of refraction (n) may be defined as the ratio of the velocity of light in a vacuum to the velocity of light in a given medium, and similarly as a result of the difference of n between core and cladding, light may be guided along a waveguide such as a glass or quartz fibre[438].

Light passing from one medium, $n_{1,}$ to a second medium, $n_{2,}$ of a lower refractive index at a specific incident angle, $\theta_{1,}$ to the normal will be refracted, or bent, at a specific angle, θ_2 measured from the normal of a plane surface as illustrated in figure 2.2.

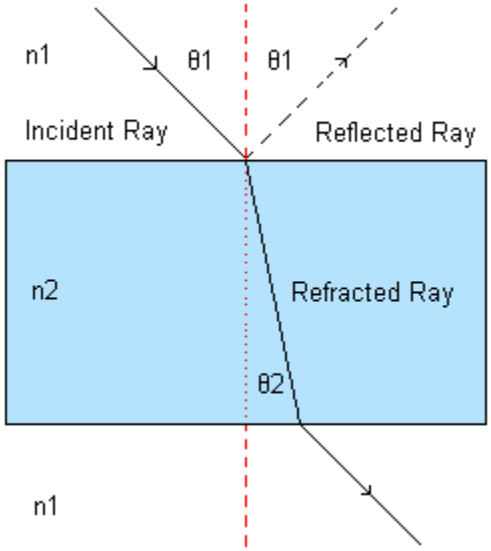

Figure 2.2:

Refraction at a plane surface.

This angular displacement of the light depends on the two refractive indices in question and is described by Snell's Law given in equation 2.3[439]:

$$n_1 Sin\theta_1 = n_2 Sin\theta_2 \qquad \text{Eq.:2.3}$$

As light propagating in the more dense medium (one of high refractive index), n_1, approaches a boundary with a less dense medium, n_2, at an angle θ_1, at or greater than θ_c, the critical angle, it is totally internally reflected. This implies that none of the light striking the less dense material at this angle escapes the boundary and remains propagating along the length of the optical fibre[440].

As mentioned above, the basis for TIR and light propagation along a fibre optic is the angular limitation of critical angle. This critical angle can be best described by equation 2.4[441]:

$$Sin\theta_c = \frac{n_2}{n_1} \qquad \text{Eq.:2.4}$$

The conditions for TIR to occur are as follows:

(i) $n_1 > n_2$

(ii) $\theta_1 > \theta_c$

When coupling light into a fibre optic, only rays incident at the input face within a certain range of angles will actually enter the fibre and propagate along its length. This limited acceptance cone is known as the (dimensionless) numerical aperture (NA) and it characterises a cone of rays which will be accepted or emitted from the fibre[442]. An extreme ray of light, propagating within a medium (for our purposes, air) with refractive index n_{air}, striking the input face of the fibre optic at the limiting angle, θ_{max}, to the normal will be refracted and propagate along the fibre. Since θ_{max} is the half-angle of the maximum cone of light that can enter or exit, all light entering within this defined cone will be accepted. The NA of a system as described by equation 2.5 cannot be greater than 1, where $n_{air} = 1$:

$$NA = n_{air} \sin\theta_{\max} \qquad \text{Eq.:2.5}$$

The NA of a fibre optic is fixed by the fibre characteristics and can alternatively be calculated by equation 2.6[443]:

$$NA = (n_{core}{}^2 - n_{cladding}{}^2)^{0.5} \qquad \text{Eq.:2.6}$$

The importance of this concept will become more apparent in Chapter 5, where a fibre optic probe was used to investigate PLF across a model anterior section. For efficient light collection, the fibre optic probe had to be placed within a confined range of angles to collect the refracted radiation.

.2.6 Conclusion

In summary, the incorporation of solar blind photodiodes in a novel ocular sensor array will be used to measure the irradiance distribution across the palpebral fissure in the field. The voltage output from the photodiodes will be calibrated against a broadband radiometer with a broadly similar spectral response under the same illumination conditions to relate output voltage to irradiance. Further to this, a novel fibre optic microspectrophotometer setup will be presented to investigate PLF across the cornea. Through this method the transmission of the human cornea *in vivo* will be demonstrated.

Having outlined the ideal sensing devices that can be used to achieve the specifications for ocular radiation sensing listed in the first section of this chapter,

the specifications of components and systems that most closely match these can be examined. It is these components and systems that were used to record the data presented and while they do not cover all of the ideal specifications, they show significant improvements on more widely used sensor devices such as polysulphone. Not to imply that the latter is without its merits, but advances in readily available optical technology provide us with the means to cover more of the desired specifications listed for real time, in-vivo quantification of the human ocular UVR field.

Chapter 3

Novel Photodiode Array Materials and Methods

3.1 Introduction

To reliably and repeatedly quantify the solar UVR field at the ocular surface, a portable sensing device with robust physical design was necessary to facilitate ease of use. The majority of investigations relating to the ocular UVR field previously have been achieved using polysulphone film and have been noted in section 2.2. Solid state technology has been used by other groups to ascertain the degree of protection afforded by sunglasses and palpebral fissure angle at the ocular surface in an insolation environment[444 445]. An early system to incorporate the use of numerous photodiodes was developed by Sakamoto *et al.* to measure the distribution of UVR on a mannequin head and around the ocular region. For this relatively preliminary study, it was found that the nasal brow ridge reduced the amount of UVR incident at the nasal aspect of the lid fissure and that irradiance was highest temporally, similar to the results presented in detail in chapter 4[446]. There were drawbacks relating to experimental design, primarily the fact that no human faces were used for quantification of the UVR levels at various facial sites, instead relying on a mannequin model, which would have had a different reflectivity in the UVR waveband to that of human skin. Walsh *et al.* integrated Texas Instruments TSL-250 photodiodes which had a spectral range from 300 nm to the infrared, and measured the ocular UVR bias for a number of

human models within an artificial light box[447]. From these initial investigations, the idea for a more meticulous ocular UVR field survey stemmed.

An ideal sensor for applications similar to those described for the research presented here will have specifications such as:

- Flat spectral response over the waveband being investigated.
- Solar Blind
- High quantum efficiency
- Large field-of-view
- Large dynamic range
- Linear output
- Fast response time
- Ease of use

As is the case with many sensing systems, a compromise must generally be agreed by considering the key sensor specifications which are essential to the given application. As the ideal sensor does not exist for the outdoor field measurements and PLF investigations described here, the sensor chosen fulfilled as many of the requirements and met as closely as possible the specifications outlined above. This photodiode sensor array developed in DIT will be described in section 3.3 and a brief account of previous sensor systems is given now.

3.2 First generation ocular sensor array

Preliminary research into the ocular light field was conducted by Dr James Walsh at the School of Physics, Dublin Institute of Technology. Initially, active photodiodes (i.e. needed an external power source) were soldered to an elliptically shaped piece of flat circuit board with similar diameter to the human eye. Wiring difficulties, bulk, sensor flatness, and distance from the eyelid made it impractical, but demonstrated the principle of ocular UVR measurements upon which the sensor used for the research presented in this thesis was based. Subsequently, a first-generation novel UVR sensing array was designed by a final year BSc undergraduate, Helen McEvoy, along with Dr Walsh in 1999, and can be seen in figure 3.1[448].

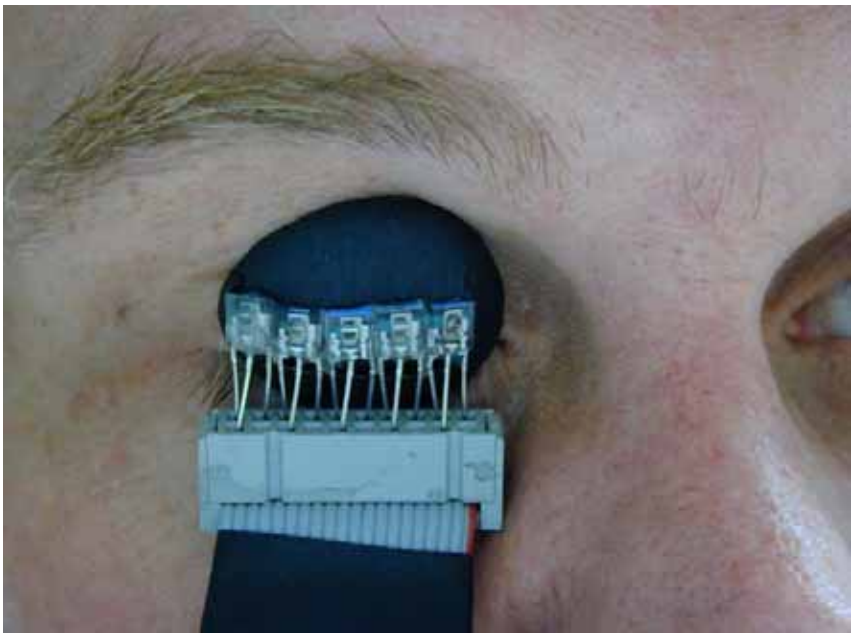

Figure 3.1:

First Generation Sensor Array

This first generation array had many improvements on the original concept, mainly the fact that it incorporated a curved plastic shell which would commonly be used in eyelid surgery to protect the eye and smaller active photodiodes. This shell was obtained from the Royal Victoria Eye & Ear Hospital, Dublin and served as the base upon which five Texas Instruments TSL-250 photodiodes were fixed, as seen on the left hand side of figure 3.2; also included in this figure is the shell and passive photodiode used for the research presented here.

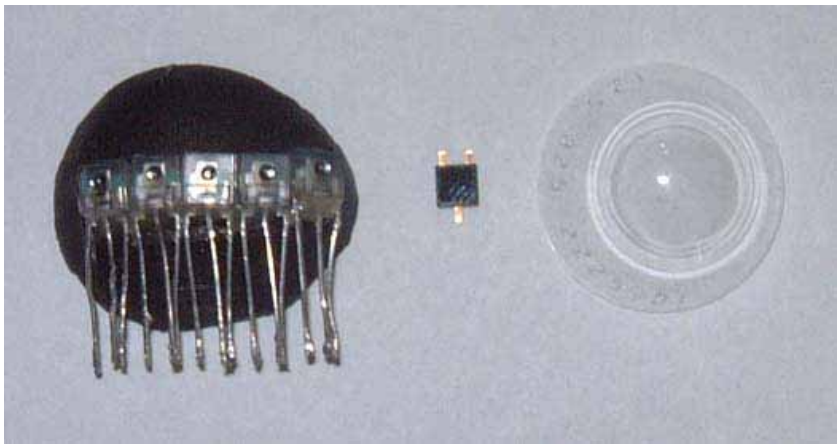

Figure 3.2:

First generation sensor array on left compared to second generation solar blind array components on right hand side.

The basic specifications of interest which resulted in the incorporation of the Texas Instruments photodiodes were their physical size, ability to measure ultraviolet wavelengths from 300 nm upwards, and their larger field-of-view. As such, they served favourably for initial measurements which were laboratory-

based. Their specifications were the most desirable of similar specification photodiodes available at the time.

For *in vitro* testing of the first generation array, a test-environment (1 m^3) lined with white paper, to simulate a uniform light field was purposely constructed. A small hole was punctured at one face of the test-box, over which several sheets of paper were attached, and a tungsten lamp was situated just outside this test-environment. This lamp provided light from approximately 360 nm to around 2 μm and the arrangement diffused the light such that it was more uniform within the box. A Styrofoam mannequin head was placed at the entrance to the test-box for initial measurements with the sensor array placed upon the right eye, and a black cloth was draped over the entire system. For human test subjects, a headrest was positioned at the entrance to the diffusing test-box with the array clamped in place. For both mannequin and human test subjects, the actual on-eye light field was recorded firstly, and the background light field was recorded by moving the head away from the sensor array.

With this system, the fundamental aspects of sensor design for ocular light field measurements were achieved. As with all research and development, there were inherent flaws, which were primarily due to the photodiode specifications. They had a broad spectral response, from 300 nm to 1100 nm and since the skin has a different reflectivity in the UV region of the spectrum than it does in the visible, visible light being reflected from facial structures onto the nasal side of the eye caused a signal that was not indicative of the actual levels of damaging

UVR striking the anterior surface. Another drawback was that the TSL-250 photodiodes required an external power supply, which, along with the ground and output pins, and wiring, increased the bulk of each photodiode. Finally, each of the five photodiodes set onto the plastic shell had their own plano-convex lens, causing light incident at oblique angles to focus on the active area, subsequently providing an unrealistic measure of the amount of light which would actually be incident across the palpebral fissure in an insolation environment. A flat detector is a closer approximation of the ocular surface than one with a lens above the detecting surface. An important consideration in trying to approximate the field of view and response of the ocular surface with a mechanistic sensor is whether the latter is a true representation of the former.

3.3 Current UVR sensor array design and construction

The novel solar-blind sensor array designed, constructed and tested for the research described here was based upon a Cantor & Nissell scleral lens. It was a spherical shell type and mimicked the curvature of the human eye more closely than the first generation plastic shell as can be seen in the superimposed photograph in figure 3.3. The current shell was made from a medical grade plastic with back optic radius of 8.25 mm, a scleral radius of 14.00 mm and a diameter of 23.50 mm, thereby mimicking the anterior ocular structures. These are designed to cover the whole of the ocular surface as pre-formed fitting shells as can be seen in figure 3.3. Being multipurpose and made from medical grade plastics, they can be

utilised by an optician to assist such diversities as surgery, disease, trauma or physical protection of the eye post surgery[449] [450].

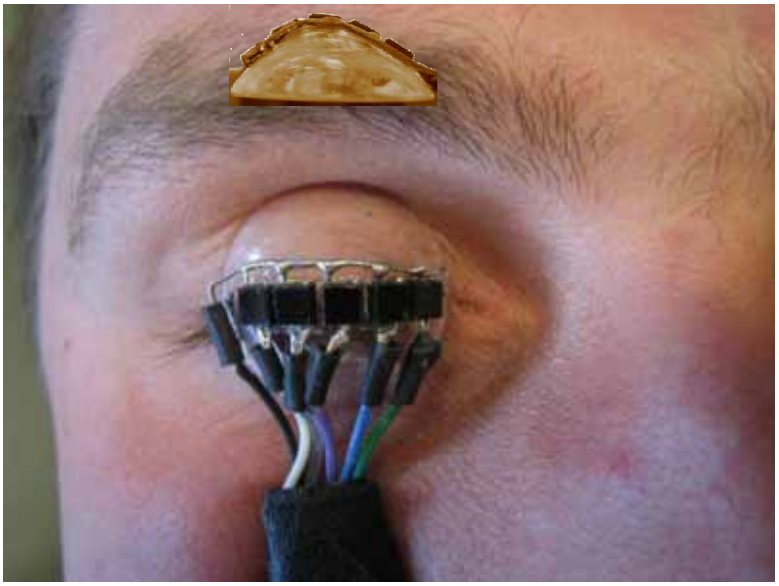

Figure 3.3:

Solar-blind sensor array with sensor 1 at temporal portion and sensor 5 at nasal portion. Curvature illustration is superimposed.

The full specifications of the Hamamatsu G5842 photodiodes are provided in Appendix I, however there are a range of other specifications pertinent to this research that also require consideration. Including their electrical contacts, the dimensions of the surface mount photodiodes are 6.5 ± 0.2 mm x 4.0 mm, with thickness 1.5 mm. Since the front surface of the eye exposed when the lids are open is elliptical, the horizontally exposed tissue, that is, from temporal to nasal canthus, is approximately 25 mm. This permitted five photodiodes to be placed across key areas of the exposed ocular tissue, as shown in figure 3.3. The centre

sensor was mounted over the corneal apex, with two photodiodes extending either side of this, covering the temporal and nasal limbal and conjunctival tissues further outwards. Since the active area of each individual photodiode was 0.8 mm x 0.8 mm, located centrally in the base and filter, the five-element array extended 20 mm across the ocular tissue.

Due to the G5842 photodiode's specifications best suiting the novel sensor system requirements, such as responsivity to the UVR waveband only, large field of view, large dynamic range and linearity across anticipated UVR irradiance levels during late summer at noon in Texas (maximum ~ 50 W m^{-2}), Hamamatsu G5842 Gallium-Arsenide-Phosphide photodiodes were chosen as the sensing device to measure the terrestrial solar UVR irradiance at the palpebral fissure. These had a number of advantages over similar photodiodes available and the previously used TSL-250's, primarily, the combination of their size, their field of view, being passive devices, as opposed to the active TSL-250 type, and the fact that they are solar-blind, i.e. their spectral response is solely in the UVR region from 260 nm to 400 nm, with peak sensitivity at 370 nm, as shown in figure 3.4 with a Solar Light Co PMA2107 A+B UVR radiometer. Measurements taken by the PMA2107 A+B detector were non-weighted and the relative response is given in figure 3.4. This detector had a spectral response over a similar spectral range to that of the GaAsP photodiodes, 260 nm – 400 nm, but their sensitivities were different per nanometre.

Figure 3.4 shows the G5842 photodiode's relative spectral response over the range 260 nm to 400 nm compared to an ideal flat response, and a Solar Light Co. PMA2107 UVA+B broadband radiometer, which was used in conjunction with the solar blind photodiodes during field based measurements. Using an absorption filter that eliminates portions of the visible that the photodiode semiconducting material alone is sensitive to, these photodiodes only detected ultraviolet photons within the 260 nm to 400 nm waveband. This feature was important when making UVR measurements in sunlight as the solar irradiance spectrum increases rapidly from ~ 300 nm in the UVR region to a maximum at around 500 nm in the visible region as shown in figure 1.1. The photodiodes could therefore quantify the relatively low UVR irradiance levels in the presence of the spectrally adjacent high visible levels.

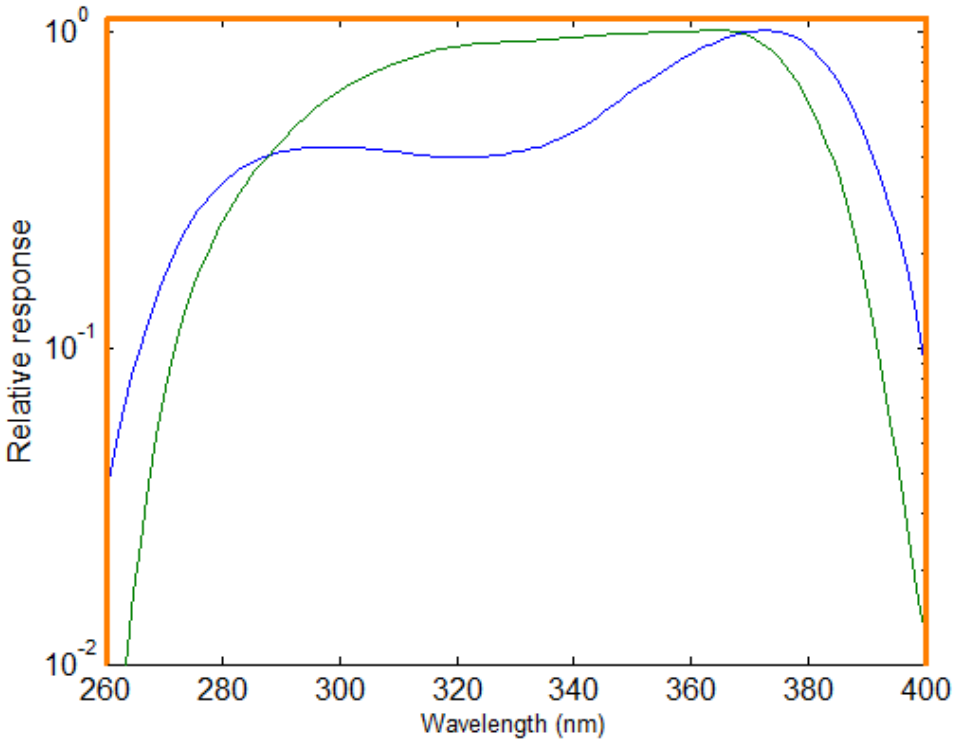

Figure 3.4:

Spectral response of Hamamatsu GaAsP photodiodes used in solar-blind sensor array (blue) and Solar Light Co. PMA2107 UVA+B broadband radiometer (green) compared to ideal flat response (orange line).

As described earlier, an ideal photodiode sensor will have a flat spectral response over a desired spectral range, as depicted in orange in figure 3.4. After a thorough search, the chosen photodiodes, when compared to others available at the time, were deemed to have the optimum specifications, principally the solar blind spectral response in the UVR waveband and large field of view.

In addition to measuring the ocular light field with the purposely designed sensor array, it was necessary to cross calibrate sensor output voltage levels with a

calibrated broadband radiometer so that the digitised analogue voltage output from the solar blind sensors could be related to the irradiance falling on them. For this, a NIST traceable portable Solar Light Co. PMA 2100 radiometer, with sensor PMA2107 A+B, was used to measure the absolute ambient irradiance levels. The five analogue voltage outputs from the photodiode array digitised by the data acquisition card could then be related to irradiance by cross-calibration between the photodiode array and UVR radiometer. A cross-calibration factor was calculated relating the irradiance and the sensors output voltages by locating the radiometer and the centre photodiode adjacent to each other and facing the zenith at approximately two hours either side of noon under diffuse/direct sunlight in Houston, Texas. This permitted simultaneous measurements to be taken from the photodiode array and radiometer under various sky conditions with fluctuating irradiance values, thereby permitting the cross calibration to be measured over a wide range of irradiances similar to the levels when used to measure the ocular UVR field. The resultant conversion factor of 25 W m^2 per sensor volt was given by the slope provided in figure 3.5.

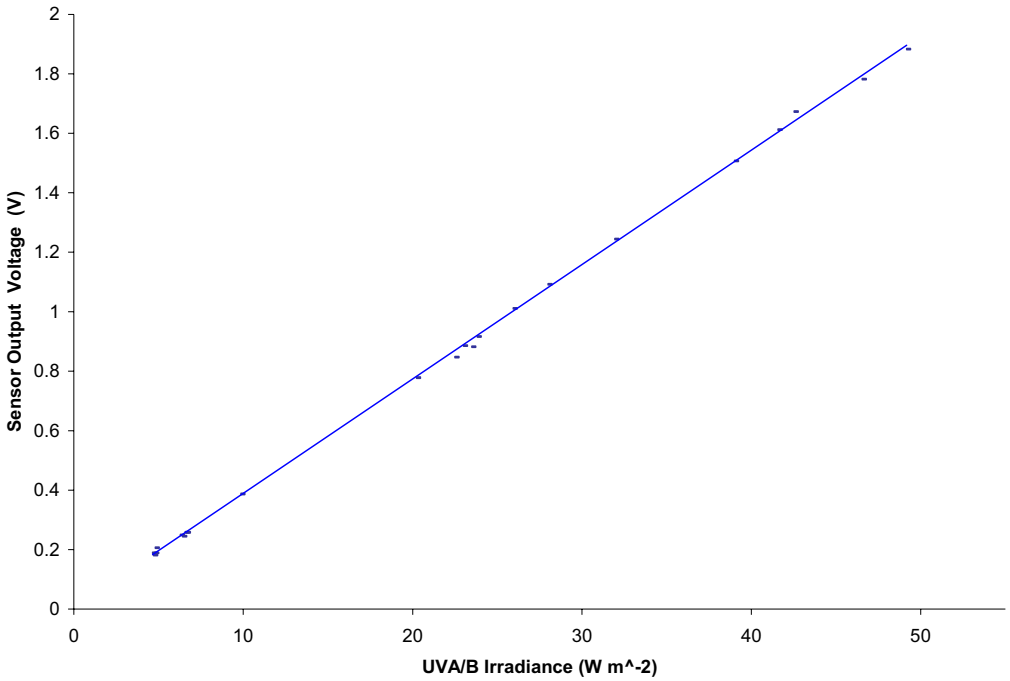

Figure 3.5:

Cross calibration of photodiode output voltage with calibrated UVA/B radiometer.

The photodiodes specified photosensitivity of 0.06 A/W at 370 nm meant that a corresponding solar irradiance value of 1 W/m^2 would produce 0.04 V across a 1 MΩ resistor, given their active area is 0.8 x 0.8 mm. Therefore, if there was the same A/W over the 140 nm spectral response range of the detector, and assuming 1 W m^2 at all solar UVA-B wavelengths, one would expect an overall signal of 3.8 V which correlates well with the 0.04 V/W signal from the detector.

To avoid saturation, ensure a linear response and maintain high photon conversion efficiency, the photodiodes were wired in a reverse bias circuit, as shown in figure 3.6 powered by the 5 V PCMCIA output from a laptop PC. In

forward bias mode, the dynamic range of the photodiode was exceeded by the intense levels of UVR presented in Texas, and saturation resulted.

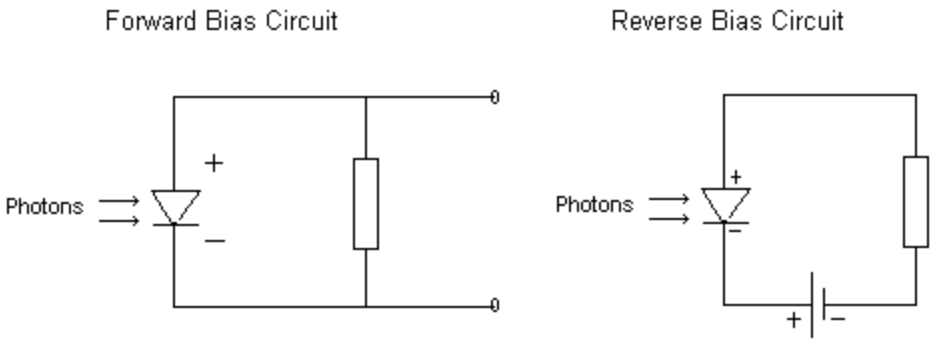

Figure 3.6:

Schematic of typical forward and reverse bias photodiode circuits

The G5842 sensor's field of view can be seen in figure 3.7, as quoted by the manufacturer. As with many optical sensing devices, such as broadband radiometers and optical fibres, peak sensitivity occurs when a source is normal to the sensors surface, with sensitivity falling off at more oblique angles. For the sensor employed for this research, the fall off in sensitivity is primarily attributable to Fresnel reflection from its specularly reflecting surface. Analogous to reflections from this mechanistic device are reflections from the exposed ocular surface itself. At more oblique angles, the ratio of corneal transmission to reflections from its surface will change. The more oblique the angle of incidence, the greater the reflectivity from the corneal surface. Related to such reflections from the corneal dome is PLF, and for this reason, PLF only occurs within a narrow range of angles, just temporally oblique from the cornea. Outside of this

range, most incident radiation is reflected from the corneal surface and does not refract across the aqueous humour.

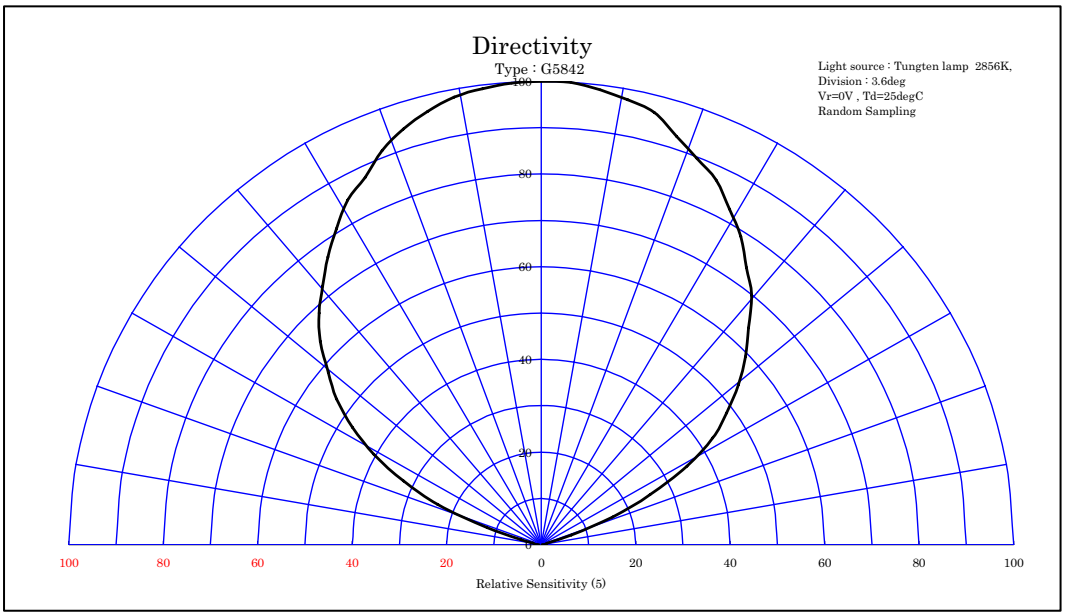

Figure 3.7:

Hamamatsu GaAsP G5842 photodiodes

sensitivity to the UVR waveband only over field of view.

In addition, prior to being attached to the shell, the relative response of each photodiode in the array was tested in the laboratory by placing each in the same UVR field for ten measurements, as this was considered sufficient to measure any variations in sensor responsivity across the array. As such, the variations in the measured response across the array were found to agree to less than 1 % variation and this variation can possibly be attributed to an inability to exactly place the sensors in the same location for each recorded measurement.

3.4 LabVIEW Data Acquisition

The National Instruments (Austin, Tx) LabVIEW data acquisition suite serves as a most efficient tool for acquiring and presenting data using the principles of virtual instrumentation. A virtual instrument consists of a standard PC workstation which hosts powerful application software that takes advantage of the computing power and connectivity capabilities of such stations. These are interfaced with a measurand-specific sensing device and perform the functions of traditional instruments such as dataloggers or oscilloscopes with greater flexibility and control. As it is a graphical development environment, the need for reams of code is now replaced by a user-friendly graphical interface consisting of a front panel and block diagram. The former consists of controls and indicators, while the latter contains the graphical code.

A LabVIEW program was written specifically to allow real time ocular UVR field measurements to be made. The program was written such that it had a variable sample rate, but the highest possible rate, determined by the processing speed of the computer in tandem with the acquisition speed of the data acquisition card, was always chosen to account for the rapidly varying atmospheric conditions. A DAQCard-700 was used as the analogue to digital interface and its maximum sample rate was 100 kHz. As there were five photodiodes comprising the ocular sensor array, this maximum sample rate was separated into five maximum sample rates, which resulted in each sampling at 20 kHz. This sampling rate permitted an excellent signal to noise ratio and invariably had the ability to

measure rapidly varying UVR levels in an ambient insolation environment. For all field–based measurements recorded, data was recorded for 10 seconds; 5 seconds on, and 5 seconds off the eye. Along with the sampling rate of 20 kHz, it was determined that this measurement duration was sufficient to permit as many samples to be taken as possible, in as short a timeframe as possible, to acquire UVR levels both on and off the eye, under a perceivably uniform insolation environment. In cases where the UVR levels varied over the course of measurement, as recorded by the calibrated UVR radiometer, these measurements were simply re-taken.

Figure 3.8 shows the block diagram for the program. The AI Acquire waveforms acquires data from the specified channels and samples the channels at the specified sample rate, the output of which is sent to an index waveform array. This selects one waveform out of an array of waveforms by array index or channel name. It does so in the order specified by the user, and wires data directly to a waveform graph, where it is displayed on the front panel as a varying voltage signal. The elements of the 2-D array are transposed just before being saved for ease of use when analysing in Matlab.

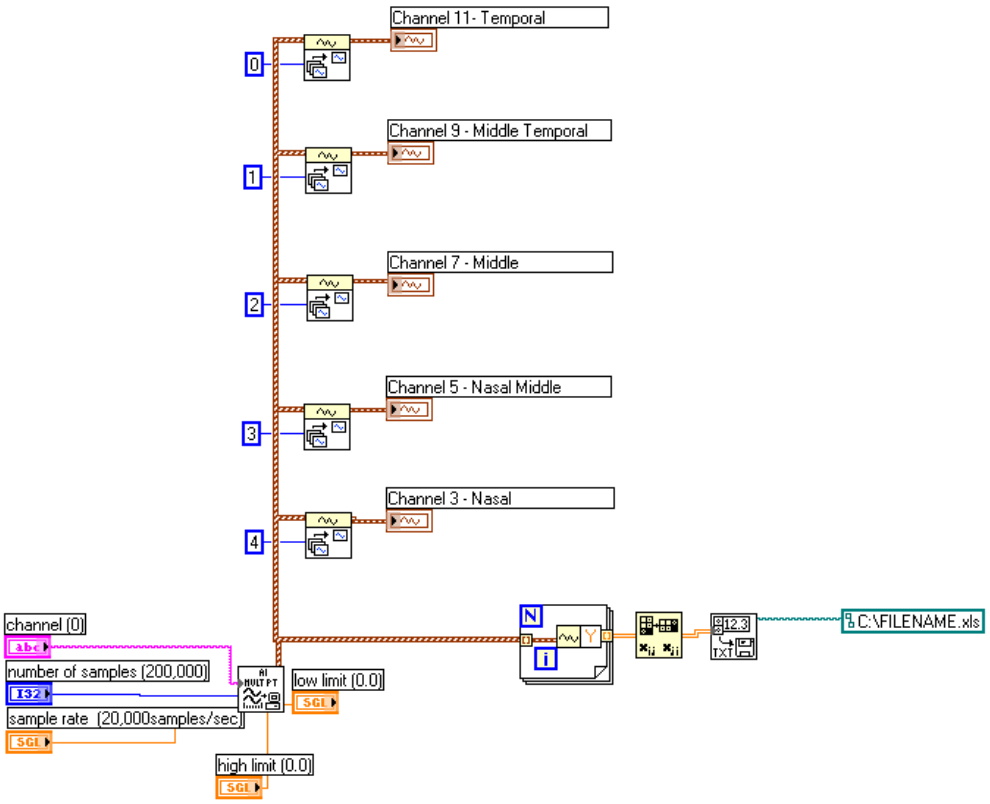

Figure 3.8:

LabVIEW Block Diagram which acquires real-time field based measurements.

The Front Panel user interface which displayed the voltages from the array is now shown in figure 3.9. Each sensor's voltage was displayed individually within the given waveform charts. The benefit of this was to ensure that no malfunctions occurred during a given acquisition, as after each, the five voltages over the course of a ten second measurement were displayed for user-analysis, prior to more data being acquired.

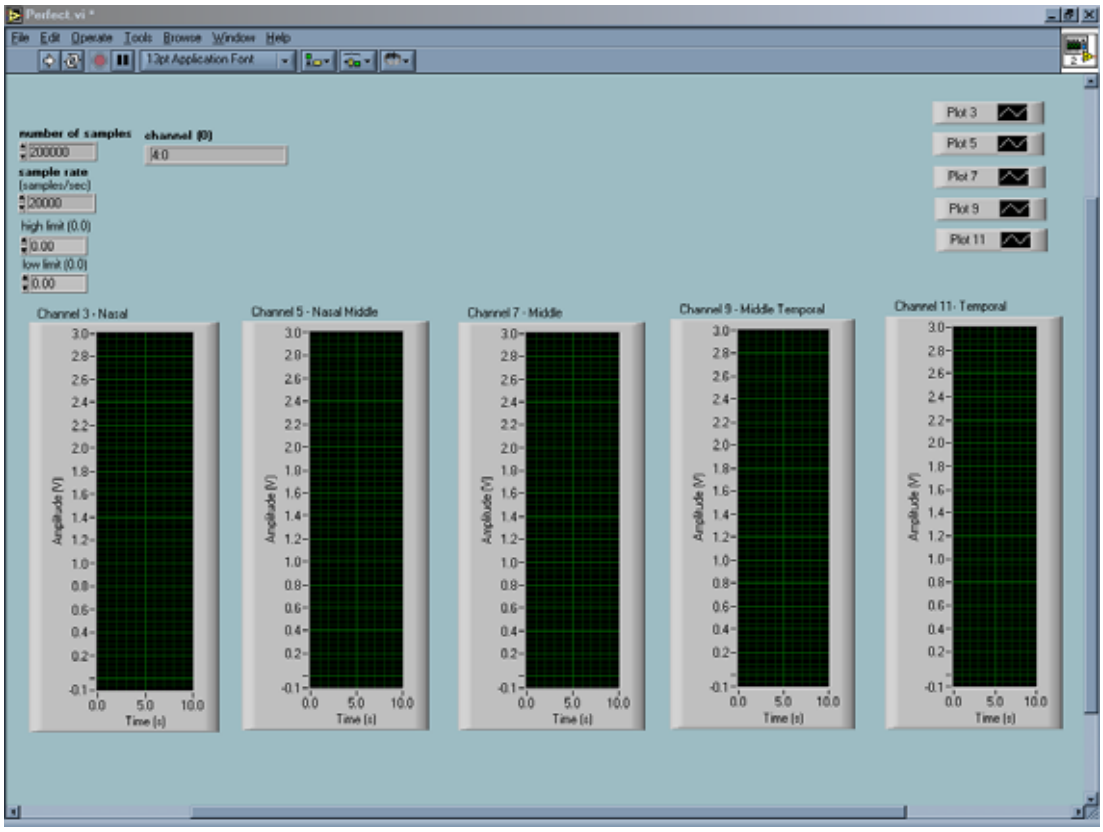

Figure 3.9:

LabVIEW Front Panel display which provided graphical representations of varying voltages across array from nasal to temporal sensor.

3.5 Laboratory Based Photodiode Testing

To quantify the ocular UVR field in an insolation environment, a purpose designed photodiode sensor array was constructed and tested. Initial measurements and characterisation of the photodiode array were carried out in the laboratory in DIT, and the field methodology used in Houston, Texas, was tested

on the roof of the Facility for Optical Characterisation and Spectroscopy (FOCAS), DIT.

Due to the anticipated levels of irradiance in Houston towards the end of summer (~ 50 W m^{-2}), it was necessary to test the photodiodes in both forward and reverse bias under similar irradiance levels as those typically found in Houston. To do so, a Q-Panel Xe-1-C solar simulator was used to irradiate the photodiodes as it had a spectral power distribution resembling that of solar UVR at a summer's midday near the equatorial latitudes. It was found that by reverse biasing the photodiodes, their dynamic range increased permitting the measurement of irradiance without photodiode saturation.

3.6 Houston field based measurements

As there are much higher yearly average levels of UVR at latitudes progressing closer to the equator, accompanied by expected clearer skies in general, field based measurements were carried out with the aid of Dr James Walsh and Prof. Jan PG Bergmanson at the Texas Eye and Research Technology Centre (TERTC), University of Houston College of Optometry, Houston, Texas. Measurements were taken on consecutive days during August/September 2004 and early August 2005. Expected clear skies in Houston for these times of year proved to be quite intermittent, which ultimately allowed investigation of the ocular UVR field for a range of different orientations with respect to the zenith

and intercomparison of the variation in these ocular UVR field for direct and diffuse insolation environments.

By comparison with Dublin (53° 20' N, 6° 18' W, altitude 85 m above sea level), Houston, (29° 45' N, 95° 22' W, altitude 40 m above sea level) is appreciably closer to the tropics, which themselves lie between 23° 30' north and south of the equator, and is well within the 'pterygium belt', which spans from the equator to approximately 30° – 40° north and south[451].

Chapter 4

Novel Photodiode Array Field Results

4.1 Introduction

Many previous measurement systems designed to quantify the ocular exposure to terrestrial solar UVR incorporated mannequin heads, as highlighted in section 2.2. As mannequin heads have been used extensively in these other studies, it was thought that the design and ease of use of this novel sensing system, along with the use of human heads, would give a more realistic measure of the UVR intensities across the anterior ocular surface. The use of mannequin heads and interpretation of field results gained through their incorporation in dosimetric studies is very limited. Although much better models are available these days, with varying facial structures resembling different ethnic groups, they could still be considered anatomically imprecise, as they are only representative of what is perceived to be an average ethnic facial structure. Coupled with this is the mannequin's albedo. The reflectivity of human skin is highly individualistic, and such factors as perspiration will come in to effect also. The use of a single mannequin head could ultimately lead to misleading results. Therefore two human test subjects were used for field based measurements.

4.1.1 Field based Measurements Environment

Two Caucasian males, Dr. James Walsh and Mr. David Fleming were test subjects A and B respectively for the field-based measurements recorded and presented in this thesis. The solar UVR field at the ocular surface for a range of orientations under direct and diffuse skies was measured, highlighting the variation in irradiance at the anterior ocular surface due to differing facial structures. The Facial structures can be seen in figure 4.1. It can be seen that there is only a slight difference in facial structure around the brow ridge, with test subject A on the left hand side having a more deeply set eye, thus potentially greater protection from solar rays.

Figure 4.1:

Test Subject A on the left and B on the right hand side highlighting test subject B having a more protrusive eye socket.

The repeatability of the sensor array was also demonstrated under different conditions, emphasising its strong potential in the field. All field-based measurements were carried out on the roof of the Texas Eye and Research Technology Centre (TERTC), Houston. Due to the distances between this building and the surrounding ones, the view of the entire sky from this rooftop was considered to be free of obstruction, as seen in figure 4.2. Measurements were always recorded under totally clear skies or under skies with perceivably uniform cloud cover and were taken at the centre of the roof.

Figure 4.2:

The roof of TERTC with an unimpeded view towards the foreground and horizon.

For all data recorded, the photodiode sensor array was always worn on the right eye of both test subjects A and B since the shell used was specific to the right eye, with sensor number 1 to the temporal side of the sagittal plane and

sensor number 5 to the nasal side. The system was operated by both test subjects. While one subject wore the sensor array, correct alignment and orientation was verified by the other while also operating the specifically written LabVIEW acquisition program. For every orientation recorded and presented, five sample data measurements were made per cardinal point orientation for a given data set. The reason for taking no more than 5 samples per orientation for each test subject was that the time spent outdoors would have been too long in the intense heat and humidity with no shade, and 5 samples per orientation was found to be enough to compute good standard deviations of the data sets. Potential sources of measurement error were due to ambient light level variation, head movement and in particular sensor placement. To monitor ambient light levels the Solar Light PMA2107 UVA+B radiometer was always used in tandem with the array. Any changes noted on the radiometer during a measurement run resulted in that data set being discarded and re-started. To minimise head movement, the test subject relaxed prior to measurement and as stated, the array positioning at the ocular surface was checked by the other test subject.

4.1.2 Field Based Study Expectations

Before the field results for both test subjects are presented over a complex range of cardinal point orientations for different solar zenith angles and under direct and diffuse skies, it is important to consider what general trends might be expected across the sensor array. The following list narrows down the many environmental and physiological factors which, when combined, cause large

variations in irradiance across the anterior ocular surface. This list is not definitive due to the nature of the countless environmental variations (and combinations thereof) that occur, which ultimately affect the intensity and distribution of solar UVR across the anterior ocular surface.

4.1.2.1 Direct Irradiance

1) Absolute data should be dominated by facial anatomy and the test subjects orientation to the sun and solar zenith angle, except where there is considerable shading and/or field of view variations in specific direction, e.g. trees and buildings in the surrounding foreground and vastly varying UVR reflectances of nearby objects.
2) Facing due south at local noon, one would expect data recorded off-eye (i.e. the background UVR levels) to show a trend where the centre sensor is irradiated greater than the two adjacent sensors, at the temporal and nasal limbal locations. Further still, adjacent to these limbal sensors, one would expect the most temporal and nasal sensors to be irradiated least, assuming no objects in the foreground alter the solar UVR field.
3) For data recorded with the array on the eye under similar conditions, one would expect the nasal sensors to be shaded by the brow ridge and nasal anatomy, with the temporal sensors recording the highest irradiances.

4) By calculating the relative intensity, which is on-eye data divided by the off-eye data, it is possible to quantify the effects the facial structure has on the distribution of solar UVR across the palpebral fissure. One would expect the relative intensities to be similar for a particular subject regardless of sky conditions and cardinal point orientation as it is subject specific.

5) There are therefore two ocular biases which can be examined. The environmental bias which gives the irradiance at that time across the eye and the relative bias which gives the irradiance variation across the eye by eliminating the variations of the background radiation field. In calculating the relative intensity, it is found to be subject specific.

Having outlined what one would expect under direct insolation, the following is a list of what might be expected under diffuse skylight:

4.1.2.2 Diffuse Irradiance

1) Lower solar UVR irradiance than under direct insolation, although it is important to note the values as they will be incident on possibly less protected ocular tissue as protective measures and squinting may be reduced.
2) Less variation in irradiance between the four cardinal point orientations.
3) Less variation in irradiance across the sensor array than under direct insolation due to the absence of direct solar component, resulting in a

more uniform distribution of irradiance across the array. This is suggested to be true of completely uniform diffuse cloud cover. However, as sometimes occurs, portions of the sky may be perceivably brighter, particularly when the sun is present in this area.

4) Similar variations in the relative intensities as under insolation due to head anatomy dominating the relative intensities, thus showing that a persons facial anatomy is a major determinant in ocular UVR dose.

The preceding list is what one would expect in the data that follows.

4.2 Example data for zenith facing field measurements

In order to present data of the measured irradiance levels at the human eye for a range of different environmental conditions, it is important to present the maximum possible irradiance at the ocular surface, as it is these values which other measurements will be compared against to show the difference between looking towards the horizon and zenith. The maximum possible irradiance expected at the ocular surface would be while lying down, looking towards the zenith at local noon. Any measurements of ocular irradiance taken while looking towards the horizon would not be expected to surpass this zenith facing data, as the brow ridge should provide some protection from the direct rays and related Fresnel reflections would be expected from the surface of the photodiodes also.

Unfortunately, measurements were not taken at local noon whilst facing the zenith, due to time constraints and more significantly, changing environmental

conditions. Due to intermittent cloud cover during the field measurement period in Houston, the best possible sets of direct or diffuse data were recorded at times when reasonably consistent direct/diffuse skies were presented. However, the methodology and reasoning behind zenith facing measurements is described, and the reliability and repeatability of the instrument is borne out through the figures presented for this data, prior to data presented for test subjects fixated on the horizon.

One set of digitised data from each of the five sensors are shown in figure 4.3 for a measurement duration of ten seconds as defined in the specifically written LabVIEW program. The sensor array was held directly on the closed right eye for the first five seconds of the recorded data and the test subject's head was then moved back from the array for the final five seconds, thereby quantifying the background or reference UVR levels, since shading by the brow ridge and nose were eliminated due to their being no head present. The order in which the individual photodiode outputs are displayed in figure 4.3 and all subsequent figures is given in table 4.1:

Sensor Position	**Sensor Colour**	**Sensor Number**
Temporal	Blue	1
Temporal-Middle	Green	2
Middle	Red	3
Nasal Middle	Cyan	4
Nasal	Magenta	5

Table 4.1:

Sensor Array Reference Table.

The unstable voltage regions at the crossover point, where the head was moved back, were not used in any calculations. However, the stability of the system under constant direct sunlight can be clearly seen through the raw voltage data shown in figure 4.3, and the stable off-eye levels compared very well to the un-shaded radiometer values recorded which was placed a distance of five meters from the test subject and oriented skywards. It was placed this distance away so that any movement by the person recording the data behind the test subject did not cause shading.

The sample output data from the array provided in figure 4.3 for test subject A was recorded at approximately two hours before local noon due to there being extremely clear skies, with the test subject looking directly towards the zenith, or in the supine position, for a southern facing aspect. At this time and date, the solar azimuth and solar elevation angles proceeded from ~ 123º to ~ 134º

and ~ 56º to ~ 61º respectively. These angles were found at the National Oceanic and Atmospheric Administration (NOAA) Surface Radiation Research Branch website[452]. At these solar coordinates, for a test subject, with the sensor array worn on the right eye and looking towards the horizon for a southern facing aspect, one would expect a nasal bias across the array as the direct rays originate from this portion of the sky. While lying down, the nose would not be expected to protect the nasal aspect for these solar coordinates as the sun is progressing closely towards its zenith. This is true of the data presented in figure 4.4, where there is a pronounced nasal bias.

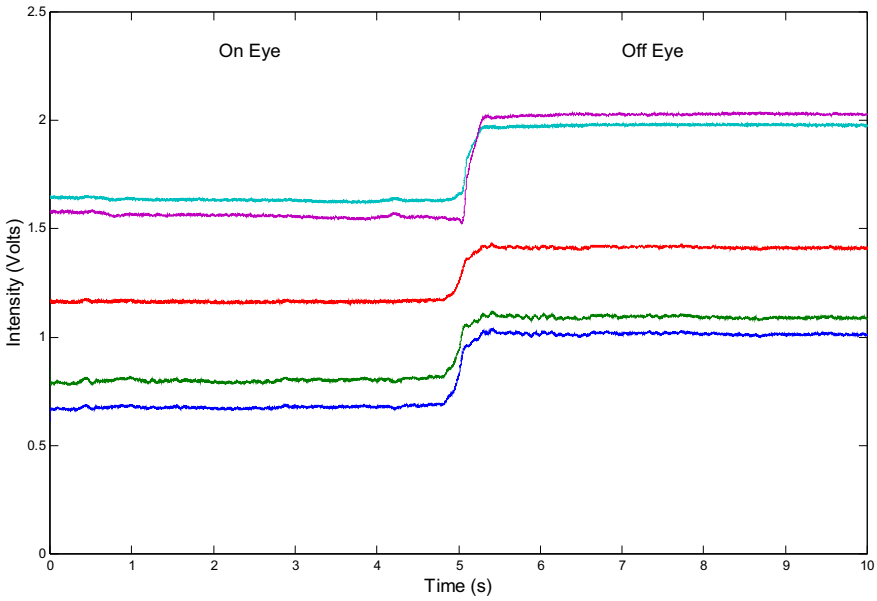

Figure 4.3:

Sample photodiode array output voltages of test subject A facing the zenith at 11.30 am under direct insolation.

4.2.1 Calibrated Mean Absolute Zenith Facing Irradiance Intensities

Using the calibration factor of 25 W m^{-2} / V calculated in section 3.3 it was possible to determine the mean absolute UVR irradiance values for each photodiode and plot these values as a function of photodiode number and irradiance level in W m^{-2} for on and off the eye.

Figure 4.4 shows the calibrated mean absolute UVR irradiance values of the raw data for direct insolation, with the sensor array on and off the eye while subject A looked towards the zenith for a southern facing aspect. The black dashed lines are the calculated mean absolute UVR values of five measurement runs with the sensor array on the eye, while the blue dashed lines are the absolute background levels across the array after the head was removed. The five measurement runs presented here highlight the repeatability of the measurement method. The photodiode output voltage presented in figure 4.3 was one of five data sets used to produce figure 4.4.

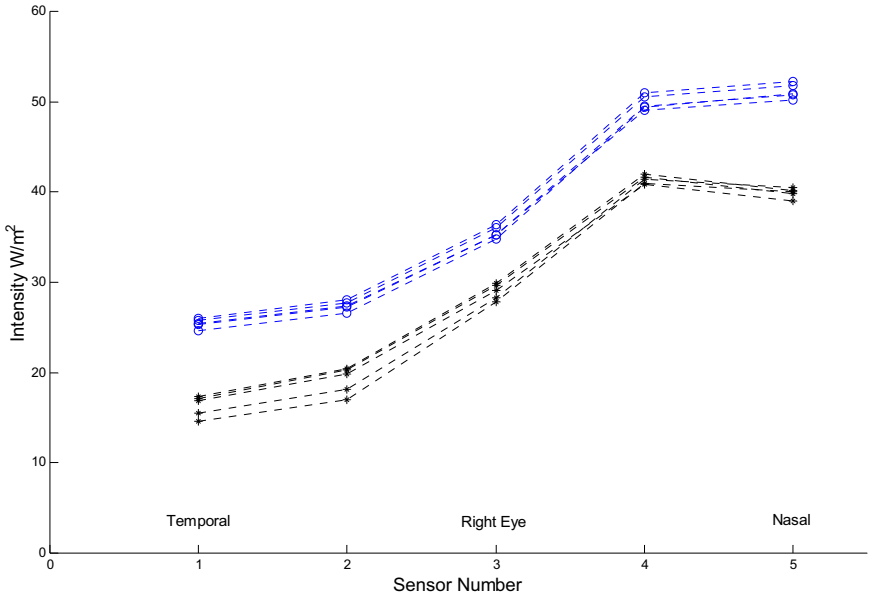

Figure 4.4:

Calibrated mean absolute irradiance values of raw data for test subject A, off (Blue) and on-eye (Black), facing the zenith for the southern aspect.

As anticipated under direct insolation for the sensor worn on the right eye, due to the south-easterly position of the sun, the nasal photodiodes received a greater irradiance than the temporal photodiodes, as can be seen in figure 4.4. This was expected of the zenith facing array as the nasal photodiodes were illuminated more so than the temporal ones both on and off-eye, with the former exhibiting minimal nasal and brow shading, and the direct rays being more normal to the nasal photodiodes surfaces than those of the temporal ones. Off-eye, one would expect no shading at all, and thus a higher irradiance was found. The trends for both the on-eye and off-eye data are very similar, with a more or less uniform decrease in intensity across the entire array, attributable to brow shading above that of nasal shading, the latter of which would have resulted in a flatter trend if it

dominated. From the on-eye data, it can be seen that sensor 4 received 40 W m^{-2} with the irradiance falling off dramatically across the curvature of the sensor array as the sun ascended towards its diurnal peak. Figure 4.4 demonstrates how effective a tool the array is in determining solar UVR levels at the ocular surface.

Figure 4.5 provides the observed trends for test subject A looking towards the zenith at two hours pre-local noon for the four cardinal points. **For each data set and all subsequent data sets, starting at the top left, and progressing clockwise, the orientations are East, South, North and West.** The data for the southern aspect was computed using the data presented in figure 4.4. The error bars were calculated from the standard deviation around the mean for the five sets of readings taken and indicate statistically significant variations across the array. The black error bars are on-eye values and the blue error bars are the off-eye values or background levels.

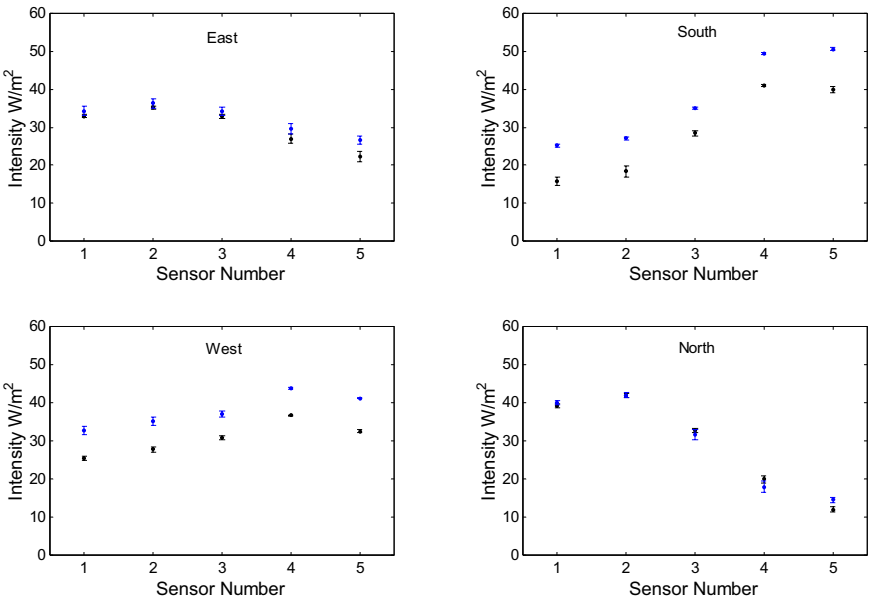

Figure 4.5:

Calibrated mean absolute irradiance values for test subject A, off and on-eye, facing the zenith for the four cardinal points 2 hours pre-local noon.

In figure 4.5, sensors 1, 2 and 3 received a greater UVR irradiance on-eye than 4 and 5 with the trend dropping off nasally for the eastern aspect. This would also have been expected due to the solar azimuth being south-easterly, and the direct rays irradiating these sensors more normal to their active surface than the more nasal ones, which were afforded a certain degree of protection due to the curvature of the shell and the sun being ~ 30º from zenith.

For the western aspect, sensor 4 received the greatest irradiance with the general trend falling away temporally. This also would be expected considering the south-easterly azimuth of the sun and the fact that the sun was not yet high enough to illuminate the temporal side of the array. It can be further explained by

forward reflections from the nasal and brow ridge concentrating UVR towards the nasal region. The northern oriented on-eye data highlights a trend peaking at sensor 2 and falling off nasally. For the given azimuth angle range, this would also have been expected due to sensors 1 and 2 being illuminated mostly, and sensors 3, 4 and 5 being progressively more shaded by the brow ridge and receiving less irradiance due to the array curvature. Taking the middle sensor, the average on-eye irradiance value for the four orientations was approximately 30 W m^{-2}, with the off-eye data only slightly greater for the southern and western aspects. From figure 4.5, it is clear that the irradiance across the ocular surface whilst looking skywards, with the sun not quite at zenith, is a result of the combination of the solar position, cardinal point orientation, and facial shading,

4.2.2 Relative Intensities For Zenith Facing Field Measurements

Figure 4.6 compares the relative light field across the eye for test subject A for the four orientations presented in figure 4.5. The relative intensities are calculated by dividing the off-eye values presented in figure 4.5 into the on-eye values, essentially therefore, eliminating the background, or reference, and leaving one with the relative intensity of solar UVR at the ocular surface for a particular SA, SEA, insolation environment and head carriage relative to all of these.

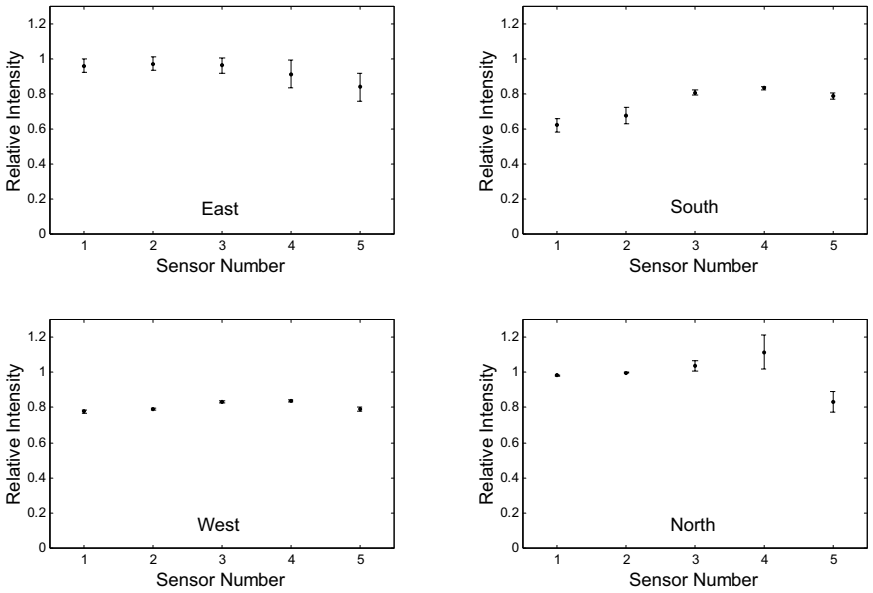

Figure 4.6:

Relative Intensities for test subject A facing the zenith for the four cardinal points 2 hours pre-local noon.

From figure 4.6 it can be seen that for all aspects, the largest variation in photodiode output signal across the sensor array occurs for the southern aspect, with a temporal bias for this orientation. East, west and north are relatively flat, highlighting that the ocular surface receives relatively comparable UVR intensities across the lid margin for these aspects due to less shading by the facial structures at this time of the day and under such atmospheric and environmental conditions.

4.3 Horizon Facing Measurements, Houston, Tx.

4.3.1 Introduction

Section 4.2 demonstrated the progression of output voltage from the five photodiodes, through calibrated mean absolute irradiance values, to relative intensities for test subject A lying down facing the zenith for the four cardinal points. A more natural head carriage is that of gazing towards the horizon standing upright. For this typical upright head carriage, the head's orientation with respect to the sun coupled with the solar angle under direct insolation are the dominant factors when assessing UVR levels at the anterior ocular surface. This can be explained by the fact that a horizontal surface is always receiving direct radiation; however, standing upright at local noon, a sensing device such as the array described here, is dominated by its orientation to the sun and solar angle, in which case one would expect a southern facing device to generate a higher output voltage than a northern oriented one in the Northern Hemisphere. It follows that both east and west oriented devices will be intermediary ones under direct insolation[453]. Under diffuse insolation, one would not expect radical differences in the irradiance trends across the array for a southern facing array, as the direct component is weaker or absent. It also follows that mean irradiance levels across the array should be more uniform for the four cardinal points as the diffuse nature of the irradiance dominates under uniform diffuse skies. After preliminary surveys, a substantial database of field results for this more natural position was acquired over the course of two field-based trips to Houston. These measurements

were recorded for test subjects A and B under both direct and diffuse skies and at varying times around local noon, which was approximately 13.20hrs for all measurements. In building up this database, variance in the calibrated mean absolute irradiance values and consequent relative intensities between test subjects under direct and diffuse insolation at different solar angles was analysed and is presented in sections 4.3.2 to 4.3.6. Along with the sensor arrays cardinal point orientation, the respective solar azimuth and elevation angles are also given for each figure presented as it is the combination these which govern the array trends found in the field.

Starting at approximately 2.5 hours pre local noon, figures 4.7 to 4.10 show test subject A looking towards the horizon until approximately 40 minutes post local noon under direct insolation. As already mentioned, due to variable weather conditions, measurements were taken on different days when there were definite direct or diffuse skies, and subsequently are now presented over time. Thus, the progression of the sun with respect to the four cardinal point measurements orientations can be analysed under direct insolation.

4.3.2 Test Subject A Irradiance Intensities - Direct Insolation

Figure 4.7 shows test subject A gazing towards the horizon under direct insolation at approximately 2.5 hours pre-local noon. At this time the SA and SEA proceeded from ~ 102º to ~109º and ~ 53º to ~ 60º respectively.

Comparing to test subject A in the supine position presented in figure 4.5 for the southern facing aspect, the off-eye trend is similar, albeit with a lower solar irradiance. Sensors 4 and 5 were illuminated greatest, which would be expected, given the solar position with respect to the array. The key difference between both southern oriented aspects presented in figures 4.5 and 4.7 is that the on-eye trend is actually lower nasally whilst standing (figure 4.7). This can be explained by the fact that the right eye brow ridge coupled with the surrounding facial anatomy prevented direct rays striking the more nasal sensors. As the SA and SEA are quite similar for both sets of measurements presented in figures 4.5 and 4.7, it can be concluded that for this orientation and time, the facial anatomy plays a huge role in preventing direct rays from reaching the nasal anterior surface, when compared to lying on one's back and fixating at the zenith, where the brow ridge protection is limited. Moving across the array more temporally for the on-eye data, there is a slightly higher irradiance than sensor number 5 for sensors 1, 2, and 3, which all receive a fairly constant irradiance, thereby further emphasising the degree of UVR reduction afforded by the brow ridge.

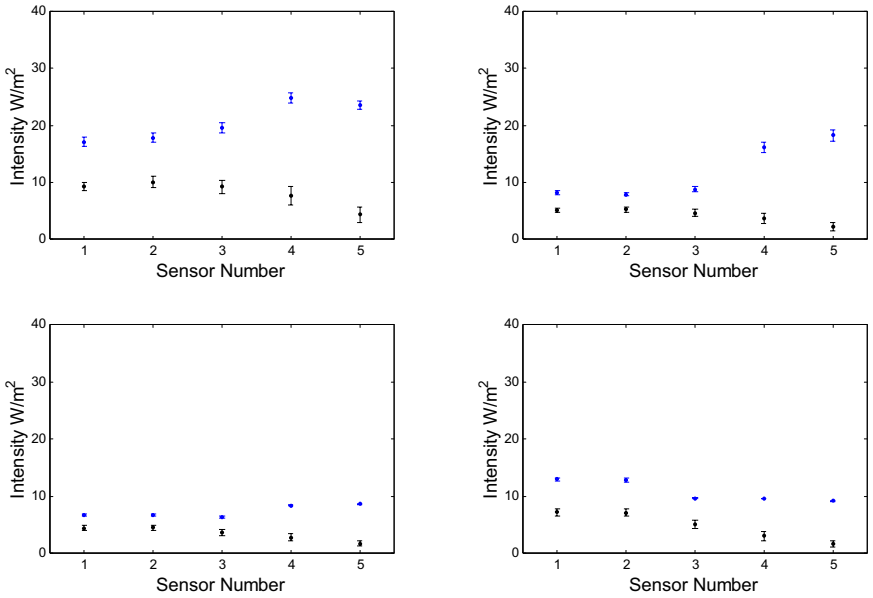

Figure 4.7:

Calibrated mean absolute irradiance values for test subject A, off and on-eye, facing the horizon for the four cardinal points ~ 2.5 hours pre-local noon.

Progressing clockwise from top left: East, South, North & West.

The off-eye eastern facing orientation in figure 4.7 shows sensors 4 and 5 receiving the greatest illumination. The on-eye trend for the eastern facing aspect shows the more temporal to middle sensors, namely 1, 2 and 3, receiving a larger irradiance than 4 and 5. This can also be explained by the SA and SEA. While facing due east, or 90º east, the sun was between ~ 102º and ~ 109º. This meant that the temporal sensors of the array worn on the right eye were illuminated more so than the nasal sensors.

Due to the sun being located more easterly in the sky, with the western sky exhibiting no real direct component, the resultant off-eye and on-eye irradiance

levels for the western facing aspect were much less than those for the eastern facing aspect in figure 4.7. They were also much flatter, with no significant trend to either the off- or on-eye data, notwithstanding the fact that the nasal sensors received a slightly lesser irradiance than the temporal ones on-eye. This can be attributed to no direct solar rays being incident at the array surface for both on-eye and off-eye, only scattered and reflected rays illuminating its surface. It can be further deduced that the brow ridge did provide protection from the ambient diffuse rays since the on-eye irradiance is less than that off-eye nasally.

The off-eye northern facing orientation in figure 4.7 illustrates that the temporal sensors receive a marginally greater UVR irradiance than the central and nasal sensors. When placed on-eye, this trend does not deviate much. The most significant difference is that similar to the western facing data; the nasal sensor is protected by the facial anatomy from the scattered and reflected diffuse rays.

Figure 4.8 presents test subject A gazing towards the horizon under direct insolation at approximately 2 hours pre-local noon. At this time the SA and SEA proceeded from ~ 113º to ~123º and ~ 61º to ~ 67º respectively. These angles are a progression towards local noon from those presented in figure 4.7. Very similar trends to figure 4.7 can be seen for all directions of sensor array orientation in figure 4.8, and most significantly, these trends and corresponding irradiance, while very similar, also exhibit higher irradiance values both on- and off-eye. As the difference in time was only 30 minutes between figures 4.7 and 4.8, these higher irradiance values show that the sensor array was very responsive to slight

changes in both solar azimuth and solar elevation angles across its horizontal diameter due to it measuring the increased direct irradiance due to the sun being higher in the sky.

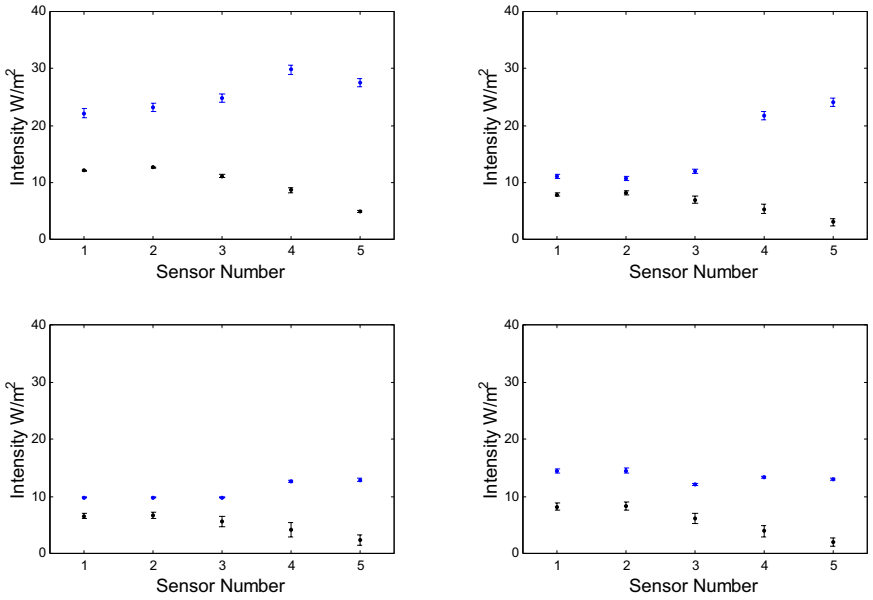

Figure 4.8:

Calibrated mean absolute irradiance values for test subject A, off and on-eye, facing the horizon for the four cardinal points 2 hours pre-local noon.

Progressing clockwise from top left: East, South, North & West.

Approaching 20 minutes pre-local noon, figure 4.9 presents test subject A gazing towards the horizon under direct insolation for solar azimuth and solar elevation angles proceeding from ~ 167º to ~176º and ~ 64º to ~ 66º respectively.

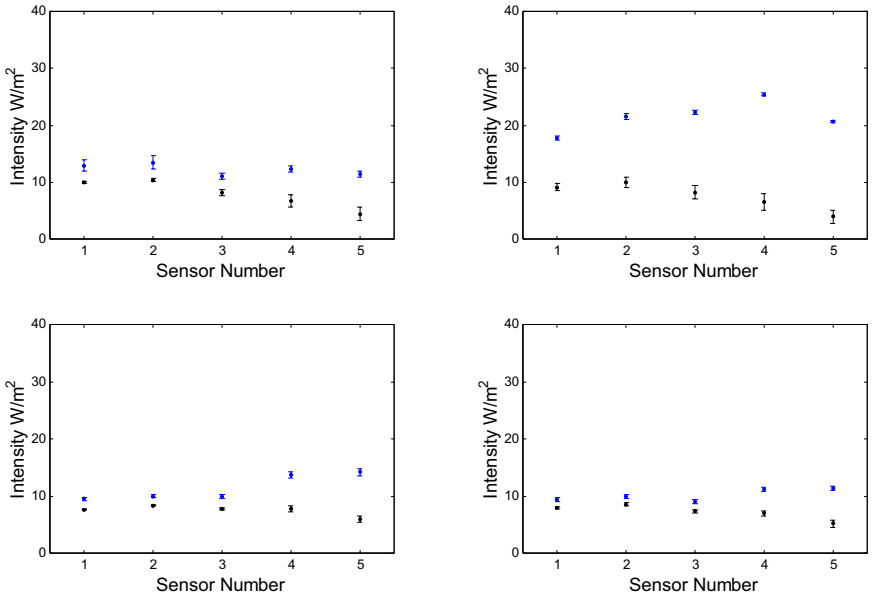

Figure 4.9:

Calibrated mean absolute irradiance values for test subject A, off and on-eye, facing the horizon for the four cardinal points ~ 20 minutes pre-local noon.

Progressing clockwise from top left: East, South, North & West.

Trends shown in figures 4.7 and 4.8 for the southern and eastern facing orientations are quite different to those presented in figure 4.9. Taking the southern facing aspect, the off-eye trend is flatter than the previous two figures. This was expected for local noon, as the sun was located almost due south, and illuminated the array evenly, if one negates the shell's own curvature. As measurements were recorded 20 minutes before noon, it can be seen that sensor 4 on the nasal side received a slightly higher irradiance than the others. This shows that the array can distinguish between minor deviations in solar angles, i.e. if measurements had been recorded at exactly local noon, sensor 3 would have yielded the highest output voltage, with the array output voltage falling off on

either side. Due to the fact that the measurement was recorded just 20 minutes pre-local noon, this meant that sensor 4 on the nasal side of the right eye array, the one which would have been most normal to the direct solar rays, recorded the highest irradiance, with the array output voltage falling off temporally, as expected. The irradiance recorded by sensor 5 was similar to that of 2 and 3, due to the curvature of the shell and its shallower angle with respect to the direct rays.

On-eye, however, for this southern facing aspect, the protection presented by the prominent brow ridge can once again be seen. The nasal sensors experience a much larger reduction in received direct irradiance at 20 minutes to local noon. It is suggested here that this reduction would be less evident if the measurements were recorded at exact local noon as the brow ridge and nose would have less impact on blocking the direct rays reaching this nasal region.

Due to the sun being located due south, all other measurement orientations presented in figure 4.9 demonstrate no significant attributes. For this reason, there is no real distinguishing factor in the off-eye trends for the east, west and north orientations. It can be seen that for the western orientation, the nasal sensors off-eye are higher than the temporal ones and this can be attributed to the direct rays originating from due south are illuminating these. The temporal sensors are shaded due to the right eye sensor's curvature. However, the on-eye data for the western facing aspect shows a marked decrease in surface irradiance at the nasal sensors, and this is due to the nose and brow blocking these direct rays. Both the eastern and northern facing aspects present a quite diffuse irradiance across the

array when off-eye, as would be expected with the sun in the south and no there were no highly reflective features in the foreground. These rather diffuse, flat trends are altered slightly with the array placed on-eye, with the nasal sensors experiencing a reduction in diffuse radiation falling upon them due to anatomical protection.

Approximately 40 minutes post-local noon, figure 4.10 presents test subject A gazing towards the horizon under direct insolation for solar azimuth and solar elevation angles proceeding from ~ 217º to ~234º and ~ 73º to ~ 68º respectively. As the sun had now reached its peak and was progressing towards evening and sunset, the off-eye trend for the southern facing aspect was surprisingly uniform. However, the on-eye data reveals yet again the protection afforded by the nasal brow ridge at reducing the apparently relatively uniform foreground. As expected, sensors 1 and 2 received the highest irradiance.

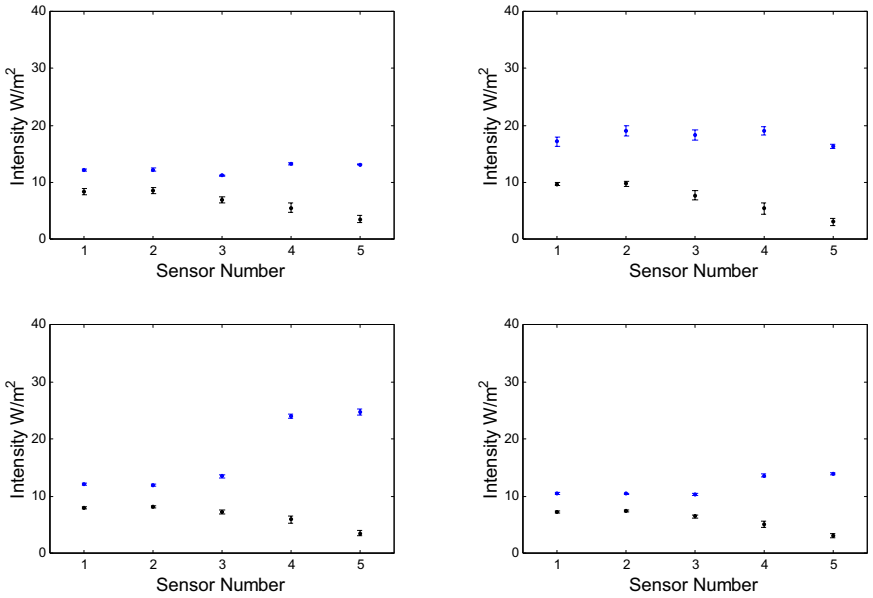

Figure 4.10:

Calibrated mean absolute irradiance values for test subject A, off and on-eye, facing the horizon for the four cardinal points ~40 minutes post-local noon.

Progressing clockwise from top left: East, South, North & West.

For both the eastern and northern facing data, once again the foregrounds appear relatively diffuse off-eye, with the brow decreasing the irradiance nasally on-eye. The most remarkable feature is that of the western facing data. There is a substantial difference in the on- and off-eye trends. The more nasal sensors, namely 4 and 5, receive the lowest direct UVR irradiance prior to the face being moved away from the array. Once moved back, the protection afforded by the facial anatomy is clear to see. With the sun at a south-westerly location, one would expect that sensors 4 and 5 were irradiated the greatest when facing west when the head is not present. As can be seen, with the head present, sensors 4 and

5 experience a huge decrease in surface irradiance, further emphasising the significance of facial shading at the anterior ocular surface.

The relative intensities for each sensor across the array will now be given in section 4.3.3 for test subject A under direct insolation. These correspond to figures 4.7 to 4.10. By calculating the relative intensities, the background, or reference UV radiation field is eliminated and the actual relative intensity of terrestrial solar UVR across the ocular surface is presented.

4.3.3 Test Subject A Relative Intensities - Direct Insolation

The relative intensities for test subject A facing the horizon under direct insolation for the four cardinal points are presented in figure 4.11. These relative intensities were calculated from the calibrated mean irradiance values presented in figure 4.7.

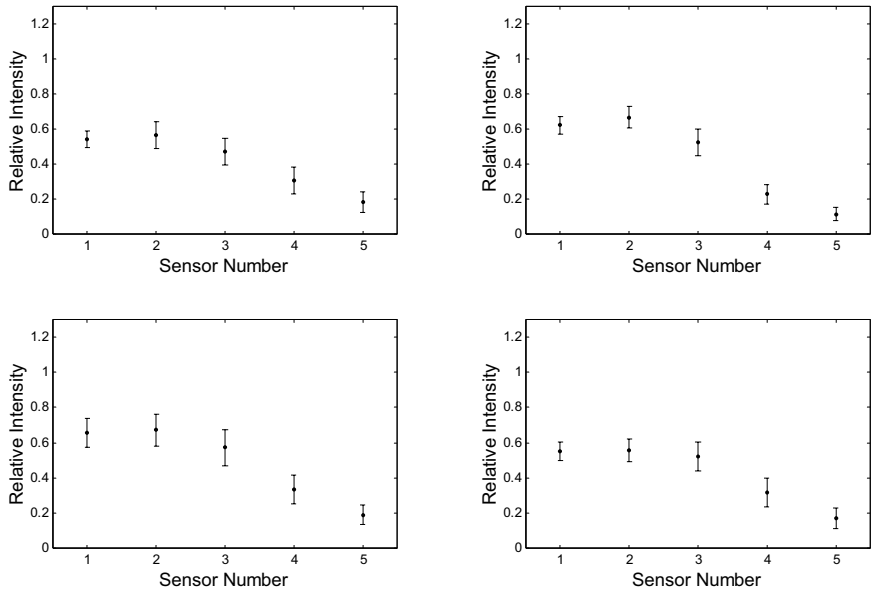

Figure 4.11:

Relative intensities for test subject A facing the horizon for the four cardinal points 2.5 hours pre-local noon.

Progressing clockwise from top left: East, South, North & West.

As shown in figures 4.11 to 4.14, there is a consistent relative intensity trend for test subject A under direct insolation. By broadly analysing each of these figures for all cardinal point orientations, it can be seen that the more temporal sensors receive a higher relative intensity than the more nasal ones. In each figure, irrespective of orientation, sensors 1 and 2 are substantially greater than sensors 4 and 5. This can best be explained by test subject A having a very prominent brow ridge/nasal structure. For the same measurement window, the relative intensities for test subject B will be presented and compared to those presented here for test subject A in section 4.3.6. Having a less pronounced brow ridge, test subject B showed consistently flatter relative intensities for the most

part, further emphasising the protective role at the nasal portion of the nasal brow ridge.

Figure 4.12 presents the relative intensities calculated from the data presented in figure 4.8. For all orientations, temporal sensors 1 and 2 were higher than the nasal sensors 4 and 5, due to the facial anatomy dominating the spread of UVR across the ocular surface, through shading of the nasal sensors.

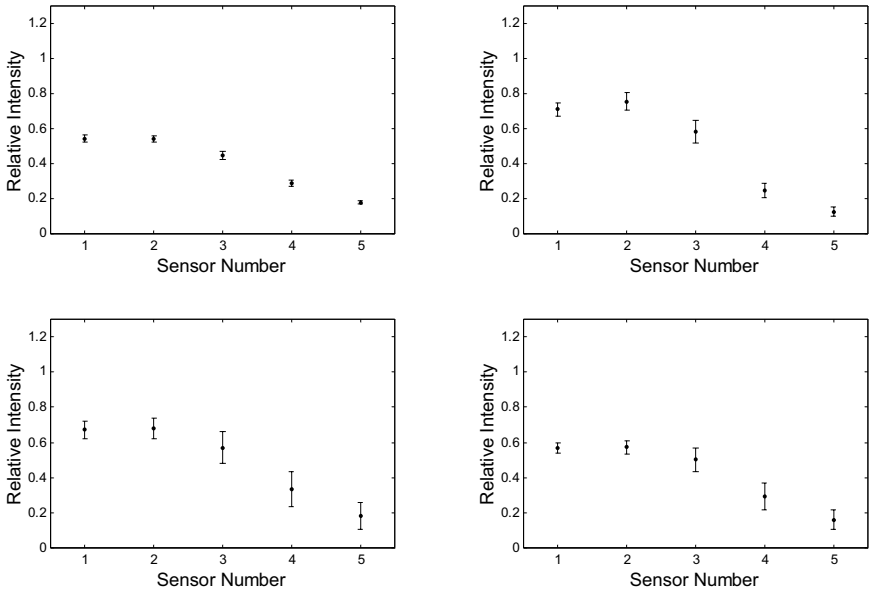

Figure 4.12:

Relative intensities for test subject A facing the horizon for the four cardinal points 2 hours pre-local noon.

Progressing clockwise from top left: East, South, North & West.

Figure 4.13 presents the relative intensities calculated from the data presented in figure 4.9. Once again, there is a consistent temporal bias across the

array. Slightly higher relative intensities for the east, west and north oriented data than figures 4.11 and 4.12 are the product of the off-eye and on-eye data presented in figure 4.9 being comparable in intensity. Taking the south facing data presented in figure 4.9, there is a significant difference in the on and off-eye irradiance intensities. As this data was recorded at 20 minutes pre-local noon, the sun was approaching its zenith and also approaching due south in the sky. This is evident in figure 4.9 as the off-eye irradiance intensities are much higher for the south facing data than the other three orientations. Due to facial shading of a near uniform south facing UV radiation field across the array, there was a significant difference in on and off-eye intensities when compared to the other three orientations. As the relative intensities are calculated by dividing the off-eye data into the on-eye data, thereby essentially eliminating the background radiation field, the southern facing relative intensities across the array presented in figure 4.13 are actually lower than those of the east, west and north relative intensities. This is again indicative of test subject A having a deep set ocular surface. The fact that the sun was almost at its diurnal peak, the prominent brow ridge provided excellent protection across the eye, with the nasal aspect receiving the greatest protection.

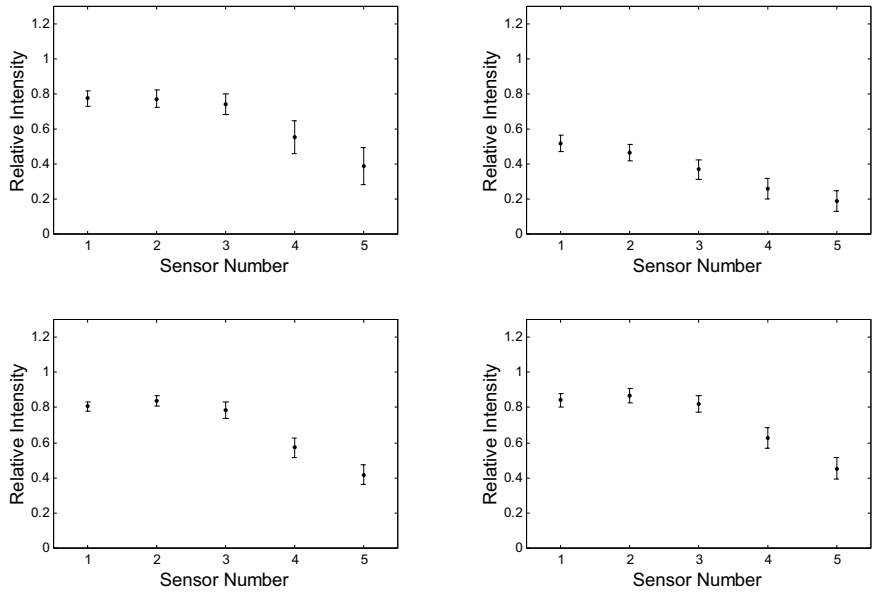

Figure 4.13:

Relative intensities for test subject A facing the horizon for the four cardinal points ~ 20 minutes pre-local noon.

Progressing clockwise from top left: East, South, North & West.

Figure 4.14 presents the relative intensities calculated from the data presented in figure 4.10. Once again, there is a consistent temporal bias across the array. As this data was recorded at approximately 40 minutes post local noon, one would not expect any major departures from the relative intensity trends presented in figure 4.14. Taking figures, 4.9 and 4.10, the south, east and north facing data for on and off-eye are quite similar as would be expected. This is reflected in their corresponding relative intensities, figures 4.13 and 4.14 respectively. However, examining the west facing data in figure 4.10, as the sun was located west of due south, the nasal sensors were irradiated the greatest off-eye, by comparison with the other orientations and west facing off-eye data presented in figure 4.9. The on-

eye irradiance values in figure 4.10 portray a marked reduction in the irradiance levels received at the nasal sensors due to nasal and brow ridge shading, with the temporal sensors receiving a slightly greater irradiance. Taking the corresponding west facing relative intensities computed for figure 4.14, due to the substantial reduction in on-eye irradiance, there is a more pronounced drop across the sensor array from temporal to nasal, as compared to the west facing relative intensity data presented in figure 4.13.

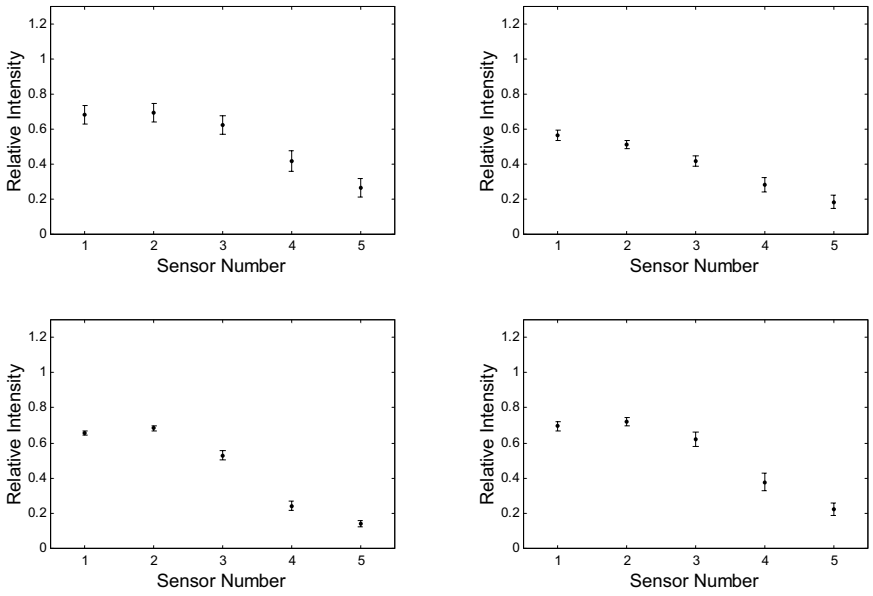

Figure 4.14:

Relative intensities for test subject A facing the horizon for the four cardinal points ~ 40 minutes post-local noon.

Progressing clockwise from top left: East, South, North & West.

Having examined the data recorded with test subject A looking towards the horizon for the four cardinal points under direct insolation, sections 4.3.4 and 4.3.5 will now provide the calibrated mean irradiance levels and corresponding

relative intensities for test subject A under diffuse sky conditions at similar times of the day.

4.3.4 Test Subject A Irradiance Intensities - Diffuse Insolation

Starting at approximately 2 hours pre local noon, figures 4.15 to 4.18 show test subject A looking towards the horizon until approximately 1.5 hours post local noon under diffuse insolation. As these figures are presented over time, the progression of the sun with respect to the four cardinal point measurements orientations is analysed.

Figure 4.15 presents test subject A gazing towards the horizon under diffuse insolation at approximately 2 hours pre-local noon. At this time the SA and SEA proceeded from ~ 129º to ~134º and ~ 55º to ~ 58º respectively. Plotted on the same scale as the figures presented for direct insolation, it is clear that the irradiance levels on and off the ocular surface for all directions are markedly less under diffuse insolation.

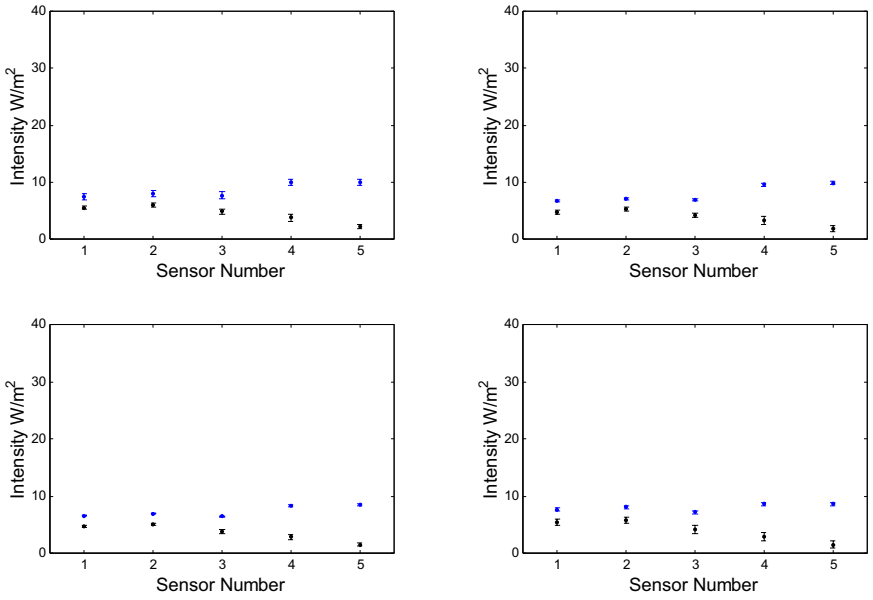

Figure 4.15:

Test subject A gazing towards the horizon under diffuse insolation at ~ 2 hours pre-local noon.

Progressing clockwise from top left: East, South, North & West.

Due to the nature of diffuse skies having little or no direct component, as would be expected, the four orientations shown in figure 4.15 represent a much flatter UVR field both on and off the eye than those figures presented for direct insolation. There are no striking features indicating the position of the sun in the sky with respect to the 5 photodiodes on the sensor array. Indeed, each of the orientations, on and off-eye, bear a similar resemblance to each other, indicative of uniform cloud cover.

Figure 4.16 presents test subject A gazing towards the horizon under diffuse insolation at approximately 1 hour pre-local noon. At this time the SA and SEA proceeded from ~ 130º to ~152º and ~ 55º to ~ 58º respectively.

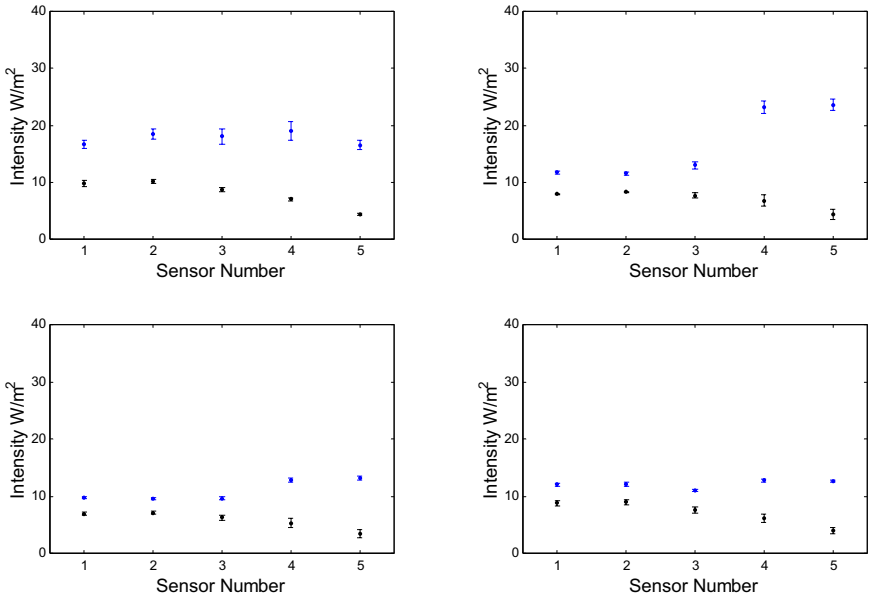

Figure 4.16:

Test subject A gazing towards the horizon under diffuse insolation at ~ 1 hour pre-local noon.

Progressing clockwise from top left: East, South, North & West.

The most remarkable feature about figure 4.16 is that the levels both on and off-eye are comparable to the figures shown earlier for direct insolation. There is direct penetration of the suns rays through the perceivably uniform cloud cover from the eastern direction. This is particularly evident on the nasal sensors off-eye for the south facing subplot. Under clear sky conditions, the nasal sensors would be expected to receive greater irradiance off-eye than the temporal ones as the sun was still progressing towards zenith and located east of due south. The

fact that they still receive a similar irradiance under cloud cover only serves to highlight that a serious UVR hazard still exists under light cloud cover. As the data recorded for figure 4.16 was approaching local noon, one would expect higher levels than those presented in figure 4.15 due to the increase in diffuse insolation. For all orientations, the nasal sensors received less irradiance while on-eye due to shading.

Figure 4.17 presents test subject A gazing towards the horizon under diffuse insolation at approximately 20 minutes to local noon. At this time the SA and SEA proceeded from ~ 151º to ~182º and ~ 76º to ~ 78º respectively.

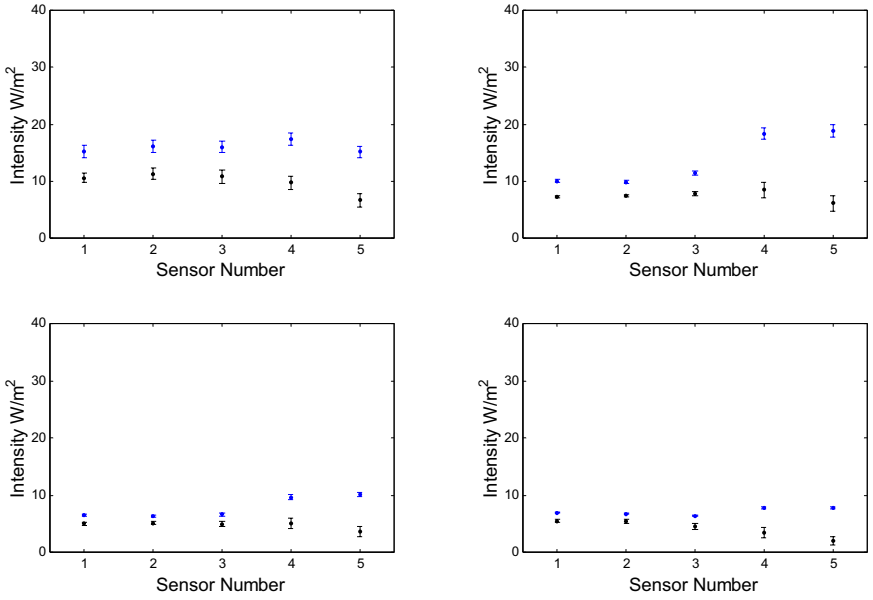

Figure 4.17:

Test subject A gazing towards the horizon under diffuse insolation at ~ 20 minutes pre-local noon.

Progressing clockwise from top left: East, South, North & West.

Similar to figure 4.16, for the south facing aspect there was direct penetration through the cloud cover from the sun located just east of due south resulting in sensors 4 and 5 receiving greater irradiance than the more temporal sensors while the array was held off-eye. This was most probably due to the cloud cover directly beneath the sun becoming slightly thinner during the time course of south facing measurement. This is also true of the west facing off-eye data, with the north facing off-eye data relatively flat as expected due to no direct solar component influencing off-eye data. However, the nasal ridge reduced the diffuse component for this orientation resulting in the temporal irradiance being higher than the nasal on-eye. The east facing off-eye data is relatively uniform, indicating stable cloud cover at that time, with the on-eye data dropping slightly at the nasal sensors due to shading.

Figure 4.18 presents test subject A gazing towards the horizon under diffuse insolation at approximately 1.5 hours after local noon. At this time the SA and SEA proceeded from ~ 237º to ~247º and ~ 69º to ~ 63º respectively.

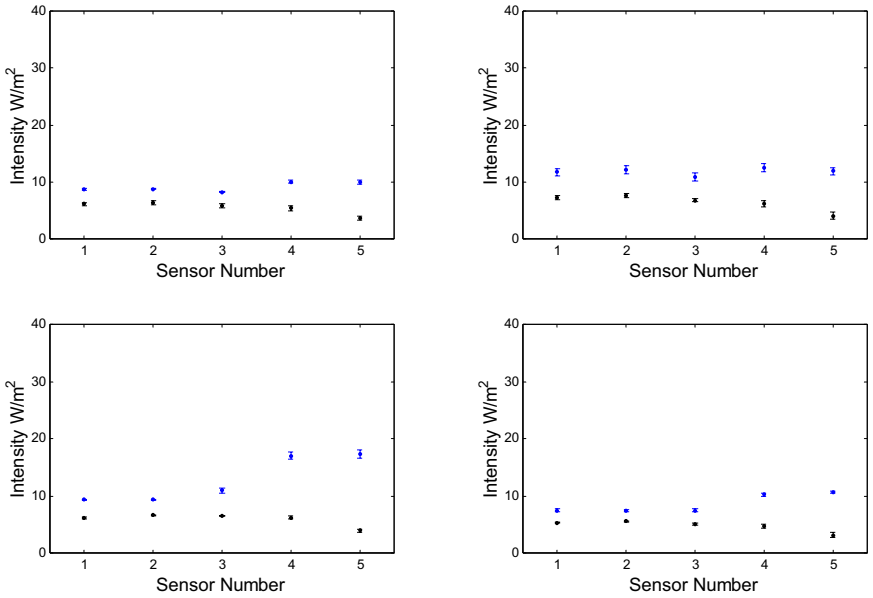

Figure 4.18:

Test subject A gazing towards the horizon under diffuse insolation at ~ 1.5 hours post-local noon.

Progressing clockwise from top left: East, South, North & West.

It is clear from figure 4.18 that the irradiance levels on and off-eye for the east and south facing data at the eye were taken under uniform cloud cover. There is no notable bias across the array for on and off-eye data, which is indicative of no cloud penetration of the direct beam. However, as the sun was located south-westerly, sensors 4 and 5 were irradiated off-eye more so than 1, 2 and 3. This is due to the illumination through the cloud cover being brightest for this solar coordinate and sensors 4 and 5 being oriented most normal to this south-westerly solar position. On-eye shading resulted in sensor 5 receiving least irradiance for this orientation. East, south and north orientations were relatively flat both on and off-eye with no distinct features, evident of a uniform radiation field.

The relative intensities for test subject A looking towards the horizon under diffuse insolation will now be presented in section 4.3.5.

4.3.5 Test Subject A Relative Intensities - Diffuse Insolation

Corresponding to figure 4.15, figure 4.19 shows the relative intensities computed for test subject A under diffuse insolation ~ 2 hours before local noon.

As this data was recorded with the sun relatively low in the east under diffuse insolation, there were no significant differences in the irradiance data provided in fig 4.15, and as a result of this, the relative intensities for each cardinal point orientation are very similar, indicative again of uniform cloud cover, with no penetrating direct component. As can be seen in figure 4.19, test subject A's nasal and brow ridge offered excellent protection at the nasal portion for all cardinal point orientations.

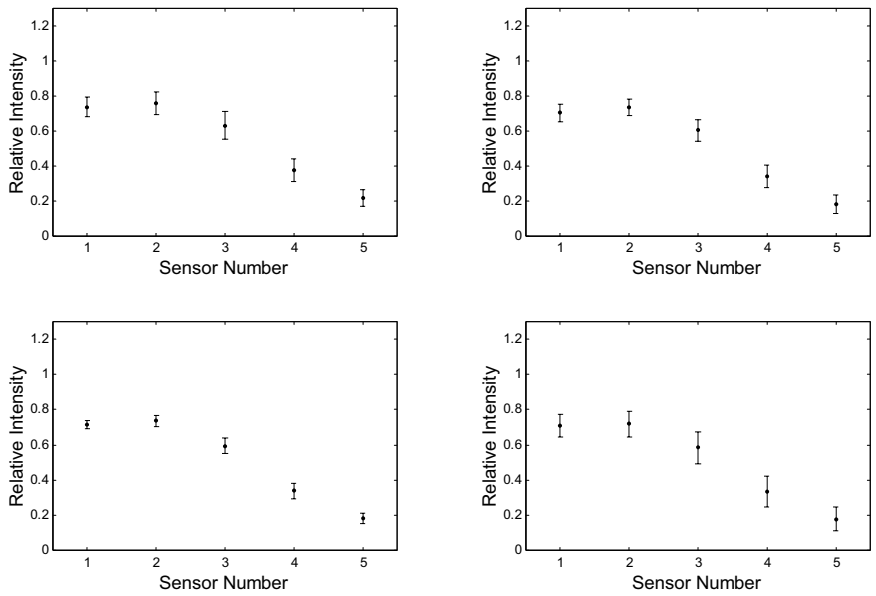

Figure 4.19:

Relative intensities computed for test subject A under diffuse insolation ~ 2 hours pre-local noon.

Progressing clockwise from top left: East, South, North & West.

Figure 4.20 corresponds to the data recorded approximately 1 hour before local noon presented in figure 4.16. All 4 cardinal point orientations show a temporal to nasal bias. As suggested in the discussion of figure 4.16, there was direct penetration of the solar beam from the east direction in the south facing subplot, resulting in sensors 4 and 5 receiving greater irradiance than the temporal sensors when off-eye. The relative intensities across the array shown for the south facing data in figure 4.20 stress the importance of brow ridge shading again as the temporal sensors far exceed the nasal sensors, which were shaded from the cloud penetrating direct component when on-eye, leaving the temporal sensors exposed

to the diffuse component. All other cardinal point orientations show a temporal-nasal bias, reflective of the facial structure shading the nasal portion under diffuse insolation.

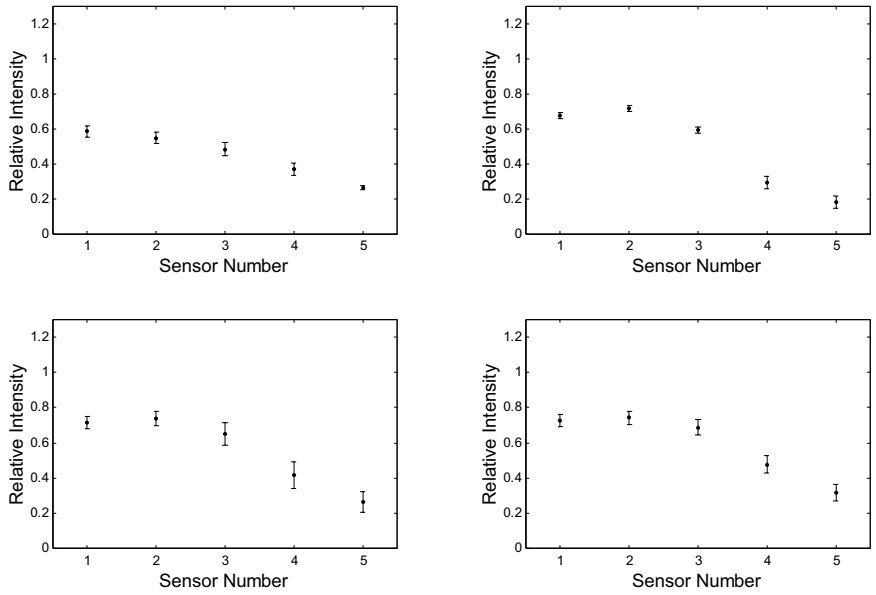

Figure 4.20:

Relative intensities computed for test subject A under diffuse insolation ~ 1 hour pre-local noon.

Progressing clockwise from top left: East, South, North & West.

Figure 4.21 presents the relative intensities across the array of test subject A gazing towards the horizon under diffuse insolation at approximately 20 minutes to local noon, and corresponds to figure 4.17. It can be seen that similar to the previous relative intensities, nasal shading dominates the trends for all four orientations, resulting in a temporal-nasal bias.

Figure 4.22 corresponds to figure 4.18 recorded ~ 1.5 post local noon and as before, nasal shading dominates again, reiterating that the brow ridge plays a fundamental role in protection of the nasal portion under diffuse insolation.

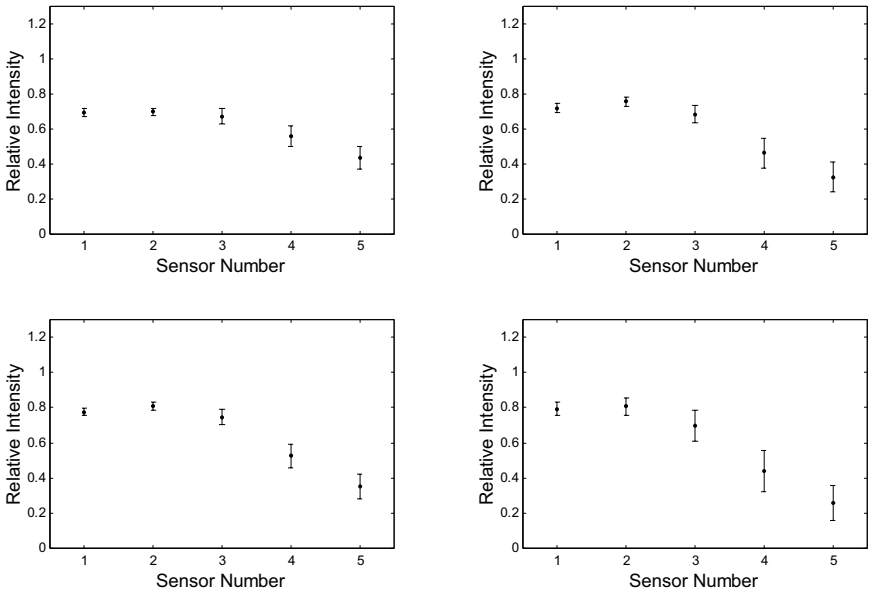

Figure 4.21:

Relative intensities computed for test subject A under diffuse insolation at ~ 20 minutes pre-local noon.

Progressing clockwise from top left: East, South, North & West.

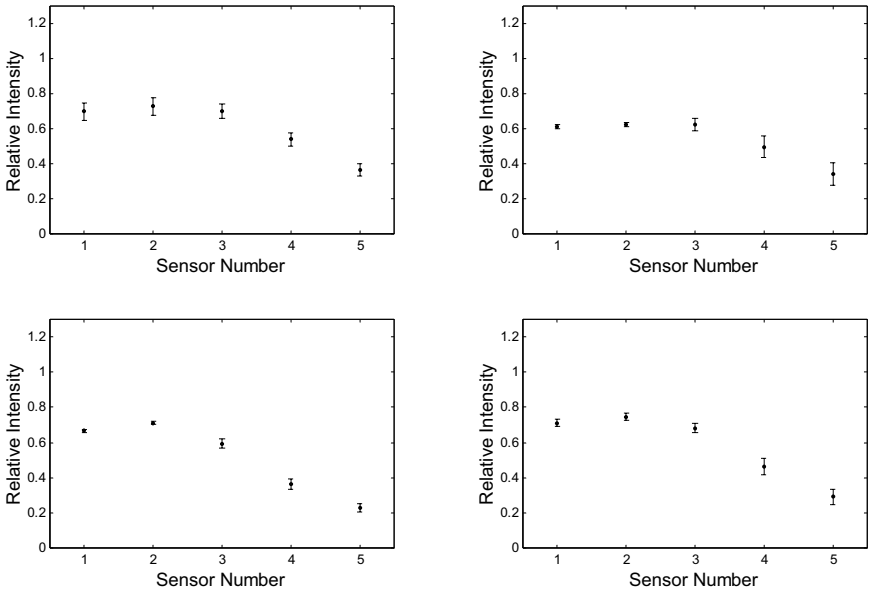

Figure 4.22:

Relative intensities computed for test subject A under diffuse insolation ~ 1.5 hours post-local noon.

Progressing clockwise from top left: East, South, North & West.

4.3.6 Relative Intensity Comparisons of Test Subject A and subject B

To compare and show the effects of different facial structures on biases across the ocular surface, the relative intensities of test subject B will now be superimposed on figures presented already for test subject A. Two figures are given for the relative intensities of both test subjects under direct insolation, and two figures under diffuse insolation.

As test subject B had a less prominent brow ridge than test subject A, one would expect less shading across the array for test subject A and therefore a flatter relative intensity across the array.

To discriminate between facial structures, the most effective method of analysis is the comparison of relative intensities. As it is the effect of facial shading being examined, and the resultant elucidation of ocular bias under various environmental conditions, it is only necessary to present the relative intensities for test subject B, as the background, or off-eye UV radiation field, was the same for test subjects A and B for a particular measurement duration. For this reason, the only major variable was the test subject in question. Through comparison of the relative intensities of test subjects A and B, one can see the effect of different facial structures on spread of UVR across the ocular surface most effectively. In all figures, test subject A is in red, and test subject B is in black. For the four following, the calibrated mean irradiance data and relative intensities have already been analysed, and as such it is only the comparison of different facial features which are of interest. The efficacy of the array in discriminating between different facial anatomies is evident through the large differences in relative intensity.

Measured under direct insolation, the data presented for test subject A in figures 4.23 and 4.24 has previously been shown in figures 4.12 and 4.14 respectively. In figures 4.23 and 4.24, the overall difference in relative intensities reaching the ocular surface of both test subjects is illustrated. Indeed, for some orientations, the more central sensors on the array approach a relative intensity of 1 for test subject B, indicating that no protection was afforded by the overhang of his brow ridge. This further emphasises the degree of overall and, in particular, nasal protection afforded by test subject A's facial anatomy. For the most part, test subject B showed a flatter trend progressing from temporal to nasal.

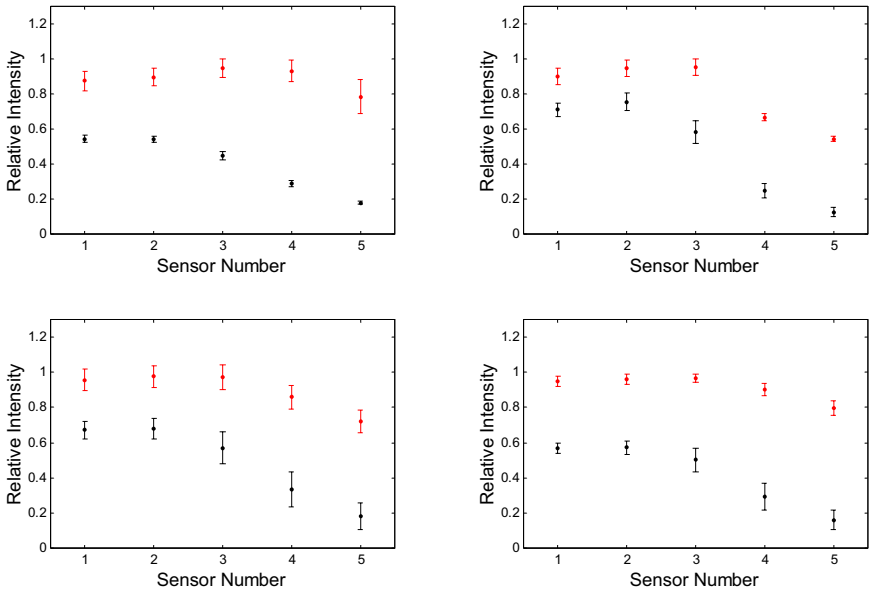

Figure 4.23:

Relative Intensities of test subject A (black) and B (red) under direct insolation.

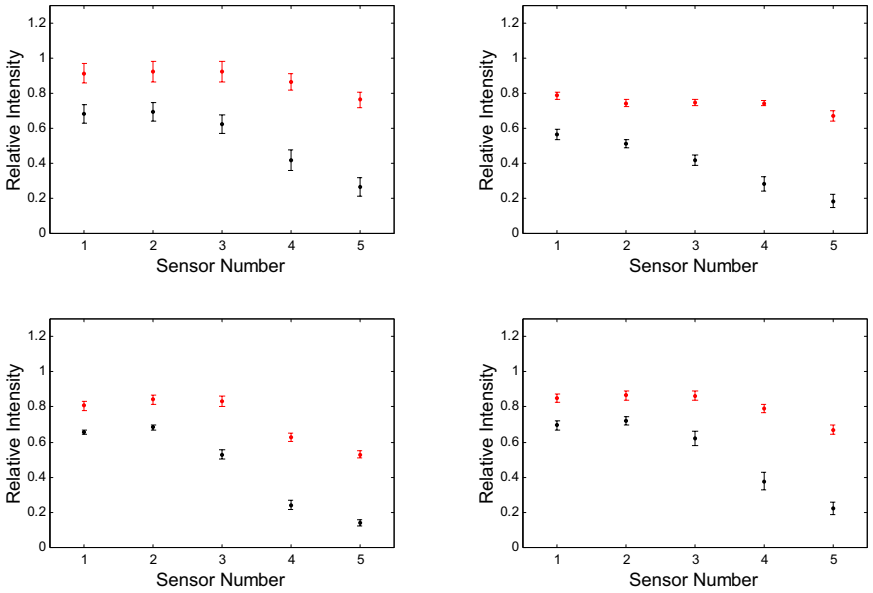

Figure 4.24:

Relative Intensities of A and B under direct insolation.

Measured under diffuse insolation, the data presented for test subject A in figures 4.25 and 4.26 has previously been shown in figures 4.20 and 4.22 respectively. It is clear from figures 4.25 and 4.26 that test subject B receives a greater irradiance than test subject A across the entire lid margin, and although not as significant, nasal protection is still offered by test subjects B's anatomy under diffuse skylight.

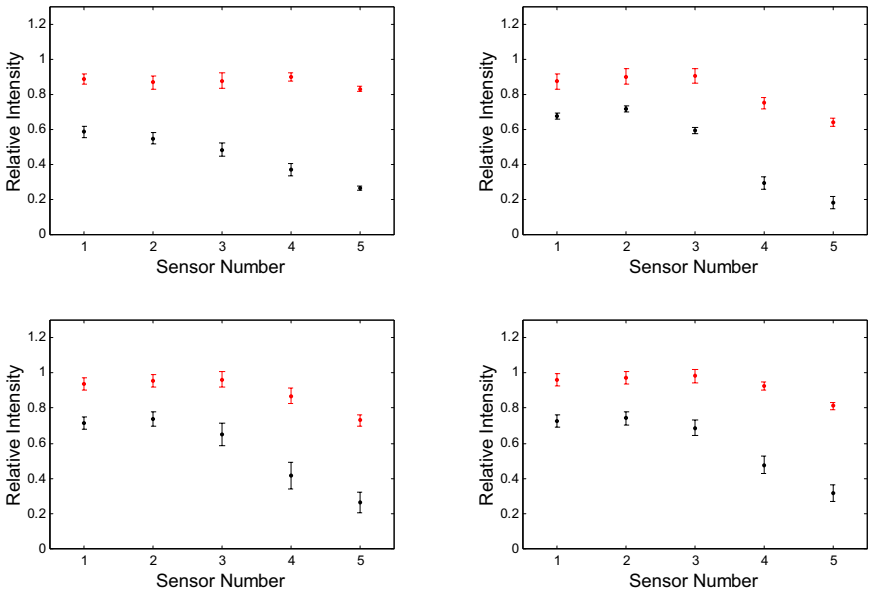

Figure 4.25:

Relative Intensities of A and B under diffuse insolation

Progressing clockwise from top left: East, South, North & West.

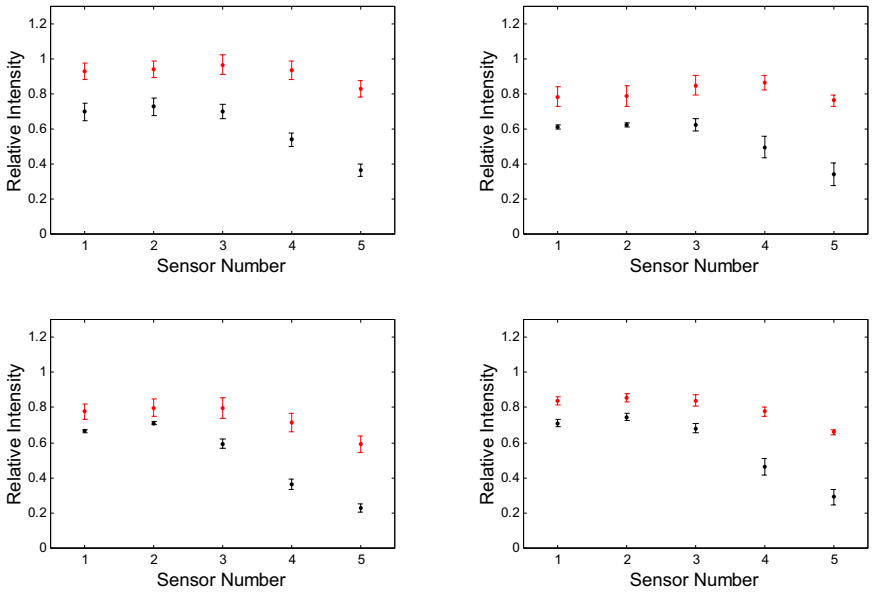

Figure 4.26:

Relative Intensities of A and B under diffuse insolation.

Progressing clockwise from top left: East, South, North & West.

4.3.7 Conclusion

In conclusion, a novel solar blind UVR sensor array has been designed constructed and tested in the field to measure the background and actual on-eye raw voltage levels for the four cardinal points under direct and diffuse insolation. By calculating a calibration factor between raw voltage produced by the photodiodes and solar UVR irradiances measured by a calibrated broadband UVR radiometer, the absolute intensities in W m^{-2} have been computed at the ocular surface under these different insolations. A survey of ocular irradiance has also been shown progressing from pre- to post-local noon, highlighting the substantial differences in irradiance occurring across the lid margin for the four cardinal

points, and the degree of protection offered by the facial anatomy. The relative intensities for the aforementioned field measurements has also been presented, indicating that in general a temporal-nasal bias exists while standing in an upright position with a typical natural head gaze towards the horizon. Intercomparison of test subjects has also been shown, and the most notable feature of this intercomparison is the major differences in UVR levels received across the entire lid margin, revealing that the levels of UVR at the eye is very individualistic. It has been shown that for most orientations and solar angles, the facial anatomy affords the nasal portion greater protection than the temporal portion. This is true for both direct and diffuse insolation environments. As had been previously suggested in section 1.2.4.2, it would appear that for the most part, reflections of diffuse UVR from the nasal structure towards the nasal portion are superseded by the degree of protection afforded by the brow ridge, and paradoxically, by the nasal structure also under direct and diffuse skies.

For this reason, and since many ocular pathologies occur nasally, the phenomenon of peripheral light focussing has been investigated and will be presented in the following chapter. As has been suggested by Coroneo, intensification of refracted terrestrial solar UVR at the nasal limbus due to UVR striking the temporal corneal dome obliquely, could play the major role in the aetiology of pathologies such as pterygium, since it would appear that the nasal portion is relatively well protected from both direct and diffuse sunlight when compared to the temporal portion, which consistently showed higher relative intensities in the research presented here.

Chapter 5

Novel Peripheral Light Focusing Measurement System and Results

5.1 Introduction

Peripheral Light Focusing has been credited as a possible key agent in affecting nasal pterygia, a hypothesis first outlined by Coroneo. In an insolation environment, PLF at the nasal region is primarily dependent on grazing incident angle, which in itself is a function of SZA, the albedo of the surrounding terrain, the dioptric power, or convexity of the temporal peripheral cornea, ocular prominence and lateral protection provided by hair or sunglasses and/or other shading headwear. Depending on the incident angle, the relative amount of UVR reflected from the corneal surface will vary, thus increasing or reducing the available amount of UVR for refraction at this surface.

As it has also been termed by Sliney, PLF, or the 'Coroneo Effect', most possibly accounts for the occurrence of more nasal pterygia than temporal and could play a role in UVR cataractogenesis[454]. This can be best described by the fact that the nose obstructs light striking the nasal cornea at angles which contribute to instigating the nasal to temporal refraction phenomenon. Only in rare circumstances may rays be refracted across the corneal dome from nasal origin. Considering the right eye, an example of nasally originating PLF would occur if one was to strain the eyes towards the extreme right side. Assuming a low horizon

sun originating from the subjects left hand side, and a relatively protruding eye, radiation could strike the nasal corneal dome and be refracted towards the temporal limbus.

Conversely, with the temporal cornea of either eye exposed, oblique rays incident can readily be refracted to the nasal limbus, provided there is a quite large SZA, and the ocular tissue is situated in a position conducive to the refraction process. Such conditions occur when the sun is low in the horizon sky and the temporal portion is oriented such that rays may be incident here obliquely. Equally, if one is lying down on their side and the temporal portion is exposed to UVR from the sun at its zenith, PLF will occur. These are straightforward examples of instances where PLF may occur. Of course, PLF can occur at any time outdoors, once the sun is located within a catchment range behind the temporal cornea.

In the research presented here, the phenomenon of PLF was modelled using ray tracing software in tandem with a laboratory based setup utilising an anatomically based model eye. Through development of this novel laboratory based PLF measurement system, the transmission of the human cornea was measured *in vivo* across the UVR waveband.

5.2 RubrEye – Anatomical Model Eye

In order to investigate PLF *in vitro*, a number of anatomically based polymer eyes (polydimethylsiloxane) were manufactured at the Texas Eye and Research Technology Center, located in the College of Optometry University of

Houston, Tx. These 'RubrEye's' are available with different optical powers and used by TERTC as model eyes to demonstrate emmetropia, hyperopia and myopia. As the whole RubrEye is made of the same material and thus has a constant refractive index of 1.406, the focussing power of its cornea is slightly different to that of the human cornea. The human cornea provides 70 % of the eye's total focussing power and has a refractive index of 1.376. However, as a model cornea for investigations into PLF *in situ*, the RubrEye served adequately to aid in the construction of the fibre optic sensing system used later to measure the corneal transmittance *in vivo*. By measuring the transmission of a bisected RubrEye with the conventional method of directing a beam straight through the horizontal thickness of the sample, and collecting the transmitted radiation with a butt coupled fibre optic, the transmission of the material was found. Assisted by ray tracing techniques, and based on the phenomenon of Peripheral Light Focusing, a new method was developed to measure the RubrEye's transmission and was later adapted and advanced to measure the human corneal transmission *in vivo*.

The two part miscible silicone-based elastomer compound which was used to produce the RubrEye was supplied by General Electric and is better known as RTV-615 a+b. As a two-part addition cure, the silicone compound resin and curing agent were mixed by parts in a 10:1 ratio respectively. Due to their individual viscosities, after adding the curing agent, both were mixed for approximately five minutes. By doing this, many air bubbles were introduced to the mixture, so it was necessary to degas. This was achieved by pouring the

mixture into a beaker, more than twenty times the volume of the initial mixture, and placing it inside a BOC Edwards Auto 306 coating system. By gradually pumping the vacuum chamber down to ~ 10^{-5} mbar (typical pressure at earth mean sea level is 1013.25 mbar, or 1 atm), the volume of the initial mix expanded due to outgassing of absorbed atmospheric gases. This pressure was confirmed through correspondence with TERTC, and was held for 5 minutes, after which the viscous mixture was deemed to be completely outgassed, and the vacuum was suspended. The mix was then carefully poured into the RubrEye mould, so as to avoid reintroducing air. If necessary, any visible air bubbles introduced into the mixture at this point were enticed to the surface using a dissecting needle and the mixture was then sealed and left to set for 24 hours at room temperature.

When finally cured, the globe was optically clear with a quoted refractive index of 1.406. As with most nominal refractive indices, this value is for wavelengths in the yellow region of the visible spectrum.

The RubrEye eye model consisted of a corneal segment also. Due to the manufacture process, which took place by pouring the viscous mixture into an aluminium mould, the transition from the globe to cornea, where the limbus physiologically occurs, was slightly stepped, but by finely paring this transition zone with a scalpel, a smooth continuous surface from globe to cornea was attainable.

5.3 AutoRAY Modelling of RubrEye PLF and Angular Dependence on Input Optics

Using the AutoCAD (rel.13) environment, AutoRAY (ver.5) optical ray tracing software developed by RayCAD (MA, USA) was used to model PLF of the RubrEye. To ensure input model parameters were behaving correctly, the parameters outlined in the Gullstrand Exact Schematic Model of the emmetropic human eye were used to trace the optical path of normally incident light on the retina[455] [456]. As can be seen in figure 5.1, these parameters focused a collimated beam of light to the retina, as one would expect.

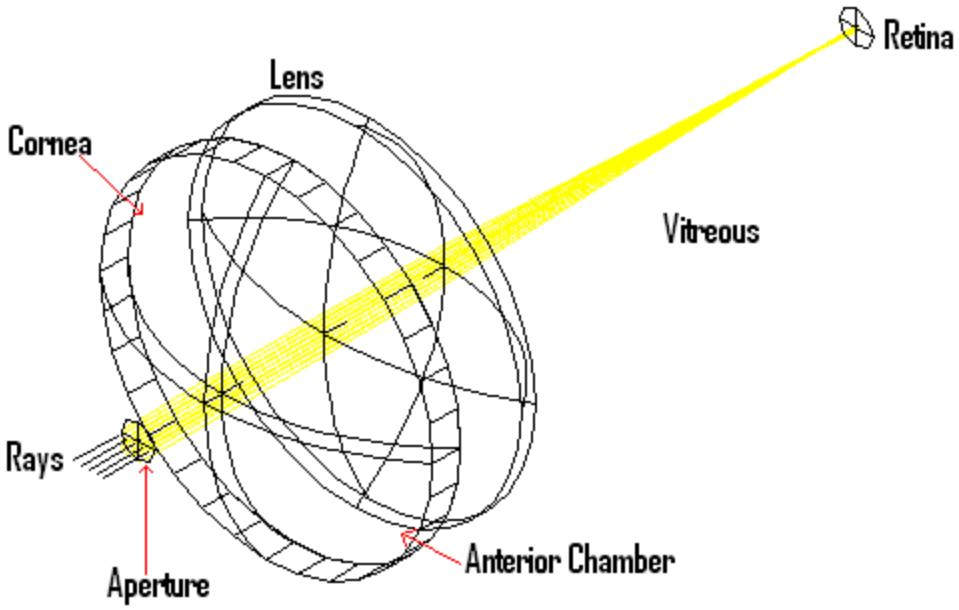

Figure 5.1:

Gullstrand's Exact Schematic Model of the human eye illustrating the emmetropic focusing power.

The homogenous RubrEye simulates the focusing power of the emmetropic human eye so that when parallel light strikes the cornea, it is refracted to a focal point at the retina, as can be seen in figure 5.2. Unlike the human eye, which has a number of refractive indices, there is only one change of refractive index from air to polydimethylsiloxane in the RubrEye. Along with this and the corneal radius of curvature, the RubrEye's refractive power is acceptably emmetropic.

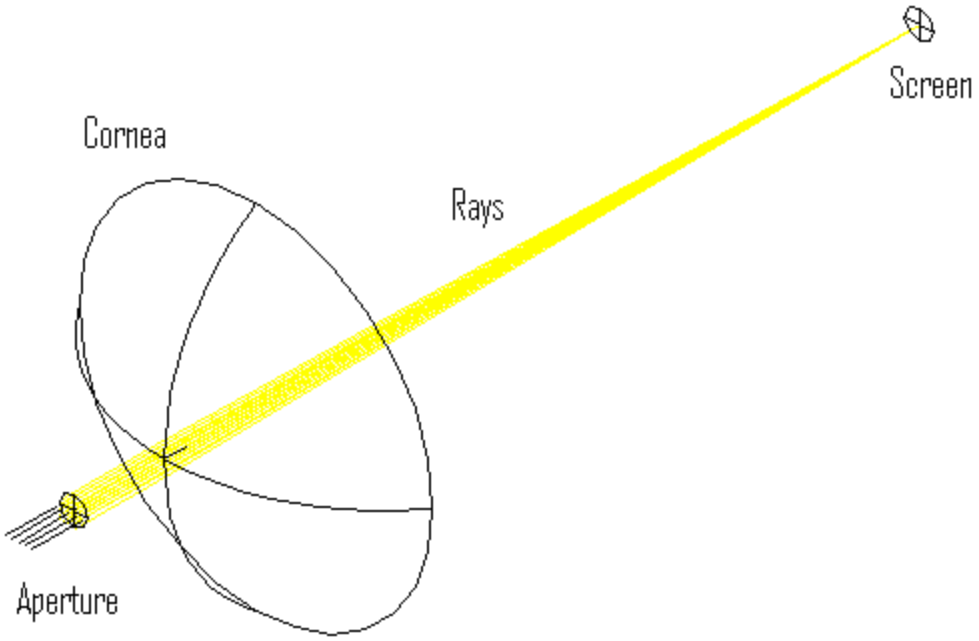

Figure 5.2:

Corneal focusing of collimated rays at RubrEye retina

The dimensions of the RubrEye are as follows:

Corneal diameter:	12.5 mm
Radius of Curvature:	7.65 mm
Mechanical Axial Length:	26.67 mm

PLF effects of rays striking the temporal cornea of the RubrEye were investigated in AutoRAY using the dimensions above as a function of the angle of temporal incidence for a known wavelength. AutoRAY only permitted one wavelength to be simulated at a time and so the 633 nm emission line of a Helium-Neon laser was chosen in AutoRAY to illustrate the effects of incident angle on the resulting focal point. The reason the 633 nm emission line was chosen was that a small portable He-Ne laser was available and could be easily incorporated into the laboratory based setup for comparison of the AutoRAY model and the actual lab setup based on the RubrEye. Photographic stills were captured also for the 633 nm line to visually compare PLF effects. It should be noted that for a particular incident angle at a point on the RubrEye's corneal dome, different wavelength lasers will have different focal points. However, the incorporation of the He-Ne laser in the model and lab setup were purely for preliminary investigations to give the researcher a more fundamental understanding of PLF and to aid in subsequent setups.

Figure 5.3 illustrates refraction of the He-Ne line by the RubrEye's temporal cornea at what was found to be the optimum angle of 20 º posterior to the coronal plane to maximise focusing at the nasal aspect in AutoRAY.

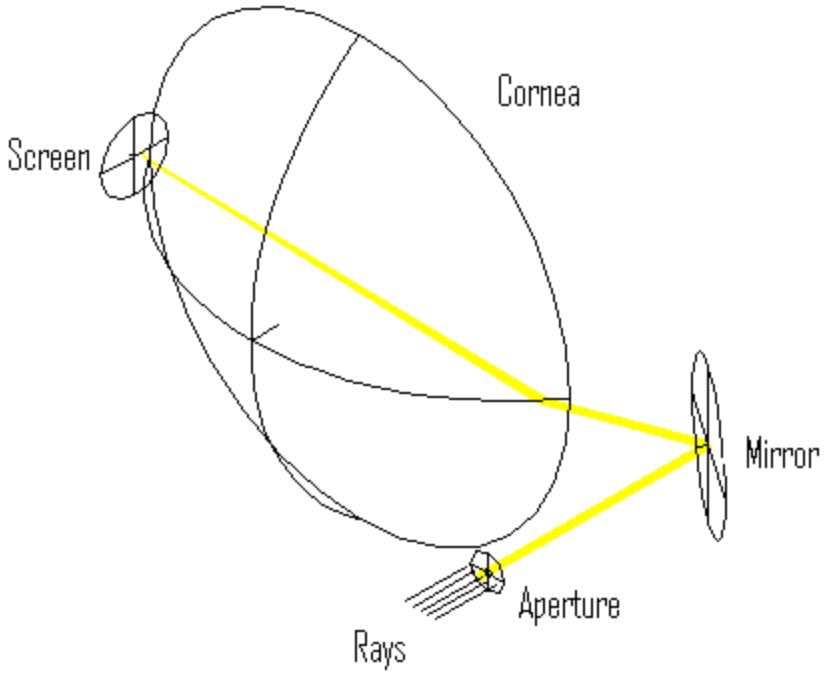

Figure 5.3:

Refraction of 633 nm laser line at temporal cornea

Figure 5.4 depicts the cross section of the same ray trace provided in figure 5.3 and illustrates strong focusing of the beam across the cornea. The trace comes to a focus along its path just before the nasal limbus. This can possibly be attributed to the refractive index of the RubrEye being slightly different to that of the cornea. At smaller and larger angles than 20 º posterior to the coronal plane, the resulting traces traversed towards the lens and emerged above the nasal limbus respectively. This is outlined in more detail now with corresponding photographic stills.

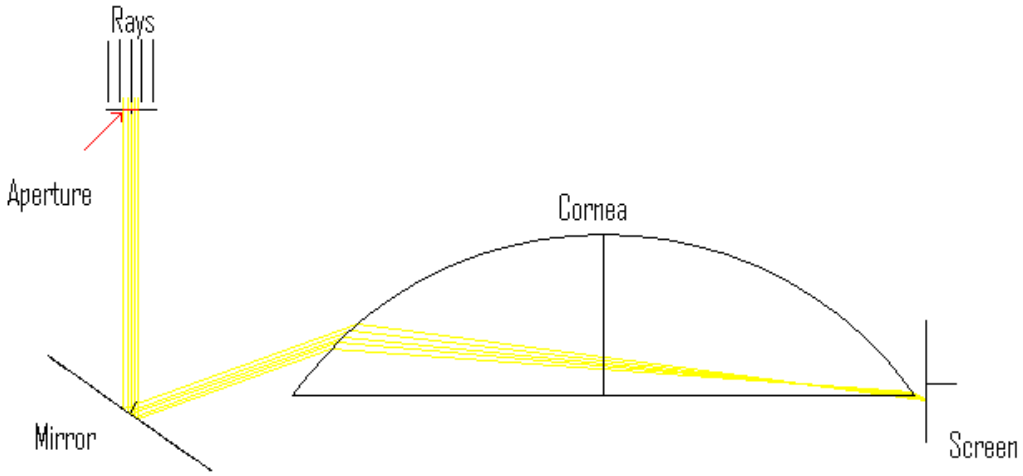

Figure 5.4:

Beam exhibiting temporal focusing at 20 º posterior to coronal plane

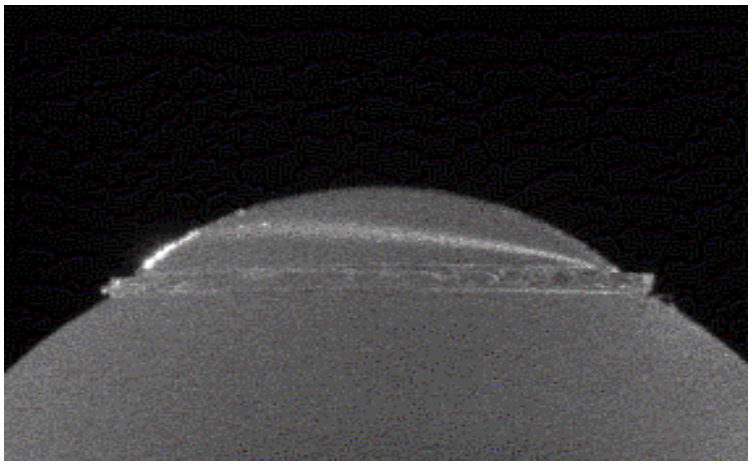

Figure 5.5:

Photographic still exhibiting maximum nasal-limbal focusing at 20 º posterior to the coronal plane

As verified through initial novel lab-based measurements, the beam incident temporally at the optimum 20 º was focused intensely enough to empirically measure the transmission of the RubrEye. When compared to the photographic still of PLF captured across the RubrEye at a 20 º input angle in figure 5.5, it can be seen that the refraction of a He-Ne laser corresponds well with the model. It was at this angle where maximum nasal-limbal focusing was noted both in the model and through focusing of the laser beam. Please note also the glare from the RubrEye's surface at the temporal side due to the relatively large angle of incidence (20 º) in figure 5.5. This inevitably contributes to losses by inter-media Fresnel reflections.

There is a large dependency on input angle for PLF effects to result in focusing of UVR at the nasal limbus. With the system designed here incorporating the RubrEye, it can be demonstrated that a beam emerging from a steep angle of approximately 30 º posterior to the coronal plane and striking the temporal cornea will result in the beam traversing the corneal dome and emerging above the nasal limbus, striking the palpebral fissure, as shown in figures 5.6 and 5.7. As this beam is modified to a less oblique coronal angle, the resultant focal point shifts towards the nasal limbus until finally striking it at 20 º posterior to the coronal plane, as shown in figures 5.4 and 5.5. Further reducing the coronal angle of incidence to approximately 10 º causes the beam to focus at a point intraocularly where the inner retina is situated beneath the nasal limbus, as shown in figures 5.8 and 5.9. These observations confirmed the critical nature of angular input optics on eliciting maximum PLF occurrence at the nasal-limbal region. These

observations could possibly further back up the hypotheses of a causal relationship of UVR with basal cell carcinoma's occurring at the inner canthus and cortical cataracts occurring due to focusing of UVR at this region.

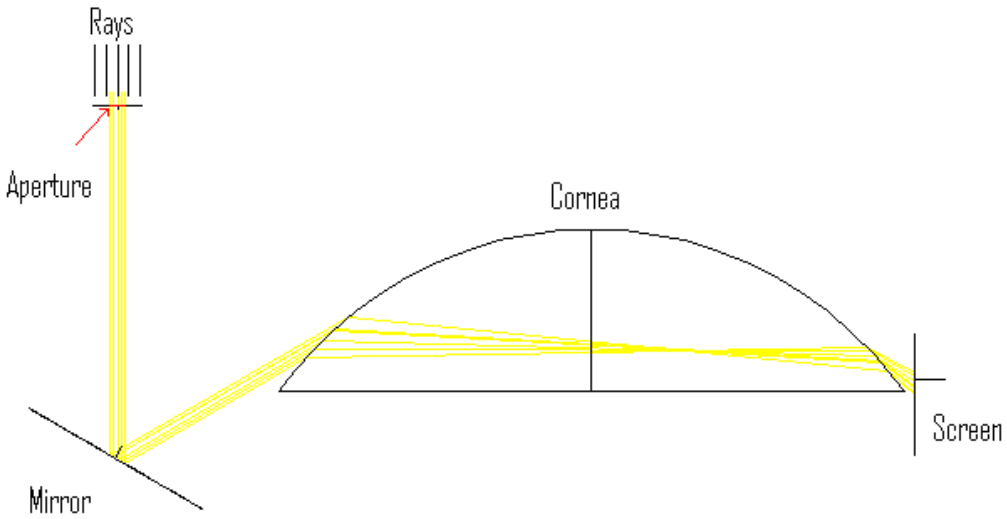

Figure 5.6:

30 º angle of incidence at temporal cornea resulting in light emerging above nasal limbus.

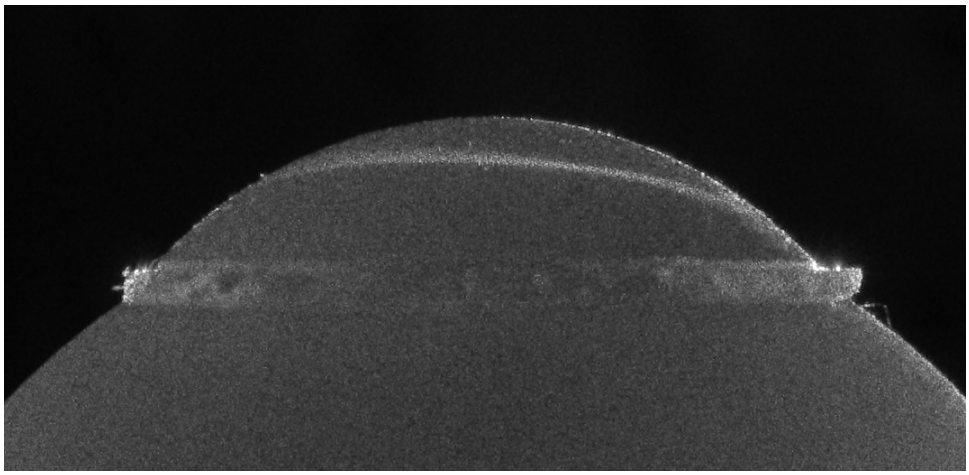

Figure 5.7:

30 º angle of incidence at temporal cornea of He-Ne laser demonstrating light escaping from cornea above nasal limbus.

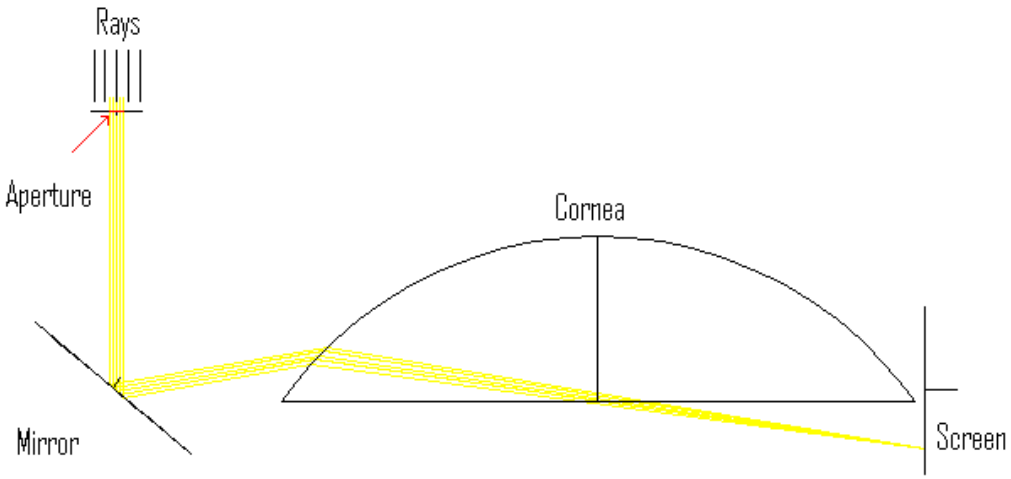

Figure 5.8:

10 º angle of incidence at temporal cornea of He-Ne laser resulting in light focusing at inner retina, possibly being absorbed by the human lens.

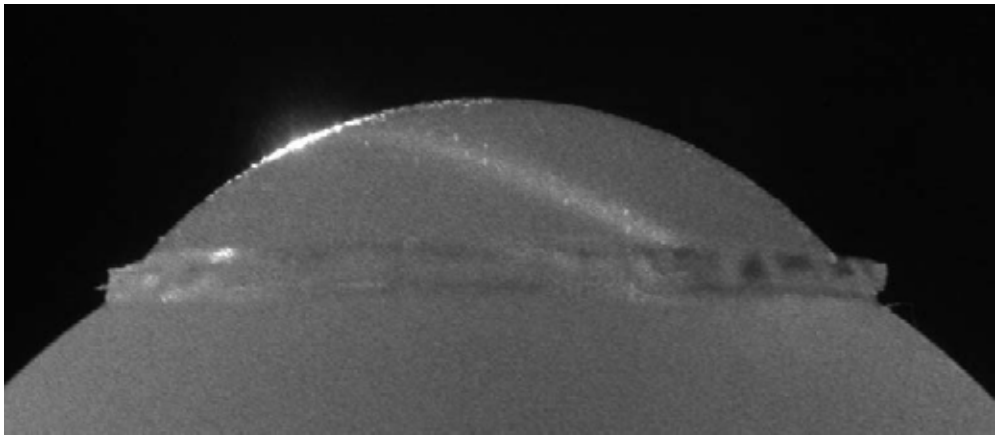

Figure 5.9:

10 º angle of incidence at temporal cornea resulting in light being intensely directed towards the lens.

5.4 Novel Lab Based PLF Transmission System Design

Having gained a good understanding of the mechanisms and temporally incident angles by which PLF causes rays to focus at the limbus for a 633 nm He-Ne emission line, a novel laboratory-based setup was designed, constructed and tested to measure the RubrEye's transmission for a broadband source, prior to performing similar measurements at the human cornea. The RubrEye was used as a test eye with the broadband source and novel fibre optic setup so that any problems encountered during testing would be resolved before testing on a human eye, thereby limiting the radiation exposure to the human eye. In addition, if problems were encountered while measuring the corneal transmission *in vivo*, they could be more easily remedied through the fundamentals of measurement gained through testing with the RubrEye.

An Ocean Optics DH-2000 Deuterium Tungsten Halogen source was used for measurements as it provided a combined continuous spectrum from 215 – 2000 nm in a single optical path. Consisting of two separate lamps, the deuterium had a wavelength range of 215 – 400 nm, while the halogen provided radiant energy in the 360 – 2000 nm range. When both sources were in use, the operating principle was based on the tungsten halogen lamp being directed through a small diameter aperture in the deuterium bulb, resulting in one continuous spectrum which can be seen in figure 5.10 in green. The blue spectrum is that of the tungsten halogen lamp only. When both were switched on it can be seen that the UVR region was very intense by comparison with the tungsten halogen alone, the

UVR output of which was too low to measure RubrEye and corneal transmission *in vivo*. To gain optimal spectral output, with little drift, the lamps were always left to warm up for 40 minutes, as recommended.

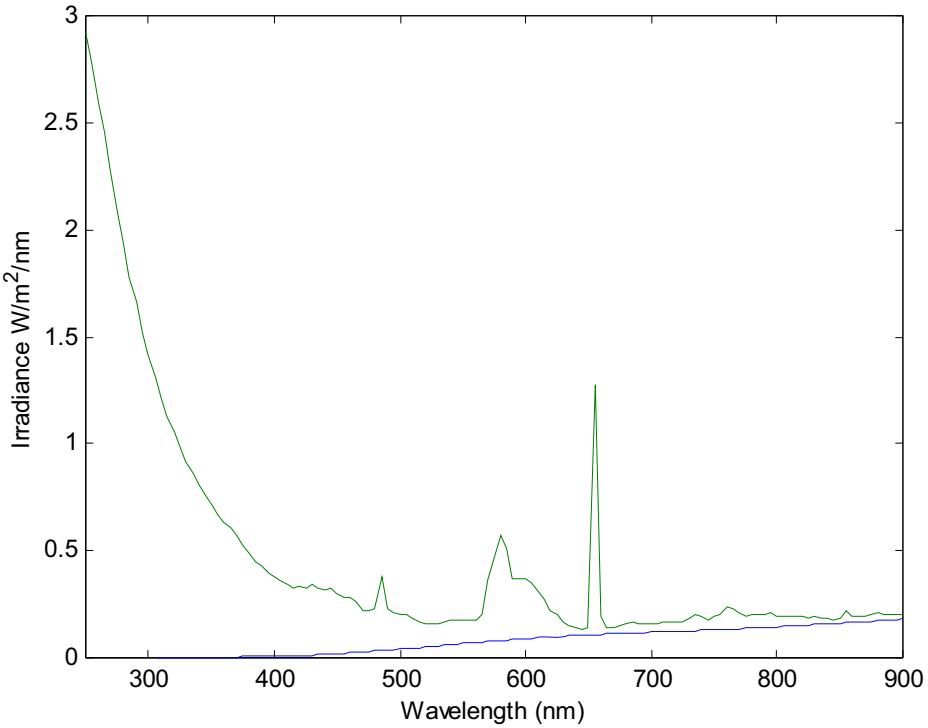

Figure 5.10:

Continuous Spectrum provided by Ocean Optics DH-2000

Deuterium Tungsten Halogen Source in green, and Tungsten Halogen in blue

The DH-2000 Deuterium Tungsten Halogen source was used for transmission measurements of the RubrEye and human cornea as it provided UVR to 215 nm[457], although as with most spectrometers the reliability of the S2000 employed for detection fell off closer to its detection limit of 200 nm. However, while both the tungsten and deuterium were used for the RubrEye measurements,

only the tungsten was used for *in vivo* measurements initially. For the *in vivo* measurement shown in section 5.6, the setup was finalised and a reference spectrum recorded without the test subject in place. The tungsten source was then passed across the eye, from temporal to nasal limbus, so that a pronounced focusing of the tungsten halogen light was clear at the nasal limbus. Only then was the deuterium switched on and a transmission spectrum recorded.

The original spectrometer used in spectral testing was an Ocean Optics S2000 single beam miniature fibre optic spectrometer which is designed to accept light most efficiently through single strand optical fibres with SMA 905 connectors. This consists of a 2048-element linear CCD-array which detected radiant energy dispersed by a fixed diffraction grating across this CCD-array. Its spectral range was 250 – 800 nm, with spectral resolution limited by the size of the slit (if present) or in this case, the diameter of the collecting fibre optic attached[458].

As increasing noise was introduced to the system at wavelengths shorter than approximately 300 nm due to the inherent problem of relatively poor UV response associated with micro-spectrometers, an updated version of the S2000, the USB2000 UV/Vis, was assessed. This spectrometer had a 50 μm slit and spectral range of 200 – 850 nm. While the size of this slit gave better spectral resolution, the practicality of using it in a set-up to measure PLF had to be considered. The main drawback was the slit size. Radiation throughput to the detector did not permit good signal-to-noise across the UV/Vis wavebands. In

effect, it was a trade-off between spectral resolution and signal-to-noise. Due to the low light levels involved with this type of research at the fibre optic sensing end, the S2000 micro-spectrometer was chosen above the USB2000 as the spectral resolution could be determined by changing the fibre optic employed depending on the level of resolution sought for a given measurement.

To determine the spectral resolution of the Ocean Optics S2000 spectrometer used for RubrEye and corneal transmission and to ensure it was sufficiently accurate to determine the "true" shape of these transmission spectra, an Ocean Optics CAL-2000 Mercury Argon wavelength calibration source which produced low pressure mercury and argon emission lines from 253 - 1700 nm was used. A number of prominent emission lines fell within the bandpass of the spectrometer used and these are outlined in Table 5.1.

Mercury Argon Calibration Peaks	
253.65 nm	404.66 nm
296.73 nm	407.78 nm
302.15 nm	435.84 nm
313.16 nm	546.08 nm
334.15 nm	576.96 nm
365.01 nm	579.07 nm

Table 5.1:

CAL-2000 Mercury Argon Calibration Source Emission peaks

A number of fibres were tested with the CAL-2000. These included 50 µm, 100 µm, 200µm, 400µm and 600 µm fibres and their respective colours in figure 5.11 are blue, black, red, green and magenta. As can be seen from figure 5.11, a number of these emission lines were well resolved for the smaller diameter fibre optics, most noticeably the lines at 253.65 nm, 296.73 nm, 313.16 nm, 365.01 nm, 435.84 nm and 546.08 nm. However, two emission lines appear at approximately 507 nm and 626 nm and these can be attributed to 2nd order effects of the 253.65 nm and 313.16 peaks respectively.

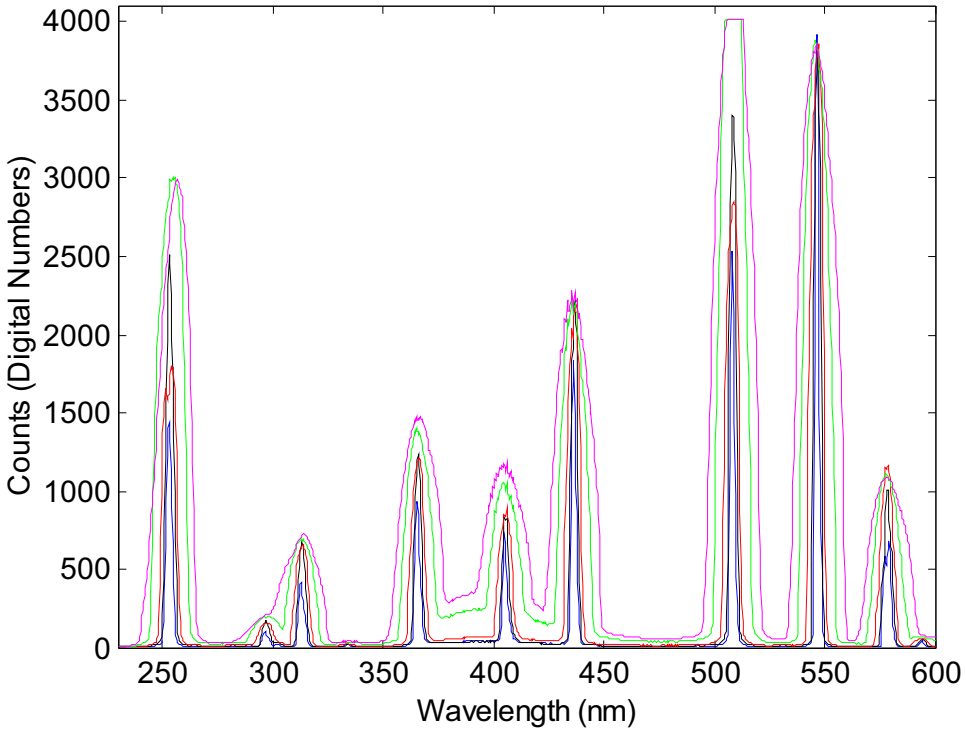

Figure 5.11:

Illustration of difference in bandwidths of different diameter fibres.

The Full-Width Half-Maximum (FWHM) for the peaks 365.01 nm and 546.08 nm were calculated. The width of each peak for the five fibres at the two separate wavelengths was determined and these fibre optic bandwidths are given in figure 5.12. The blue circles are the widths at the 546.08 nm peak and the red circles are the 365.01 nm peak.

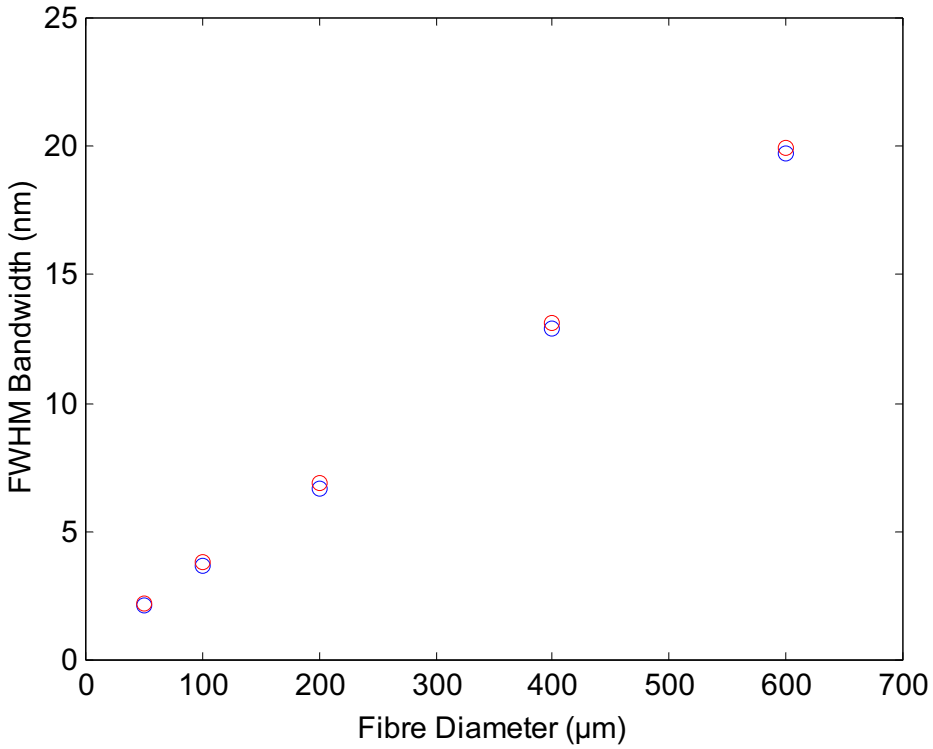

Figure 5.12:

Full Width Half Maximum Bandwidth (nm) against Fibre Diameter (µm) for 365.01 nm and 546.08 nm lines from CAL-2000.

Considering the trade off between light levels in the fibre optic transmission system and spectral resolution required to accurately determine the shape of the RubrEye and corneal transmission spectra, the 200 µm fibre was considered to provide sufficient spectral resolution, while permitting satisfactory

light levels pass to the micro-spectrometer. The bandwidth provided by a 200 μm fibre of around 7 nm is considered adequate for the investigations of corneal transmission when typical data in the literature is examined, particularly the UVR cut-off around 290 to 300 nm[459 460 461 462 463 464]. The RubrEye equivalent cut-off was found to be similar in shape to the cornea.

In summary, the best available source and detection instrumentation and components were researched and tested rigorously. Their combined application was the measurement of the RubrEye transmission across the UV/Vis wavebands, and ultimately through these investigations, the corneal transmission was measured *in vivo*.

5.5 Novel PLF Transmission of RubrEye

To prove the methodology of measuring the spectral transmittance of the RubrEye via the PLF method, the RubrEye used for these investigations was bisected using a ceramic blade along the equator leaving a hemisphere with the cornea at front and a clear equatorial rear plane. This was performed as the exterior retina of a whole RubrEye was a diffuse surface and optical coupling of focused light here into a fibre optic proved complex. The axial length from the corneal apex to the clear back section was very similar to the corneal diameter of the RubrEye, both being approximately 12.5 cm. This was advantageous for the purpose of transmission measurements, since a reference spectrum of a known thickness of polydimethylsiloxane was needed for comparison with subsequent PLF measurements. A 200 μm fibre optic from the DH-2000 source was directed

precisely through the corneal apex and the collecting 200 µm bare fibre was butt coupled to the clear rear section, as in figure 5.13. The RubrEye used for this work did not have an iris inserted during the manufacture process. This was purposely designed as it was found that the insertion of an iris increased the intricacy of detection as it bordered on the limbus and caused unwanted reflections and absorption of the focused beam.

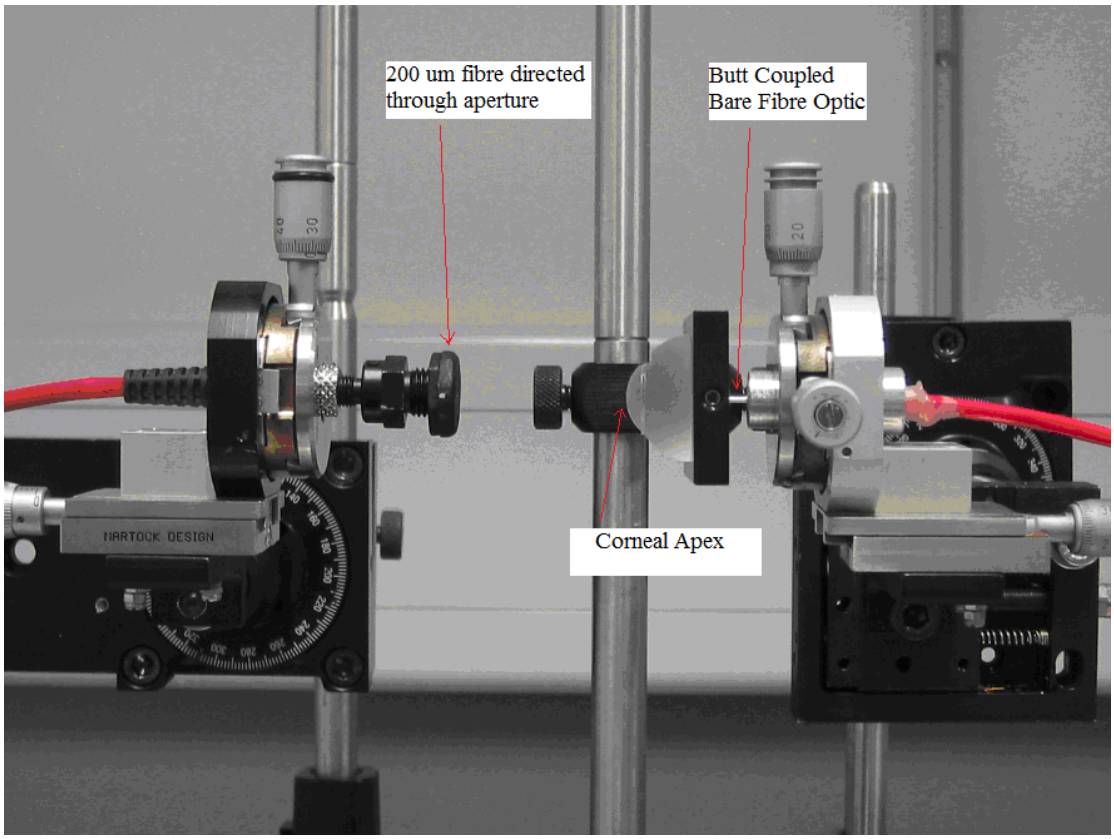

Figure 5.13:

RubrEye transmission setup with bare fibre butt coupled to rear section

The launch end of the novel setup to investigate PLF across the RubrEye consisted of a 200 µm launch fibre to which an Ocean Optics' 74-UV UV/Vis collimating lens was attached. To limit the diameter of the adjustable collimated

beam, a 1 mm aperture was attached to the other side of the lens. This system provided a collimated beam of 1 mm diameter over approximately 15 cm. The whole setup was fixed inside a fine control X-Y-Z translation stage, which itself was attached to a standard X-Y-Z translation bench stage which allowed greater movement of the launch end by shifting the whole stage up or down an optical post so that the collimated beam was always centred at the temporal cornea. The angle of this launch fibre was adjusted by means of a 1 º incremental rotational stage. A similar setup was assembled for the collecting fibre, as seen in figure 5.14.

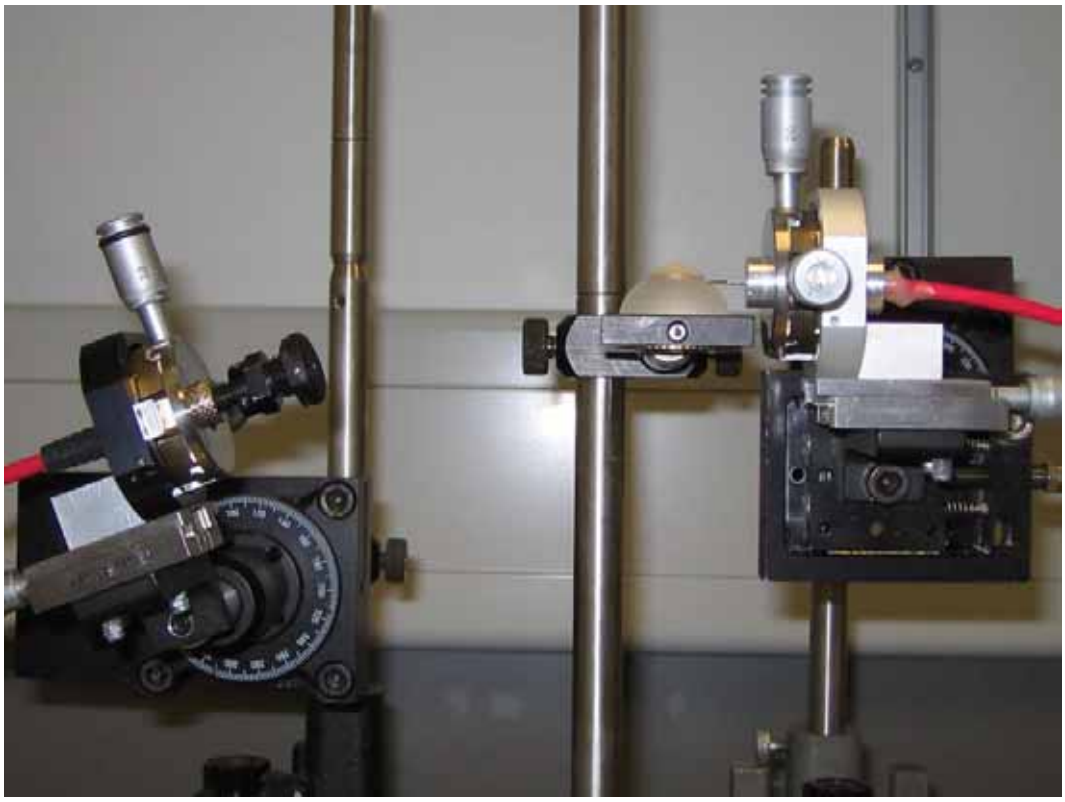

Figure 5.14:

Novel angular PLF measurement system with RubrEye

If there was focusing of the 1 mm beam across the cornea to a point at the limbus, the requirement of the sensing fibre optic was that it was as close to the nasal limbus as possible for the focused beam to be coupled. A standard SMA fibre optic did not suffice as its coupling ferrule prohibited close contact with the limbus. In order to get within close proximity of the limbus, a 600 μm fibre was modified by removing the ferrule, cleaving the whole fibre and stripping the surrounding protective plastic back to 1 cm from the bare fibre tip. The bare tip was then polished using Buehler® Metadi® Supreme Polycrystalline Diamond Suspensions. Firstly 1200 grit silicon carbide paper was used to polish the fibre tip' surface and was subsequently finely polished using a water based 3 μm diamond suspension. The tip was then analysed with a microscope objective lens to verify no degradation or blemishes on the surface. A mount was assembled which allowed the fibre to fit snugly inside with no movement, and this in turn was secured inside the fine control X-Y-Z translation stage. Care was taken to ensure that the only light striking the collecting fibre was the focused beam at the limbal region by recording measurements in a dark room. It must also be noted that the bare 600 μm fibre was connected via a barrel connector to a 200 μm fibre for all subsequent measurements for adequate spectral resolution. This coupled with the fact that it provided good light throughput and signal-to-noise when compared to smaller diameter fibres made it the most beneficial choice, as shown in section 5.4.

Although the transition from cornea to sclera of the RubrEye was a good representation of the limbus and a smooth continuous surface was attainable,

actually detecting a beam of radiation at this point proved quite difficult. This was due to the fact that at this curved boundary, radiation did not escape the RubrEye as it would do at a plane surface. It appeared to escape almost conically from the non-optically smooth surface, making detection of this refracted and scattered radiation by a fibre optic impractical. By finely cutting a small section of the RubrEye's limbus away with a ceramic blade along the limbus, optically clear vertical and horizontal surfaces were left exposed just at the limbus. This permitted the bare fibre tip to be placed just at the limbus above the horizontal surface and facilitated the detection of radiation traversing from the temporal cornea to the nasal aspect. Regular inspection and cleansing of the fibre tip was conducted prior to every set of measurements, including those of a human test subject to avoid contamination. This section is shown in figure 5.15 with the 1 mm aperture at a 20 º angle on the temporal side and the bare fibre tip at the sensing region of the sectioned limbus.

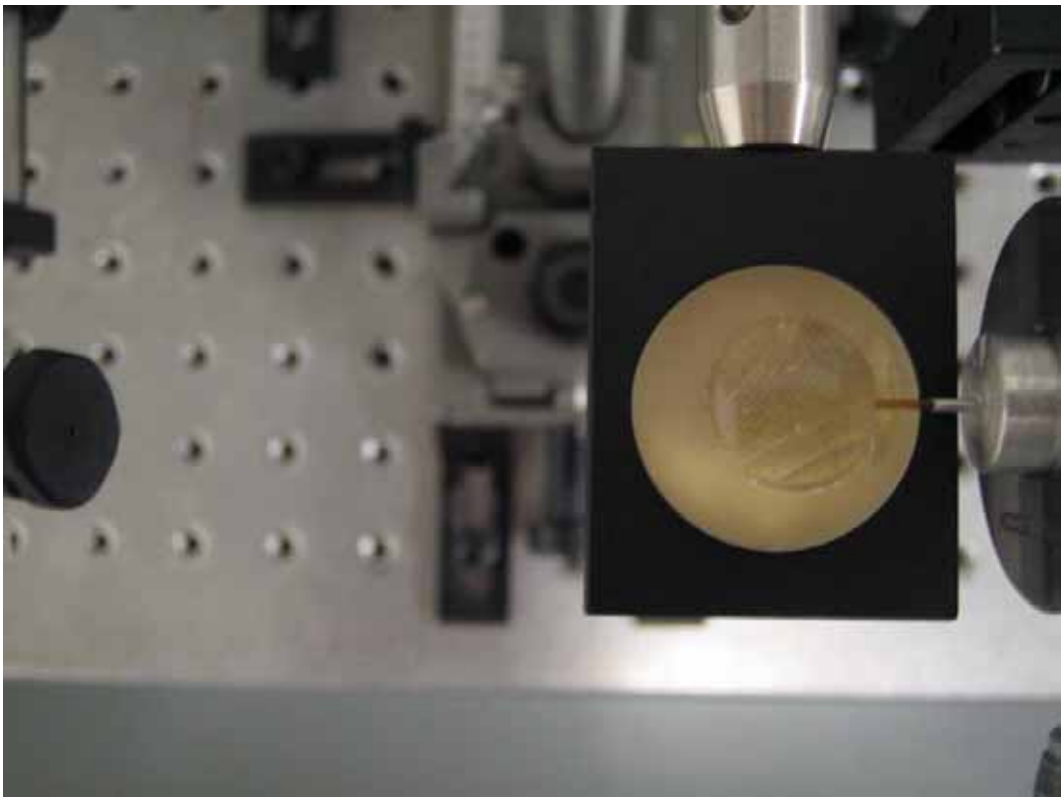

Figure 5.15:

Plan view of bare fibre at clear limbal section

For all transmission measurements of the RubrEye, the distance between the DH-2000 lamp launch fibre and the collection fibre was ~ 15 cm, approximating the distance which would be used in later experiments with the RubrEye and human cornea. The collecting fibre was axially manipulated using the fine controls of the X-Y-Z translation stage so that the collimated beam striking it was at a maximum at all times for repeatability prior to taking a reference spectrum. For each axis, the bare fibre progressed from relatively weak signal at the periphery of the beam, through the most intense signal at centre, and finally passing through relatively weak signal at the opposite periphery. Once the signal was maximised, a dark current spectrum with an integration time of 5 msec

and 100 spectra averaging was recorded. These values were chosen as they provided good signal-to-noise and good smoothing of the curves in the shortest time possible. This was important when coupling the tungsten and deuterium across the human eye. It was necessary to perform measurements as quickly as possible so as not to irradiate the eye for any longer than necessary. A reference spectrum of the light source was then recorded with similar PC acquisition and physical setup parameters, such as distance from launch to coupling fibre. With a reference spectrum recorded, the RubrEye was moved into place without disturbing either fibre optic. The bare fibre tip was located at the horizontal section of the limbus and transmission spectra were recorded for comparison with those recorded straight through the RubrEye.

The transmission of the RubrEye is now presented in figure 5.16. The black transmission curve is the average of five transmissions which were recorded by passing the collimated beam through the corneal apex and collecting the focused light with the butt coupled fibre optic at the back of the exposed clear hemisphere. The transmittance displayed in red is the average of five measurements which were recorded at a temporal incident angle of 20 º posterior to the coronal plane and collected by the fibre butt coupled to the nasal limbus.

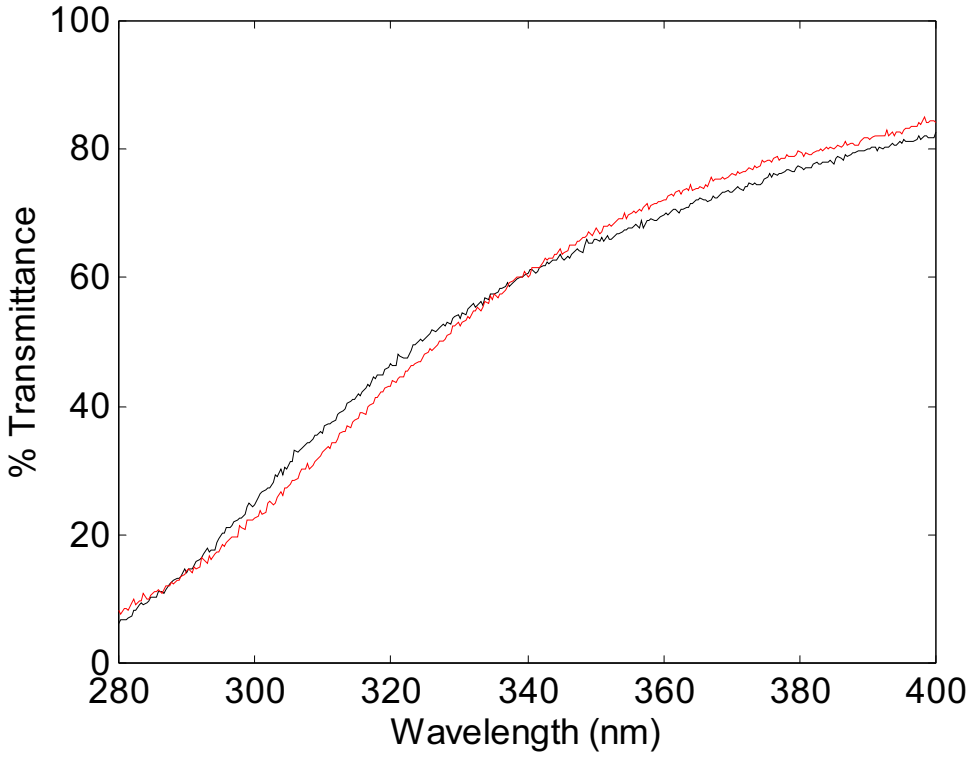

Figure 5.16:

Transmittance of RubrEye as measured through the corneal apex and at a PLF angle of 20 º posterior to the coronal plane.

While the transmission recorded with the micro-spectrometer through the corneal apex was very consistent, there was slight variation in the transmission recorded via the PLF method, as would be expected with such an oblique angle. This variation was minimised by reducing the effect of chromatic aberration associated with off-axis fibre optic light coupling. Chromatic aberration could be observed as the sensing fibre was moved along the horizontal plane around the exposed limbal region. The peak intensity of the real-time transmittance spectrum shifted from the UVR region to the red in the visible as the fibre was moved further back from the exposed vertical section. As it was the UVR region which

was of most interest, the collecting fibre was always situated a distance away from the vertical section such that the UVR waveband intensity was maximised and the visible did not vary across. In doing so, the highest possible UVR transmission was achieved, and as can be seen, this PLF method of measuring the transmission across the RubrEye cornea compared well with the standard procedure for measuring the transmission of a homogenous material.

5.6 Novel PLF Transmission of Human Cornea *in Vivo*

To date, published human corneal transmission data from many different groups from the UV to visible portion of the spectrum has been quite inconsistent. This is most probably due to differences in experimental design, instrumentation used and condition of cadaver corneas. Preservation of corneas immediately post-mortem is essential in maintaining optical clarity of this tissue. Since the transmission decreases dramatically with time across the UV-Vis, ideally the corneal transmission would be measured *in vivo*.

Using the principles and capabilities of the PLF system demonstrated in section 5.5, a novel transmission measurement system was designed to measure the corneal transmission of a human test subject *in vivo*.

The experimental method devised to measure the human corneal transmittance *in vivo* was adapted from the work with the RubrEye in section 5.5. The same 200 μm launch fibre was used, but the sensing fibre was a 200 μm fibre. The bare 600 μm fibre used for the measurements with the RubrEye was

considered too hazardous due to the necessity for it to be extremely close to the exposed human cornea. In general, a distance of 1 mm separated the bare fibre tip and cornea, so an unmodified 200 μm fibre was chosen as the sensing fibre as it provided adequate spectral bandwidth and good signal to noise, as noted in section 5.4.

A headrest removed from a slit lamp biomicroscope was adapted and fixed to a 90 cm x 60 cm optical bench. The headrest allowed a subject's head to be supported firmly as is the requirement during slit lamp biomicroscopy. It allowed reasonably sensitive vertical movement of a subject's head over a relatively large distance which was desirable when aligning the optics of the transmission setup. Due to the symmetrical design of the headrest, a 5 cm piece of the left upright was removed at a height level with the average subject's lateral ocular field. This facilitated a relatively large lateral angular rotation field of the launch fibre and ease of movement closer to and away from the ocular orbit when necessary. The launch and detecting fibre were adapted slightly from the RubrEye setup to suit the upright *in vivo* setup, but the same principles of the X-Y-Z setup and alignment applied as described in section 5.5.

When aligned, and a reference spectrum of the stabilised DH2000 lamp was recorded, the launch fibre was rotated to a preset angle of usually between 15 º to 25 º posterior the coronal plane. The subject then sat at the headrest with the distance of the collimated launch beam approximately 10 cm away from the temporal cornea. This value depended on incident angle and wasn't a critical

factor since the beam was considered well collimated by the lens over a distance of up approximately 15 cm. With the aid of a point of fixation on a mirror placed in front of the subject, adjustment of the head was made to an upright and comfortable position. Through use of the mirror, both the subject and aid guided the launch fibre on the X-Y-Z translation stage until the brightest spot perceivable appeared just at the nasal limbus. It was assumed the beam was at the limbus when the sclera was strongly illuminated by diffuse scatter from the limbal-scleral junction as in figure 5.17.

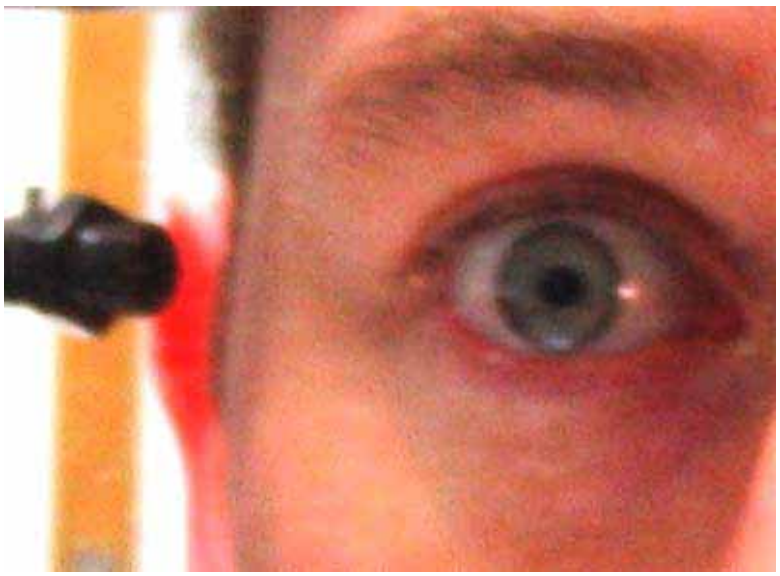

Figure 5.17:

Illumination of the limbal-scleral junction by a collimated beam 20 º laterally oblique.

By rotating the launch fibre slightly more posteriorly, the beam emerged from the cornea and could be seen faintly on a piece of paper inserted adjacent to the inner canthus. The launch fibre was then clamped to the optical bench with a magnetic base. At this point, the subject was helped guide the 200 μm sensing fibre over the nasal ridge and carefully towards the nasal limbus while gazing at a point of fixation marked on the mirror. With guidance from the aid, the fibre was moved to within 2 mm from the illuminated corneo-limbal region. At this point the fine control was used by the subject to move to approximately 1 mm from the surface of the cornea, at which point real-time corneal transmission signal was

observed. The aid always verified by visual inspection that the direct beam did not illuminate the sensing fibre optic and that no stray light emerged over the corneal apex. Either of these would have caused a false transmission spectrum. In this way, any light entering the sensing fibre optic had to have traversed and escaped from the cornea itself.

A number of trial measurements were taken using this setup for a series of angles. It was found that a similar temporal catchment angle to that of the RubrEye and in the literature of approximately 20 º posterior to the coronal plane produced maximum transmission spectra.

The spectra recorded at temporally oblique angles of approximately 20 º showed variation initially, but by making slight setup adjustments, better measurement consistency was achieved. The main factor contributing to variability in this novel setup were chromatic aberration effects of the cornea. By finely scanning the sensing fibre across the emergent beam at the cornea's curved surface, the maximised signal shifted from the red to the UV region always. As the sensing fibre could not be placed at a symmetrical angle to the launch fibre on the opposite side of the eye due to the presence of the nasal ridge, to minimise this effect a compromise was reached whereby the UVR transmittance was always maximised with the visible region reaching a plateau. The reasoning behind this was similar to that of the RubrEye outlined in section 5.4. By maximising the UV and visible regions in this way, it is acceptable to assume that data obtained via

this methodology are a true representation, as demonstrated by the RubrEye transmission tests, of the corneal transmission spectrum across this waveband *in vivo* as they compare favourably to other published data, in particular that of Dillon's cadaver cornea[465], as can be seen in figure 5.18.

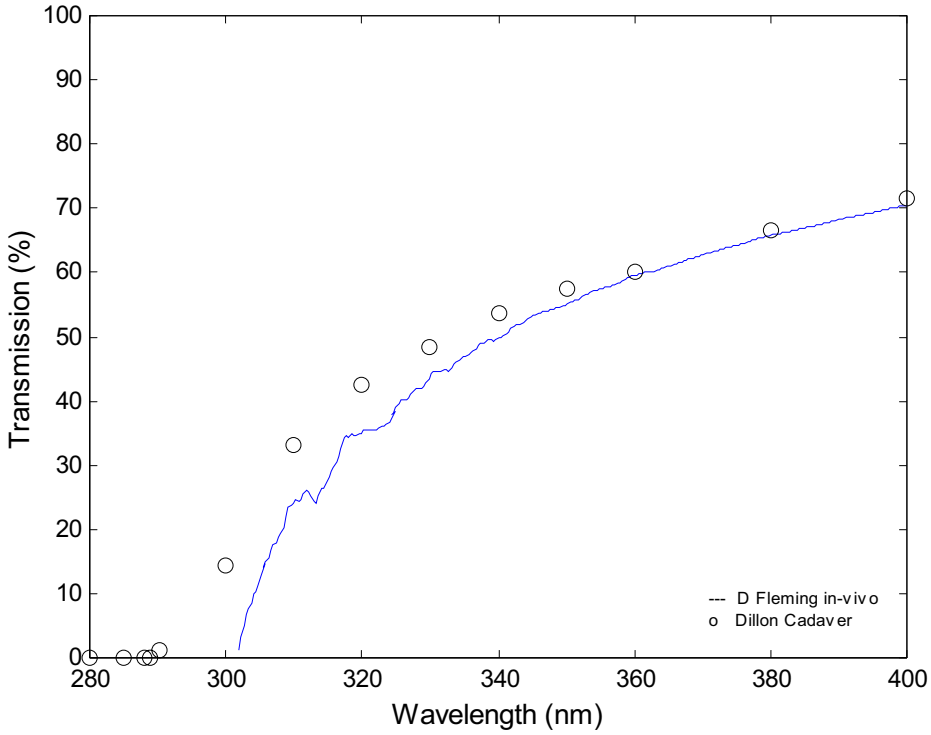

Figure 5.18:

In vivo corneal transmission measured with designed PLF method in blue, compared to cadaver human cornea.

The in-vivo corneal transmission has a similar profile to that of Dillon but with greater attenuation, particularly down at UVB wavelengths where the specific corneal attenuation coefficient is greater, due to the additional pass through the cornea and the greater corneal thickness encountered at PLF incident angles. It should be noted that due to difficulties in acquiring the PLF

transmission spectra in-vivo and the desire to limit ocular UVB exposure, the transmission spectrum shown is part of a limited set of data used to prove the method. Further research is currently underway in the Biomedical and Environmental Sensing Group to acquire more rigorous data with an improved PLF optical system.

5.7 Conclusion

In conclusion, a novel and reliable method of measuring the corneal transmission *in vivo* has been designed, constructed and tested. By incorporating modelling software, it was possible to ascertain the range of angles for which PLF would occur for the anatomically based homogenous RubrEye. Based on this, a laboratory based setup was then constructed to investigate the modelling results both photographically and empirically, by measuring the transmission of the RubrEye straight through and at various PLF angles. As an extension to this, and to our knowledge, the first time it has been achieved, the human corneal transmission spectrum has been measured *in viv*o.

Chapter 6

Discussion and Conclusions

Coupled with typical facial structure, the intricate spatial and temporal variations that occur in the environment which affect the intensity and distribution of solar UVR across the anterior ocular surface are numerous. In this thesis, it has been endeavoured to narrow the environmental variables which affect this distribution by measuring the solar UVR irradiance across the palpebral fissure using a novel solar blind UVR sensor array under specific solar insolation. In doing so, the major environmental factors contributing to the distribution of solar UVR across the array include the solar zenith angle and the solar azimuth angle. By facing the horizon at the four cardinal points, it was possible to elucidate this distribution as a function of solar position with respect to the field site coordinates under both direct and diffuse insolation environments. By testing the array in the field with two test subjects, it has been shown through the relative intensity data that distribution of solar UVR at the anterior ocular surface is subject specific, in that a persons facial anatomy plays a crucial role in the irradiance received.

Many previous studies have used alternative sensing devices such as polysulphone, which requires time consuming pre- and post-measurement analysis[410 411 412 413 414 415 416 417 418 419 420 421 422]. Although polysulphone has many merits, such as its action spectrum closely matching that of human skin, its reliability depends on rigorous calibration and any problems which may occur during measurement are only evident afterwards. It also only gives a cumulative

UVR dose, and not a continuous real time acquisition of the terrestrial irradiance. By designing, constructing and testing a solar blind mechanistic sensing device, many pitfalls of earlier systems have been removed. Using photodiode technology environmental ocular UVR sensing has been advanced using rigorously characterised novel systems. The proven benefits of these devices include their robustness, repeatability, large dynamic range, ease of use through specifically designed data acquisition software and multiple real time acquisitions. This latter point was a key feature which allowed us to statistically discriminate in the field and reduce the measurement error.

Together with the determination of the absolute irradiance values and the corresponding relative intensities at the ocular surface under direct and diffuse skies, for different test subjects at a range of solar angles, the potentially increased irradiance due to focusing of temporally incident radiation at the cornea to the corneo-scleral region was investigated. By employing an anatomically correct model eye, the RubrEye, investigations of PLF using ray tracing analysis in tandem with a novel laboratory based PLF were achieved. The determination of the optimum temporally incident input angle which resulted in a focusing of a beam of radiation striking the nasal limbus was realised using the ray tracing suite. Based on these observations, the novel *in vitro* fibre optic setup centred around the RubrEye showed that as the launch fibre optic progressed from 30° to 20° to 10° posterior to the coronal plane, the temporally incident beam was refracted to above the nasal limbus, struck the nasal limbus and refracted intraocularly towards the lens and nasal retina for each of the angles respectively.

These launch angles compared favourably with other published data based on ray-tracing models and empirical measurements of maximal UVR intensity at the nasal limbal region. In these studies, there were found a range of different angles which resulted in maximal focusing of UVR at the nasal limbal region [320] [321] [322] [323] [324] [325] [326] [327] [328] [335]. The reason for such disparity across these studies can be attributed to different optical parameters inputted to the ray-tracing software, and actual physical setup of lab-based measurement systems, inclusive of varying human corneal shapes and diameters.

To establish if the refracted beam had a similar spectral transmittance to a uniform piece of the same RubrEye polymer, the transmittance of both were measured, by using the conventional method of directing the launch fibre normal to a homogenous polymer surface and detecting the transmittance, and by utilising the novel PLF setup to measure the transmittance across the RubrEye cornea, which was the same thickness. The resultant transmission spectra agreed favourably, permitting modification the setup to measure the transmittance of the human cornea *in vivo*, as the method had been proved with the RubrEye. Indeed, the resulting human cornea transmission spectrum correlated well with a cadaver transmission spectrum published by Dillon *et al*. [465] and improved on earlier published data by the Biomedical and Environmental Sensing Group [447].

Key aspects of the data that confirm the predictions given in 4.1.2 have been vindicated including:

- Predominantly, the absolute data was dominated by the test subjects facial anatomy and orientation with respect to the sun and solar zenith angle.
- The two test subjects showed consistently different relative intensities across the eye for the range of test insolation conditions and orientations, with test subject A having a higher and flatter relative intensity

One feature that one might have expected in the data was that there was no apparent nasal bias across the array for the insolation conditions tested, for the on-eye irradiance data and the relative data. This is true of the horizon facing data, as the nose protects this region for the most part, where a temporal bias was found, as can be seen in figures 4.7 to 4.14 for test subject A under direct insolation. This general trend was also found by Sakamoto *et al.* [446] for measurements made with a system which incorporated photodiodes placed around the ocular region of a mannequin head. Measurements performed across a similar timeframe while the mannequin faced the horizon highlighted that the nasal brow ridge reduced the amount of UVR incident at the nasal aspect of the lid fissure and that irradiance was highest temporally. However, as seen in figure 4.4, a nasal bias was found when looking directly skywards, as the protection provided by the nose was removed. This is considered a key finding as this is the typical resting position of

the majority of sunbathers. Adding to this, if non-UVR blocking tinted sunglasses are used while reading in this position for instance, the squint mechanism is suppressed and essentially, the anterior segment receives an increased dose.

Under diffuse insolation while looking towards the horizon, figures 4.15 to 4.22 also show a temporal bias both on-eye and in the relative data, albeit with a slightly flatter bias for the on-eye irradiance data, as would be expected due UVR being incident much more diffusely. These results compare very well with the dose distribution map presented by Sydenham *et al*, who utilised a polysulphone lens to measure the ambient distribution of diffuse solar UVR across the eye socket of a mannequin headform facing the north just before local noon [410]. In this study, the temporal portion was found to receive a greater solar UVR dose for this horizontal gaze due to nasal and brow ridge shading.

As expected, the diffuse irradiance levels on-eye in the work presented here are also less than the levels under direct irradiance, but are still significantly high, particularly, when a person's squint would be less pronounced due to the perceivably lower illumination conditions.

Comparison of the relative intensities shown in figures 4.23 to 4.26 highlights the significance of facial anatomy in determining the bias of UVR across the eye and the levels received at the anterior segment. Test subject B was shown to consistently have a higher and flatter relative intensity across the array. This is indicative of test subject B having a less pronounced nose and brow ridge. This finding demonstrates that along with SZA and other major environmental

determining factors, facial anatomy plays a key role in the levels and distribution of solar UVR across the palpebral fissure.

From the field research presented here, it has been established that the temporal cornea typically receives a greater UVR irradiance than the nasal cornea while gazing at the horizon. Yet, most ocular pathologies manifest at the nasal aspect. Although some ambiguity still exists regarding the pathogenesis of pterygium, it is commonly accepted that UVR plays a key role. For this reason, it is hypothesised that the focusing effects of PLF at nasal cornea, combined with the irradiance typically received under direct or diffuse irradiance, plays a key role in the increased lifetime exposure received here. By measuring the corneal transmittance *in vivo* with the novel fibre optic sensing system developed, the contribution of PLF could be added to the levels incident on the nasal limbal sensor. Although the terrestrial solar spectrum falls off in the UVB, the cornea transmits UVR to ~290 nm. It has been found by Coroneo that there can be a 20X focusing of UVR at the nasal limbus due to PLF, and through this focusing, there is an almost certain causal relationship between the focusing of these highly actinic UVR wavelengths and the nasal predilection of many ocular pathologies such as pinguecula and pterygia [322].

With the addition of a photodiode at a right angle to the temporal photodiode on the sensor array, it would be possible to determine the ambient irradiance at this point. In doing so, the additional contribution expected due to

PLF to the nasal photodiode could be estimated through multiplying the corneal transmittance data by the irradiance incident on the right angle photodiode.

Two different optical detection systems were designed, constructed and tested for the research presented here. As part of the recommendations for future work already underway, it is suggested that a more rigorous field based survey of the solar UVR field using the novel solar blind array be carried out to include a broader range of solar zenith angles and subject orientations. In doing so, the temporal irradiance that results in PLF to the nasal limbus can be added to the overall direct/diffuse irradiance determined by the array.

In conclusion, the novel solar blind sensor array system has been proven to be a reliable, quick and effective method for environmental ocular surveying to ascertain the levels and distribution of terrestrial UVR across the palpebral fissure. The distribution of terrestrial UVR has been found to be dominated by facial anatomy and solar zenith angle for a particular cardinal point orientation.

Human corneal transmission has been measured using PLF by a novel fibre optic detection method and the combination of the two systems will be the primary focus of future endeavours in the research group. A more rigorous sky survey with updated software and equipment is key to these future goals in tandem with further measurements of the human corneal transmittance *in vivo*. A recommendation for future objectives is to measure focusing of UVR at the nasal

cornea due to PLF and expand this method to measure the corneal transmittance *in vivo* and apply this to field measurements.

One final interesting application of the *in vivo* PLF measurement technique is the ability to determine corneal thickness using the Beer-Lambert Law as described in papers published by the author[466] [408].

[1] Gies P, Roy C, Toomey S, Tomlinson D. *Ambient solar UVR, personal exposure and protection.* Journal of Epidemiology, 1999, 9(6), S115 – S122.

[2] Baldy C, Greenstein V, Holopigian K, Seiple W, Stenson S. *Light, Sight, and Photochromics.* Transitions Optical Inc.Ch.1, 2002.

[3] http://www.icrsurvey.com/Study.aspx?f=uv_rays_0602.html
(Accessed 18 April 2008)

[4] Young AR. *The family of sunlight-related eye diseases.* Optom. Vis. Sci. 1994; 71(2), 125-144.

[5] Rosenthal FS, West SK, Munoz B, Emmett EA, Strickland PT, Taylor HR. *Ocular and facial skin exposure to ultraviolet radiation in sunlight: a personal exposure model with application to a worker population.* Health Phys. 1991; 61(1), 77-86.

[6] Pham TQ, Wang JJ, Rochtchina E, Mitchell P. *Pterygium, pinguecula, and 5-year incidence of cataract.* Am J Ophthalmol. 2005; 139(6), 1126-1128.

[7] Friedlaender MH. *Ultraviolet radiation and the external eye.* Int Ophthalmol Clin. 2005; 45(1), 49-54.

[8] Lee JK, Kim JC. *Progenitor Cells in Healing after Pterygium Excision.* Yonsei Med J 2007; 48(1), 48-54.

[9] Taylor HR, West SK, Rosenthal FS, Munoz B, Newland HS, Emmett EA. *Corneal changes associated with chronic UV irradiation.* Arch Ophthalmol. 1989; 107(10), 1481-1484.

[10] Al-Bdour M, Al-Latayfeh MM. *Risk factors for pterygium in an adult Jordanian population.* Acta Ophthalmol. Scand. 2004; 82(1), 64-67.

[11] Vajdic CM, Kricker A, Giblin M, McKenzie J, Aitken J, Giles GG, Armstrong BK. *Eye color and cutaneous nevi predict risk of ocular melanoma in Australia.* Int J Cancer. 2001; 92(6), 906-912.

[12] Vajdic CM, Kricker A, Giblin M, McKenzie J, Aitken J, Giles GG, Armstrong BK. *Incidence of ocular melanoma in Australia from 1990 to 1998.* Int J Cancer. 2003; 105(1), 117-122.

[13] Dushku N, Hatcher SL, Albert DM, Reid TW. *p53 expression and relation to human papillomavirus infection in pingueculae, pterygia, and limbal tumors.* Arch Ophthalmol. 1999; 117(12), 1593-1599.

[14] Lu P, Chen X, Kang Y, Ke L, Wei X, Zhang W. *Pterygium in Tibetans: a population-based study in China.* Clin Experiment Ophthalmol. 2007; 35(9), 828-833.

[15] Dushku N, Reid TW. *P53 expression in altered limbal basal cells of pingueculae, pterygia, and limbal tumors.* Curr Eye Res. 1997; 16(12), 1179-1192.

[16] Luthra R, Nemesure BB, Wu SY. *Frequency and risk factors for pterygium in the Barbados eye study.* Arch Ophthalmol. 2001; 119(12), 1827-1832.

[17] Paula JS, Thorn F, Cruz AA. *Prevalence of pterygium and cataract in indigenous populations of the Brazilian Amazon rain forest.* Eye. 2006; 20(5):533-536.

[18] Durkin SR, Abhary S, Newland HS, Selva D, Aung T, Casson RJ. *The prevalence, severity and risk factors for pterygium in central Myanmar: the Meiktila Eye Study.* Br. J. Ophthalmol. 2008; 92(1), 25-29.

[19] Guenel P, Laforest L, Cyr D, Fevotte J, Sabroe S, Dufour C, Lutz JM, Lynge E. *Occupational risk factors, ultraviolet radiation, and ocular melanoma: a case-control study in France.* Cancer Causes Control. 2001; 12(5), 451-459.

[20] Ramasamy B, Quah SA, Wishart MS, Hiscott P. *Temporal pterygium: benign or not?* Br J Ophthalmol. 2005; 89(11), 1533-1534.

[21] Tan CS, Lim TH, Koh WP, Liew GC, Hoh ST, Tan CC, Au Eong KG. *Epidemiology of pterygium on a tropical island in the Riau Archipelago.* Eye. 2006; 20(8), 908-912.

[22] Bergmanson JPG, Sheldon TM, Cullen AP. *A sting in the rays.* Optician. 1996; 212(5560), 17-22.

[23] Di Girolamo N, Chui J, Wakefield D, Coroneo MT. *Cultured human ocular surface epithelium on therapeutic contact lenses.* Br J Ophthalmol. 2007; 91(4), 459-464.

[24] Cotterill R. Biophysics, An Introduction. John Wiley & Sons Ltd., England, 2002.

[25] Akbar-Khanzadeh F, Jahangir-Blourchian M. *Ultraviolet Radiation Exposure from UV-Transilluminators.* J Occup Environ Hyg. 2005; 2(10), 493 – 496.

[26] Nash JF, Tanner PR, Matts PJ. *Ultraviolet A radiation: testing and labeling for sunscreen products.* Dermatol Clin. 2006; 24(1), 63-74.

[27] Andersen FA, Landry RJ. *Optical radiation measurements and instrumentation.* J Invest Dermatol. 1981; 77(1), 8-12.

[28] vanLoon GW, Duffy SJ. Environmental Chemistry – A Global Perspective. 2nd ed. Oxford University Press, 2005.

[29] Mohr SB, Garland CF, Gorham ED, Grant WB, Garland FC. *Could ultraviolet B irradiance and vitamin D be associated with lower incidence rates of lung cancer?* J Epidemiol Community Health. 2008; 62(1), 69-74.

[30] Pitts DG. *Sunlight as an Ultraviolet Source.* Optom Vis Sci. 1990; 67(6), 401-406.

[31] Monroy E, Calle F, Angulo C, Vila P, Sanz A, Garrido JA, Calleja E, Mũnoz E, Haffouz S, Beaumont B, Omnes F, Gibart P. *GaN-Based Solar-Ultraviolet Detection Instrument.* Appl. Opt. 1998; 37(22), 5058-5062.

[32] Diffey BL. *Sunlight, skin cancer and ozone depletion.* Issues in Environmental Science and Technology. Causes and Environmental Implications of Increased UV-B Radiation. 2000; 14, 107-119.

[33] Parrish JA, Jaenicke KF, Anderson RR. *Erythema and melanogenesis action spectra of normal human skin.* Photochem Photobiol. 1982; 36(2), 187-191.

[34] Bureau International des Poids et Mesures. *The International System of Units (SI)*. 2006; 8th Ed.

[35] Diffey BL. *Sources and measurement of ultraviolet radiation.* Methods. 2002; 28(1), 4-13.

[36] Bergmanson JPG, Sheldon TM. *Ultraviolet Radiation Revisited.* CLAO J. 1997; 23(3), 196-204.

[37] Gies P, Roy. *Ocular protection from ultraviolet radiation.* Clin Exp Optom. 1988; 71(1), 21-27.

[38] Reme C, Reinboth J, Clausen M, Hafezi F. *Light damage revisited: converging evidence, diverging views?* Graefes Arch Clin Exp Ophthalmol. 1996; 234(1), 2-11.

[39] Norval M, Cullen AP, de Gruijl FR, Longstreth J, Takizawa Y, Lucas RM, Noonan FP, van der Leun JC. *The effects on human health from stratospheric ozone depletion and its interactions with climate change.* Photochem Photobiol Sci. 2007; 6(3), 232-251.

[40] Matsumura Y, Ananthaswamy HN. *Toxic effects of ultraviolet radiation on the skin.* Toxicol Appl Pharmacol. 2004; 195(3), 298-308.

[41] Heck DE, Gerecke DR, Vetrano AM, Laskin JD. *Solar ultraviolet radiation as a trigger of cell signal transduction.* Toxicol Appl Pharmacol. 2004; 195(3), 288-297.

[42] de Gruijl FR. *Health Effects from Solar UV Radiation.* Radiat Prot Dosimetry. 1997; 72(3-4),177-196.

[43] Saraiya M, Glanz K, Briss PA, Nichols P, White C, Das D, Smith SJ, Tannor B, Hutchinson AB, Wilson KM, Gandhi N, Lee NC, Rimer B, Coates RC, Kerner JF, Hiatt RA, Buffler P, Rochester P. *Interventions to prevent skin cancer by reducing exposure to ultraviolet radiation: a systematic review.* Am J Prev Med. 2004; 27(5), 422-466.

[44] Glanz K, Mayer JA. *Reducing ultraviolet radiation exposure to prevent skin cancer - methodology and measurement.* Am J Prev Med. 2005; 29(2), 131-142.

[45] Saraiya M, Hall HI, Uhler RJ. *Sunburn prevalence among adults in the United States, 1999.* Am J Prev Med. 2002; 23(2), 91-97.

[46] Edström DW, Porwit A, Ros AM. *Effects on human skin of repetitive ultraviolet-A1 (UVA1) irradiation and visible light.* Photodermatol Photoimmunol Photomed. 2001; 17(2), 66-70.

[47] Lucas RM, Ponsonby A-L. *Ultraviolet radiation and health: friend and foe.* MJA. 2002; 177(11-12), 594-598.

[48] Batham G. *UV exposure and the eye.* Br Jour Optom Dispen. 1994; 2(10), 366-368.

[49] Gallagher RP, Lee TK. *Adverse effects of ultraviolet radiation: A brief review.* Prog in Biophys Mol Biol. 2006; 92(1), 119-131.

[50] Moehrle M. *Outdoor sports and skin cancer.* Clin Dermatol. 2008; 26(1), 12-15.

[51] Taylor SL, Coates ML, Vallejos Q, Feldman SR, Schulz MR, Quandt SA, Fleischer AB Jr, Arcury TA. *Pterygium among Latino migrant farmworkers in North Carolina.* Arch Environ Occup Health. 2006; 61(1), 27-32.

[52] Moseley H. *Ultraviolet and laser radiation safety.* Phys. Med. Biol. 1994; 39(11), 1765-1799.

[53] MacKie RM. *Effects of ultraviolet radiation on human health.* Radiat Prot Dosimetry. 2000; 91(1-3), 15-18.

[54] Mathur ML, Haldiya KR, Sachdev R, Saiyed HN. *The risk of pterygium in salt workers.* Int Opthalmol. 2005; 26(1-2), 43-47.

[55] Gies HP, Roy CR, Elliott G. *A proposed UVR protection factor for sunglasses.* Clin Exp Optom. 1990; 73(6), 184-189.

[56] de Gruijl FR, Longstreth J, Norval M, Cullen AP, Slaper H, Kripke ML, Takizawa Y, van der Leun JC. *Health effects from stratospheric ozone depletion and interactions with climate change.* Photochem Photobiol Sci. 2003; 2(1), 16-28.

[57] Roh S, Weiter JJ. *Light damage to the eye.* J Fla Med Assoc. 1994; 81(4), 248-251.

[58] Michael R, Lofgren S, Soderberg PG. *Lens opacities after repeated exposure to ultraviolet radiation.* Acta Ophthalmol Scand. 1999; 77(6), 690-693.

[59] Rogers CS, Chan LM, Sims YS, Byrd KD, Hinton DL, Twining SS. *The effects of sub-solar levels of UV-A and UV-B on rabbit corneal and lens epithelial cells*. Exp Eye Res. 2004; 78(5), 1007-1014.

[60] Slominski A, Pawelek J. *Animals under the sun: effects of ultraviolet radiation on mammalian skin.* Clin Dermatol. 1998; 16(4), 503-515.

[61] Sabburg J, Parisi AV, Wong J. *Effect of cloud on UVA and exposure to humans.* Photochem Photobiol. 2001; 74(3), 412-416.

[62] Kimlin MG, Parisi AV. *Ultraviolet radiation penetrating vehicle glass: a field based comparative study.* Phys Med Biol. 1999; 44(4), 917-926.

[63] Koronakis PS, Sfantos GK, Paliatsos AG, Kaldellis JK, Garofalakis JE, Koronaki IP. *Interrelations of UV-global/global/diffuse solar irradiance components and UV-global attenuation on air pollution episode days in Athens, Greece.* Atmos. Environ. 2002; 36(19), 3173-3181.

[64] Elsner P, Holzle E, Diepgen T, Grether-Beck S, Hönigsmann H, Krutmann J, Scharffetter-Kochanek K, Schwarz T, Luger T. *Recommendation: daily sun protection in the prevention of chronic UV-induced skin damage.* J Dtsch Dermatol Ges. 2007; 5(2), 166-173.

[65] Kimlin MG, Parisi AV, Carter BD, Turnbull D. *Comparison of the solar spectral ultraviolet irradiance in motor vehicles with windows in an open and closed position.* Int J Biometeorol. 2002; 46(3), 150-156.

[66] Moyal D. *Prevention of ultraviolet-induced skin pigmentation.* Photodermatol Photoimmunol Photomed. 2004; 20(5), 243-247.

[67] Rai R, Srinivas CR. *Photoprotection*. Indian J Dermatol Venereol Leprol. 2007; 73(2), 73-79.

[68] Reichrath J. *The challenge resulting from positive and negative effects of sunlight: How much solar UV exposure is appropriate to balance between risks of vitamin D deficiency and skin cancer?* Prog Biophys Mol Biol. 2006; 92(1), 9-16.

[69] Clarkson DM. *UV and the eye – the future unfolds.* Optician. 2001; 5785(221), 22-26.

[70] Grant WB, Strange RC, Garland CF. *Sunshine is good medicine. The health benefits of ultraviolet-B induced vitamin D production.* J Cosmet Dermatol. 2003; 2(2), 86-98.

[71] Wharton JR, Cockerell CJ. *The Sun: A Friend and Enemy.* Clin Dermatol. 1998; 16(4), 415-419.

[72] Parisi AV, Wong JC. *Erythemal irradiances of filtered ultraviolet radiation.* Phys Med Biol. 1997; 42 (7), 1263-1275.

[73] Parisi AV. *Physics concepts of solar ultraviolet radiation by distance education.* Eur. J. Phys. 2005; 26(2), 313-320.

[74] Hönigsmann H. *Erythema and pigmentation.* Photodermatol Photoimmunol Photomed. 2002; 18(2), 75-81.

[75] van der Leun JC, Forbes PD. *Ultraviolet tanning equipment: six questions.* Photodermatol Photoimmunol Photomed. 2005; 21(5), 254-259.

[76] Kullavanijaya P, Lim HW. *Photoprotection.* J Am Acad Dermatol. 2005; 52(6) ,937-958.

[77] Roy CR, Gies HP, Toomey S. *The solar UV radiation environment: measurement techniques and results.* J Photochem PhotoBiol: B. 1995; 31(1), 21-27.

[78] Pitts DG, Tredici TJ. *The Effects of Ultraviolet on the Eye.* Am Ind Hyg Assoc J. 1971; 32(4), 235 – 246.

[79] Sliney DH. *Ocular injury due to light toxicity.* Int. Ophthalmol Clin. 1988; 28(3), 246-250.

[80] Ayala MN, Michael R, Soderberg PG. *Influence of exposure time for UV radiation-induced cataract.* Invest Ophthalmol Vis Sci. 2000; 41(11), 3539-3543.

[81] Parisi AV, Kimlin MG, Mulheran L, Meldrum LR, Randall C. *Field-based measurements of personal erythemal ultraviolet exposure through a common summer garment.* Photodermatol Photoimmunol Photomed. 2000; 16(3), 134-138.

[82] Sliney DH. *Ultraviolet radiation effects upon the eye: problems of dosimetry*. Radiat Prot Dosimetry. 1997; 72(3-4), 197-206.

[83] Smith GJ, Miller IJ, Clare JF, Diffey BL. *The effect of UV absorbing sunscreens on the reflectance and the consequent protection of skin.* Photochem Photobiol. 2002; 75(2), 122-125.

[84] Spencer JM, Amonette R. *Tanning beds and skin cancer: artificial sun + old sol = real risk.* Clin Dermatol. 1998; 16(4), 487-501.

[85] Diffey BL. *Sunscreens and UVA protection: A major issue of minor importance*. Photochem Photobiol, 2001, 74(1), 61-63.

[86] Dongre AM, Pai GG, Khopkar US. *Ultraviolet protective properties of branded and unbranded sunglasses available in the Indian market in UV phototherapy chambers.* Indian J Dermatol Venereol Leprol. 2007; 73(1), 26-28.

[87] Schaefer H, Moyal D, Fourtanier A. *Recent advances in sun protection.* Semin Cutan Med Surg. 1998; 17(4), 266-275.

[88] Khazova M, O' Hagan JB, Grainger KJ. *Radiation and chemical degradation of UVR protection characteristics of fabrics.* Radiat Prot Dosimetry. 2007; 123(3), 369-377.

[89] Cole C. *Sunscreen protection in the ultraviolet A region: how to measure the effectiveness.* Photodermatol Photoimmunol Photomed. 2001; 17(1), 2-10.

[90] Diffey BL, Tanner PR, Matts PJ, Nash JF. *In vitro assessment of the broad-spectrum ultraviolet protection of sunscreen products.* J Am Acad Dermatol. 2000; 43(6), 1024-1035.

[91] Bernhardt JH, Matthes R. *Recent and Future Activities of the ICNIRP.* Radiat Prot Dosimetry 1997; 72(3), 167-176.

[92] Kudish AI, Lyubansky V, Evseev EG, Ianetz A. *Inter-comparison of the solar UVB, UVA and global radiation clearness and UV indices for Beer Sheva and Neve Zohar (Dead Sea), Israel.* Energy. 2005; 30(9), 1623-1641.

[93] ICNIRP/WHO/WMO/UNEP. *Global solar UV index. A practical guide*. Geneva, Switzerland: WHO; 2002.

[94] Gies P. *Photoprotection by clothing.* Photodermatol Photoimmunol Photomed. 2007; 23(6), 264-274.

[95] International Commission on Non-Ionizing Radiation Protection (ICNIRP). *Health issues of ultraviolet tanning appliances used for cosmetic purposes.* Health Phys. 2004; 84(1), 119-127.

[96] Diffey BL. *Climate change, ozone depletion and the impact on ultraviolet exposure of human skin*. Phys Med Biol. 2004; 49(1), R1-11.

[97] Gies HP, Roy CR. *Protective measures against solar UV exposures*. Radiat Prot Dosimetry. 1997; 72(3-4), 231-240.

[98] Janda M, Kimlin MG, Whiteman DC, Aitken JF, Neale RE. *Sun protection messages, vitamin D and skin cancer: out of the frying pan and into the fire?* Med J Aust. 2007; 186(2), 52-53.

[99] New C, Driscoll CMH, Kitchen K, Miners B. *The global solar UV index used in the United Kingdom.* Radiat Prot Dosimetry. 2000; 91(1-3), 313-315.

[100] Corrêa MP, Dubuisson P, Plana-Fattori A. *An overview of the ultraviolet index and the skin cancer cases in Brazil.* Photochem Photobiol. 2003; 78(1), 49-54.

[101] Moran DJ, Hollows FC. Pterygium and ultraviolet radiation: a positive correlation. Br J Ophthalmol 1984; 68(5), 343-346.

[102] Parisi AV, Wong JC, Kimlin MG, Turnbull D, Lester R. *Comparison between seasons of the ultraviolet environment in the shade of trees in Australia.* Photodermatol Photoimmunol Photomed. 2001; 17(2), 55-59.

[103] Moehrle M, Soballa M, Korn M. *UV exposure in cars.* Photodermatol Photoimmunol Photomed. 2003; 19(4), 175-181.

[104] World Health Organisation (WHO). *Health and Environmental Effects of ultraviolet radiation: A summary of Environmental Health Criteria 160 Ultraviolet Radiation.*. WHO/EHG/95.16, Geneva 1995.

[105] Diffey BL. *What is light?* Photodermatol Photoimmunol Photomed. 2002; 18(2), 68-74.

[106] Hermann C. *CIE publ. 125-1997, Standard erythema dose, a review and CIE DS 007.3/E Erythema reference action spectrum and standard erythema dose.* Color Research & Application. 1998; 23(2), 124-125.

[107] Ridyard A. *Assessing Ultraviolet Hazards Using Portable Measuring Instruments.* Radiat Prot Dosim. 2000; 91(1-3), 147-151.

[108] Harrison GI, Young AR. *Ultraviolet radiation-induced erythema in human skin.* Methods. 2002; 28(1), 14-19.

[109] Zigman S. *Ultraviolet A and Cataracts: Basic Research and Practical Applications.* Int Ophthalmol Clin. 2005; 45(1), 29-40.

[110] Scourfield MJW, Bodeker GE. *The influence of cloud and surface albedo on surface UV erythemal irradiance.* Phys. Chem. Earth (B). 2000; 25(5-6), 521-523.

[111] De Fabo EC. *Initial studies on an in vivo action spectrum for melanoma induction.* Prog Biophys Mol Biol. 2006; 92(1), 97-104.

[112] Parisi AV, Sabburg J, Kimlin MG. *Comparison of biologically damaging spectral solar ultraviolet radiation at a southern hemisphere sub-tropical site.* Phys Med Biol. 2003; 48(8), N121-129.

[113] Wong CF, Fleming RA, Thomas BW. *Relation of dose measurements to indexing protective devices for exposure to solar radiation*. SPIE Proc. (Ultraviolet Radiation Hazards). 1994; 2134B, 113-119.

[114] Valberg A. *Light Vision Color*. J Wiley & Sons, West Sussex, England 2005.

[115] Parisi AV, Downs N. *Variation of the enhanced biologically damaging solar UV due to clouds.* Photochem. Photobiol. Sci. 2004; 3(7), 643 – 647.

[116] Rettberg P Cockell CS. *Biological UV dosimetry using the DLR-biofilm*. Photochem. Photobiol. Sci. 2004; 3(8), 781-787.

[117] Piltingsrud HV, Fong CW, Odland LT. *An evaluation of ultraviolet radiation personnel hazards from selected 400-watt high intensity discharge lamps.* Am Ind Hyg Assoc J. 1978; 39 (5), 406 – 413.

[118] Parisi AV, Kimlin MG. *Horizontal and sun-normal spectral biologically effective ultraviolet irradiances.* J Photochem Photobiol B. 1999; 53 (1-3), 70-74.

[119] McKinlay AF, Diffey BL. *A reference action spectrum for ultraviolet induced erythema in human skin*. CIE J. 1987; 6, 17-22.

[120] Matts PJ. *Solar ultraviolet radiation: definitions and terminology*. Dermatol Clin. 2006; 24(1), 1-8.

[121] Weatherhead EC, Webb AR. *International response to the challenge of measuring solar ultraviolet radiation.* Radiat Prot Dosim. 1997; 72(3-4), 223-229.

[122] Kimlin MG, Olds WJ, Moore MR. *Location and Vitamin D synthesis: Is the hypothesis validated by geophysical data?* J Photochem Photobiol B. 2007; 86(3), 234-239.

[123] Horneck G. *Quantification of biologically effective environmental UV irradiance.* Adv Space Res. 2000; 26(12), 1983-1994.

[124] European Commission. Health & Consumer Protection Directorate-General. Directorate C – Public Health and Risk Assessment, C7. Scientific Committee on Consumer Products (SCCP). Opinion on: *'Biological effects of ultraviolet radiation relevant to health with particular reference to sunbeds for cosmetic purposes'.* SCCP/0949/05. 2006.

[125] Kaidbey KH, Kligman AM. *Cumulative effects from repeated exposures to ultraviolet radiation.* J Invest Dermatol. 1981; 76(5), 352-355.

[126] Roy CR, Gies HP. *Ultraviolet Radiation Protection Methods.* Radiat Prot Dosim. 2000; 91(1-3), 239-245.

[127] Sliney DH. *The merits of an envelope action spectrum for ultraviolet radiation exposure criteria.* Am Ind Hyg Assoc J. 1972; 33(10), 644-653.

[128] Wester U. *Analytic Expressions to Represent the Hazard Ultraviolet Action Spectrum of ICNIRP & ACGIH.* Radiat Prot Dosim. 2000; 91(1-3), 231-232.

[129] Pitts DG, Kleinstein RN. Environmental Vision: Interactions of the Eye, Vision and the Environment. 1993. Butterworth-Heinemann. USA.

[130] Piltingsrud HV, Stencil JA. *A portable spectroradiometer for use at visible and ultraviolet wavelengths.* Am Ind Hyg Assoc J. 1976; 37(2), 90 – 94.

[131] Sliney DH, Moss CE, Miller CG, Stephens JB. *Semitransparent curtains for control of optical radiation hazards.* Appl. Opt. 1981; 20(14), 2352-2366.

[132] Sliney D, Aron-Rosa D, DeLori F, Fankhouser F, Landry R, Mainster M, Marshall J, Rassow B, Stuck B, Trokel S, West T, and Wolfe M. *Adjustment of guidelines for exposure of the eye to optical radiation from ocular instruments: statement from a task group of the International Commission on Non-Ionizing Radiation Protection.* Appl. Opt. 2005; 44 (11), 2162-2176.

[133] INRC/IRPA. *Guidelines on limits of exposure to ultraviolet radiation of wavelengths between 180 nm and 400 nm (Incoherent Optical Radiation)*. Health Phys. 1985; 49(2), 331-340.

[134] Matthes R. ICNIRP Statement. *Guidelines on UV radiation exposure limits*. Health Phys. 1996; 71(6), 978.

[135] International Commission on Non-Ionizing Radiation Protection (ICNIRP). *Guidelines on limits of exposure to ultraviolet radiation of wavelengths between 180 nm and 400 nm (Incoherent Optical Radiation)*. Health Phys. 2004; 87(2), 171-186.

[136] Diffey BL. *The risk of skin cancer from occupational exposure to ultraviolet radiation in hospitals.* Phys. Med. Biol. 1988; 33(10), 1187-1193.

[137] Laperre J, Gambichler T. *Sun protection offered by fabrics: on the relation between effective doses based on different action spectra.* Photodermatol Photoimmunol Photomed. 2003; 19(1), 11-16.

[138] Blumthaler M. *Ambient levels of UV radiation.* BMC Plant Biology. 2005; 5 (Suppl 1): S5.

[139] Webb AR. *Ozone depletion and changes in environmental UV-B radiation.* Issues in Environmental Science and Technology. Causes and Environmental Implications of Increased UV-B Radiation. 2000; 14, 17-36.

[140] Streicher JJ, Culverhouse WC Jr, Dulberg MS, Fornaro RJ. *Modeling the anatomical distribution of sunlight.* Photochem Photobiol. 2004; 79(1), 40-47.

[141] Taylor HR. *Aetiology of climatic droplet keratopathy and pterygium.* Br J Ophthalmol. 1980; 64(3), 154-163.

[142] ACIA, Arctic Climate Impact Assessment, *Ch.5 – Ozone and Ultraviolet Radiation.* Cambridge University Press. 2005.

[143] Grifoni D, Carreras G, Sabatini F, Zipoli G. *UV hazard on Italian Apennines under different shading and ground cover conditions during peak tourist seasons of the year*. Int J Environ Health Res. 2006; 16(6), 427-437.

[144] Rafanelli C. *Effect of environmental factors on solar UV measurements.* Radiat Prot Dosim. 2001; 97(4), 423-428.

[145] Parisi AV, Kimlin MG, Wong JCF, Wilson M. *Diffuse component of solar ultraviolet radiation in tree shade.* J. Photochem. Photobiol. B. 2000; 54 (2-3), 116-120.

[146] Diffey BL. *Environmental exposure to UV-B radiation.* Rev Environ Health. 1984; 4(4),317-37.

[147] Kerr JB, McElroy CT. *Evidence for large upward trends of ultraviolet-B radiation linked to ozone depletion.* Science. 1993; 262(5136), 1032-1034.

[148] World Health Organisation. *Children's health and environment: A review of evidence.* Environmental issue report No. 29. WHO/EEA, 2002

[149] El-Nouby Adam M, El Shazly SM. *Attenuation of UV-B radiation in the atmosphere: Clouds effect, at Qena (Egypt).* Atmos Res. 2007; 41(23), 4856-4864.

[150] United Nations Environment Programme, Environmental Effects Assessment Panel. *Environmental effects of ozone depletion and its interactions with climate change: Progress report, 2007.* Photochem. Photobiol. Sci. 2008; 7(1)**,** 15-27.

[151] Webb AR. *Who, what, where and when-influences on cutaneous vitamin D synthesis.* Prog Biophys Mol Biol. 2006; 92(1), 17-25.

[152] Foyo-Moreno I, Alados I, Olmo FJ, Alados-Arboledas L. *The influence of cloudiness on UV global irradiance (295–385 nm).* Agric. For. Meteorol. 2003; 120(1-4), 101-111.

[153] McKenzie RL, Björn LO, Bais A, Ilyasd M. *Changes in biologically active ultraviolet radiation reaching the Earth's surface.* Photochem. Photobiol. Sci. 2003; 2(1), 5-15.

[154] Robaa SM. *A study of ultraviolet solar radiation at Cairo urban area, Egypt.* Solar Energy. 2004; 77(2), 251-259.

[155] Parisi AV, Green A, Kimlin MG. *Diffuse solar UV radiation and implications for preventing human eye damage.* Photochem Photobiol. 2001; 73(2), 135-139.

[156] Webb AR. *Changes in stratospheric ozone concentrations and solar UV levels*. Radiat Prot Dosimetry. 1997; 72 (3-4), 207- 216.

[157] Kimlin MG. *The climatology of Vitamin D producing ultraviolet radiation over the United States.* J Steroid Biochem Mol Biol. 2004; 89-90(1-5), 479-483.

[158] Ireland W, Sacher R. *The angular distribution of solar ultraviolet, visible and near-infrared radiation from cloudless skies.* Photochem Photobiol. 1996; 63(4), 483-486.

[159] Gies P, Mackay C. *Measurements of the solar UVR protection provided by shade structures in New Zealand primary schools.* Photochem Photobiol. 2004; 80(2), 334-339.

[160] Oliva M, Taylor H. *Ultraviolet radiation and the eye*. Int Ophthalmol Clin. 2005; 45(1), 1-17.

[161] Roy CR, Gies HP, Lugg DJ, Toomey S, Tomlinson DW. *The measurement of solar ultraviolet radiation.* Mutat Res. 1998; 422(1), 7-14.

[162] Parisi AV, Turnbull DJ, Turner J. *Calculation of cloud modification factors for the horizontal plane eye damaging ultraviolet radiation.* Atmos Res. 2007; 86(3-4), 278-285.

[163] Alados-Arboledas L, Alados I, Foyo-Moreno I, Olmo FJ, Alcantara A. *The influence of clouds on surface UV erythemal irradiance.* Atmos Res. 2003; 66(4), 273-290.

[164] Parisi AV, Turnbull D. *Diffuse solar ultraviolet radiation.* Int Ophthalmol Clin. 2005; 45(1), 19-27.

[165] Nemeth P, Toth Z, Nagy Z. *Effect of weather conditions on UV-B radiation reaching the earth's surface.* J. Photochem. Photobiol., B. 1996; 32(3), 177-181.

[166] Pretor-Pinney G. *The Cloudspotter's Guide*. Hodder and Stoughton, UK, 2007.

[167] Chai AT, Green AES. *Ratio measurement of diffuse to direct solar irradiances in the middle ultraviolet.* Appl. Opt. 1976; 15(5), 1182-1187.

[168] Sabburg JM, Parisi AV, Kimlin MG. *Enhanced spectral UV irradiance: a 1 year preliminary study*. Atmos Res. 2003; 66(4), 261-272.

[169] Calbo J, Gonzalez JA, Pages D. *A method for sky-condition classification from ground-based solar radiation measurements.* J Appl Meteorol. 2001; 40(12), 2193-2199.

[170] Philipona R, Schilling A, Schmucki D, Photochem. Photobiol. *Albedo-enhanced maximum UV irradiance-Measured on surfaces orientated normal to the sun.* 2001; 73(4), 366-369.

[171] Chen D, Wanberg SA, Wulff A, Borne K. *Attenuation of biologically effective UV doses under overcast skies: a case study from the eastern Atlantic sector of the Southern Ocean.* Deep-Sea Research II. 2004; 51(22-24), 2673-2682.

[172] Schwander H, Koepke P, Kaifel A, Seckmeyer G. *Modification of spectral UV irradiance by clouds.* Journal Of Geophysical Research. 2002; 107(D16- 4296), AAC 7-1 – 7-12.

[173] Parisi AV, Downs N. *Cloud cover and horizontal plane eye damaging solar UV exposures.* Int J Biometeorol. 2004; 49(2), 130-136.

[174] Diffey BL. *Solar ultraviolet radiation effects on biological systems*. Phys. Med. Biol. 1991; 36(3), 299-328.

[175] Moise AF, Aynsley R. *Ambient ultraviolet radiation levels in public shade settings*. Int J Biometeorol. Nov 1999; 43(3), 128-138.

[176] Turnbull DJ, Parisi AV. *Increasing the ultraviolet protection factor provided by shade structures*. Photochem Photobiol B. 2005; 78(1), 61-67.

[177] Birt B, Cowling I, Coyne S. *UVR reflections at the surface of the eye*. J Photochem Photobiol B: Biol. 2004; 77(1-3), 71-77.

[178] Pucar M, Despic A. *The effect of diffuse/indirect light on the energy gain of solar thermal collectors.* Renewable Energy. 2005; 30(11), 1749-1758.

[179] Diffey BL. *Ultraviolet radiation and human health.* Clin Dermatol. 1998; 16(1), 83-89.

[180] Engelsen O, Brustad M, Aksnes L, Lund E. *Daily duration of vitamin D synthesis in human skin with relation to latitude, total ozone, altitude, ground cover, aerosols and cloud thickness*. Photochem Photobiol. 2005; 81(6), 1287-1290.

[181] Bodeker GE, McKenzie RL. *An Algorithm for Inferring Surface UV Irradiance Including Cloud Effects.* J Appl Meteorol. 1996; 35(10); 1860-1877.

[182] Pfister G, McKenzie RL, Liley JB, Thomas A, Forgan BW, Long CN. *Cloud Coverage Based on All-Sky Imaging and Its Impact on Surface Solar Irradiance.* J Appl Meteorol. 2003; 42(10), 1421-1434.

[183] Sabburg JM, Parisi AV. *Spectral dependency of cloud enhanced UV irradiance.* Atmos Res. 2006; 81(3), 206-214.

[184] Frederick JE, Erlick C. *The attenuation of sunlight by high-latitude clouds: Spectral Dependence and its physical mechanisms*. J. Atmos. Sci. 1997; 54(24), 2813-2819.

[185] Weihs P. *Influence of ground reflectivity and topography on erythemal UV radiation on inclined planes.* Int J Biometeorol. 2002; 46(2), 95-104.

[186] Kimlin MG, Parisi AV, Wong JC. *The facial distribution of erythemal ultraviolet exposure in south-east Queensland.* Phys Med Biol. 1998; 43(2), 231-240.

[187] Birt B, Cowling I, Coyne S, Michael G. *The effect of the eye's surface topography on the total irradiance of ultraviolet radiation on the inner canthus.* J Photochem Photobiol B. 2007; 87(1), 27-36.

[188] Meyler J, Schnider C. *The role of UV-blocking soft CLs in ocular protection.* Optician. 2002; 5854(223), 28-32.

[189] Sliney DH. *Risks of occupational exposure to optical radiation*. Med Lav 2006; 97(2), 215-220.

[190] Armstrong BK, Kricker A. *How much melanoma is caused by sun exposure?* Melanoma Res. 1993; 3(6), 395-401.

[191] Green AC, Kimlin M, Siskind V, Whiteman DC. *Hypothesis: hair cover can protect against invasive melanoma on the head and neck (Australia).* Cancer Causes Control. 2006; 17(10), 1263-1266.

[192] Meyer N, Pruvost-Balland C, Bourdon-Lanoy E, Maubec E, Avri MF. *Awareness, knowledge and attitudes towards sun protection among skin cancer-treated patients in France.* J Eur Acad Dermatol Venereol. 2007; 21(4), 520-525.

[193] Ferrini RL, Perlman M, Hill L. *American College of Preventive Medicine practice policy statement: skin protection from ultraviolet light exposure. The American College of Preventive Medicine.* Am J Prev Med. 1998; 14(1), 83-86.

[194] Parisi AV, Meldrum LR, Kimlin MG, Wong JC, Aitken J, Mainstone JS. *Evaluation of differences in ultraviolet exposure during weekend and weekday activities.* Phys Med Biol. 2000; 45(8), 2253-2262.

[195] De Gruijl FR. *Skin cancer and solar UV radiation.* Eur J Cancer. 1999; 35(14), 2003-2009.

[196] Monfrecola G, Fabbrocini G, Posteraro G, Pini D. *What do young people think about the dangers of sunbathing, skin cancer and sunbeds? A questionnaire survey among Italians.* Photodermatol Photoimmunol Photomed. 2000; 16(1), 15-18.

[197] Miles A, Waller J, Hiom S, Swanston D. *SunSmart? Skin cancer knowledge and preventive behaviour in a British population representative sample.* Health Educ Res. 2005; 20(5), 579-585.

[198] Fu JM, Dusza SW, Halpern AC. *Sunless tanning.* J Am Acad Dermatol. 2004; 50(5), 706-713.

[199] Hiom S. *Public awareness regarding UV risks and vitamin D--the challenges for UK skin cancer prevention campaigns.* Prog Biophys Mol Biol. 2006; 92(1), 161-166.

[200] Koh HK, Geller AC. *Skin cancer prevention comes of age.* Am J Prev Med. 2004; 27(5), 484-485.

[201] Gazzard G, Saw -M, Farook M, Koh D, Widjaja D, Chia SE, Hong C-Y, Tan DTH. *Pterygium in Indonesia: prevalence, severity and risk factors.* Br J Ophthalmol. 2002; 86(12), 1341-1346.

[202] Newton R, Ferlay J, Reeves G, Beral V, Parkin DM. *Effect of ambient solar ultraviolet radiation on incidence of squamous-cell carcinoma of the eye.* Lancet. 1996; 347(9013), 1450-1451.

[203] Sproul AB. *Derivation of the solar geometric relationships using vector analysis.* Renewable Energy. 2007; 32(7), 1187-1205.

[204] Kimlin MG, Martinez N, Green AC, Whiteman DC. *Anatomical distribution of solar ultraviolet exposures among cyclists.* J Photochem Photobiol B. 2006; 85(1), 23-27.

[205] Panchapakesan J, Hourihan F, Mitchell P. *Prevalence of pterygium and pinguecula: the Blue Mountains Eye Study.* Aust N Z J Ophthalmol. 1998; 26(Suppl 1), 2-5.

[206] Carter OBJ, Donovan RJ. *Public (Mis)understanding of the UV Index.* J Health Commun. 2007; 12(1), 41-52.

[207] Ramsay HM, Fryer AA, Hawley CM, Smith AG, Nicol DL, Harden PN. *Factors associated with nonmelanoma skin cancer following renal transplantation in Queensland, Australia.* J Am Acad Dermatol. 2003; 49(3), 397-406.

[208] Repacholi MH. *Global solar UV index*. Radiat Prot Dosimetry. 2000; 91(1-3), 307-311.

[209] Gies PH, Roy CR, Toomey S, McLennan A. *Protection against solar ultraviolet radiation.* Mutat Res. 1998; 422(1), 15-22.

[210] Gies PH. *Australia has more than enough solar UV radiation.* Clin Exp Optom. 2003; 86(2), 71-73.

[211] Abarca JF, Casiccia CC. *Skin cancer and ultraviolet-B radiation under the Antarctic ozone hole: southern Chile, 1987-2000.* Photodermatol Photoimmunol Photomed. 2002; 18(6), 294-302.

[212] Diffey BL. *Human exposure to solar ultraviolet radiation.* J Cosmet Dermatol. 2002; 1(3), 124-130.

[213] Johnson GJ. *The environment and the eye.* Eye. 2004; 18(12), 1235-1250.

[214] Stick C, Harms V, Pielke L. *Measurements of solar ultraviolet irradiance with respect to the human body surface.* SPIE Proc. (Ultraviolet Radiation Hazards). 1994; 2134B, 129-134.

[215] World Health Organisation (WHO). *Protection against exposure to ultraviolet radiation*. WHO/EHG/95.17, Geneva 1995.

[216] Natl Inst Health Consens Dev Conf Consens Statement. *Sunlight, ultraviolet radiation, and the skin.* 1989; 7(8), 1-10.

[217] Rigel EG, Lebwohl MG, Rigel AC, Rigel DS. *Ultraviolet radiation in alpine skiing: magnitude of exposure and importance of regular protection.* Arch Dermatol. 2003; 139(1), 60-62.

[218] Sliney DH. *Physical factors in cataractogenesis: ambient ultraviolet radiation and temperature.* Invest Ophthalmol Vis Sci. 1986; 27(5), 781-790.

[219] Dolin PJ. *Methodological considerations for future epidemiological studies of solar ultraviolet radiation and eye disease.* Ophthalmic Epidemiol. 1994; 1(3), 165-170.

[220] Reuder J, Ghezzi F, Palenque E, Torrez R, Andrade M, Zaratti F. *Investigations on the effect of high surface albedo on erythemally effective UV irradiance: Results of a campaign at the Salar de Uyuni, Bolivia.* J Photochem Photobiol B. 2007; 87(1), 1-8.

[221] Lester RA, Parisi AV. *Spectral ultraviolet albedo of roofing surfaces and human facial exposure*. Int. J Environ Health Res. 2002; 12(1), 75-81.

[222] Lenoble J. *Influence of the Environment Reflectance on the Ultraviolet Zenith Radiance for Cloudless Sky.* Appl. Opt. 2000; 39(24), 4247-4254.

[223] Sliney DH. *Ultraviolet radiation effects upon the eye: problems of dosimetry*. Radiat Prot Dosimetry. 1997; 72(3-4), 197-206.

[224] Young AR. *Acute effects of UVR on human eyes and skin.* Prog. Biophys. Mol. Biol. 2006; 92(1), 80-85.

[225] Zuclich JA. *Ultraviolet-induced photochemical damage in ocular tissues*. Health Phys. 1989; 56(5), 671-682.

[226] Sliney DH. *Eye protective techniques for bright light*. Ophthalmology. 1983; 90(8), 937-944.

[227] Roberts JE. *Ocular phototoxicity*. J Photochem Photobiol B 2001; 64(2-3), 136-143.

[228] Doughty MJ, Oblak E. *A clinical assessment of the anterior eye in arc welders.* Clin Exp Optom. 2005; 88(6), 387-395.

[229] Dixon AJ, Dixon BF. *Ultraviolet radiation from welding and possible risk of skin and ocular malignancy.* MJA. 2004; 181(3), 155-157.

[230] World Health Organisation (WHO). *Global disease burden from solar ultraviolet radiation*. July 2006, Fact sheet No 305.

[231] Diffey BL. *Ultraviolet radiation physics and the skin.* Phys. Med. Biol. 1980; 25(3), 405-426.

[232] Madronich S, McKenzie RL, Björn LO, Caldwell LL. *Changes in biologically active ultraviolet radiation reaching the Earth's surface.* J. Photochem. Photobiol., B. 1998; 46(1-3), 5-19.

[233] Tenkate TD. *Ultraviolet Radiation: Human exposure and health risks.* J. Environ. Health. 1998; 61(2), 9-15.

[234] de Gruijl FR. *Biological Action Spectra.* Radiat Prot Dosimetry. 2000: 91(1-3), 57-63.

[235] Aucamp PJ. *Questions and answers about the effects of the depletion of the ozone layer on humans and the environment.* Photochem Photobiol Sci. 2007; 6(3), 319-330.

[236] Lucas RM, Repacholi MH, McMichael AJ. *Is the current public health message on UV exposure correct?* Bull. World Health Organ, 2006; 84(6), 485-491.

[237] Di Menno I, Moriconi ML, Di Menno M, Casale GR, Siani AM. *Spectral ultraviolet measurements by a multichannel monitor and a brewer spectroradiometer: a field study.* Radiat Prot Dosimetry. 2002; 102(3), 259-263.

[238] de la Torre R, Horneck G, Rettberg P, Luccini E, Vilaplana JM, Gil M. *Monitoring of biologically effective UV irradiance at El Arenosillo (INTA), Andalucia, in Spain.* Adv Space Res. 2000; 26(12), 2015-2019.

[239] Diamond SA, Trenham PC, Adams MJ, Hossack BR, Knapp RA, Stark SL, Bradford D, Corn PS, Czarnowski K, Brooks PD, Fagre D, Breen B, Detenbeck NE, Tonnessen K. *Estimated ultraviolet radiation doses in wetlands in six national parks.* Ecosystems. 2005; 8(5), 462-477.

[240] Fris M, Tessem MB, Cejkova J, Midelfart A. *The effect of single and repeated UVB radiation on rabbit cornea.* Graefes Arch Clin Exp Ophthalmol. 2006; 244, 1680-1687.

[241] West SK, Longstreth JD, Munoz BE, Pitcher HM, Duncan DD. *Model of risk of cortical cataract in the US population with exposure to increased ultraviolet radiation due to stratospheric ozone depletion.* Am J Epidemiol. 2005; 162(11), 1080-1088.

[242] Driscoll CMH. *Solar UVR measurements.* Radiat Prot Dosimetry. 1996; 64(3), 179-188.

[243] Coldiron BM. *The UV index: a weather report for skin.* Clin Dermatol. 1998; 16(4), 441-446.
[244] Parisi AV, Sabburg J, Kimlin, Downs N. *Measured and modelled contributions to UV exposures by the albedo of surfaces in an urban environment.* Theor. Appl. Climatol. 2003; 76 (3-4), 181-188.

[245] Sliney DH. *Dosimetry for ultraviolet radiation exposure of the eye.* SPIE Proc. (Ultraviolet Radiation Hazards). 1994; 2134B, 2-12.

[246] Grifoni D, Carreras G, Sabatini F, Zipoli G. *UV hazard on a summer's day under Mediterranean conditions, and the protective role of a beach umbrella.* Int J Biometeorol. 2005; 50(2), 75-82.

[247] Sliney DH, World Health Organisation (WHO). *Ultraviolet radiation ocular exposure dosimetry of the eye.* WHO/EHG/95.18, Geneva 1995.

[248] Sliney DH. *Biohazards of ultraviolet, visible and infrared radiation.* J Occup Med. 1983; 25(3), 203-210.

[249] Sliney DH. *Spectral transmission of IOLs expressed as a virtual age.* Br J Ophthalmol. 2007; 91(10), 1261-1262.

[250] Young S, Sands J. *Sun and the eye: prevention and detection of light-induced disease*. Clin Dermatol. 1998; 16(4), 477-485.

[251] Kwok LS, Coroneo MT. *A model for pterygium formation*. Cornea. 1994; 13(3), 219-224.

[252] Kinoshita S, Adachi W, Sotozono C, Nishida K, Yokoi N, Quantock AJ, Okubo K. *Characteristics of the human ocular surface epithelium.* Prog Retin Eye Res. 2001; 20(5), 639-673.

[253] Dushku N, John MK, Schultz GS, Reid TW. *Pterygia pathogenesis: corneal invasion by matrix metalloproteinase expressing altered limbal epithelial basal cells.* Arch Ophthalmol. 2001; 119(5), 695-706.

[254] Seifert P, Sekundo W. *Capillaries in the epithelium of pterygium.* Br J Ophthalmol. 1998; 82(1), 77-81.

[255] Fritz MH. *Blindness from multiple pterygiums in an Alaskan native*. Am J Ophthalmol. 1955; 39(4, Part 1), 572.

[256] Taylor HR. *Pterygium leading to blindness: a case report*. Aust J Ophthalmol 1978; 6(3), 155-156.

[257] Wlodarczyk J, Whyte P, Cockrum P, Taylor H. *Pterygium in Australia: a cost of illness study.* Clin Exp Ophthalmol. 2001; 29, 370-375.

[258] Lee AJ, Lee J, Saw SM, Gazzard G, Koh D, Widjaja, Tan DTH. *Prevalence and risk factors associated with dry eye symptoms: a population based study in Indonesia.* Br J Ophthalmol. 2002; 86(12), 1347-1351.

[259] http://web.princeton.edu/sites/ehs/laserguide/sec2.htm
(Accessed 18 April 2008)

[260] Chan CM, Liu YP, Tan DT. *Ocular surface changes in pterygium.* Cornea. 2002; 21(1), 38-42.

[261] Courville CB, Smolek MK, Klyce SD. *Contribution of the ocular surface to visual optics*. Exp Eye Res. 2004; 78(3), 417-425.

[262] Kaye GWC. Laby TH. Tables of Physical and Chemical Constants and some Mathematical Functions, 14th edition, NY, USA, 1973.

[263] Lam AKC, Douthwaite WA. *The ageing effect on the central posterior corneal radius.* Ophthal. Physiol. Opt. 2000; 20(1), 63-69.

[264] Hughes MO. *Anatomy of the anterior eye for ocularists.* J of Ophthalmic Prosthetics. 2004; 8(1), 25-35.

[265] Saude T. Ocular Anatomy and Physiology. (Translated by Fletcher R.). Blackwell Science Ltd, UK, reprinted 2000.

[266] Cocks GG. *An instrument for measuring the contour of the cornea.* Appl. Opt. 1968; 7(1), 151-154.

[267] Jenkins FA, White HE. Fundamentals of Optics, Fourth Edition. McGraw-Hill Book Company, Singapore, 1981.

[268] Liou H-L, Brennan NA. *Anatomically accurate, finite model eye for optical modeling.* J Opt Soc Am A. 1997; 14(8), 1684-1695.

[269] Mutti DO, Hayes JR, Mitchell GL, Jones LA, Moeschberger ML, Cotter SA, Kleinstein RN, Manny RE, Twelker JD, Zadnik K; CLEERE Study Group. *Refractive error, axial length, and relative peripheral refractive error before and after the onset of myopia.* Invest Ophthalmol Vis Sci. 2007; 48(6), 2510-2519.

[270] Remington LE. Clinical Anatomy of the Visual System. Butterworth-Heinemann, MA, USA, 1999.

[271] Zhivov A, Stachs O, Kraak R, Stave J, Guthoff RF. *In vivo confocal microscopy of the ocular surface.* The Ocular Surface. 2006; 4(2), 81-93.

[272] Nichols B, Dawson CR, Togni B. *Surface features of the conjunctiva and cornea.* Invest Ophthalmol Vis Sci. 1983; 24(5), 570-576.

[273] Dua HS. *The conjunctiva in corneal epithelial wound healing.* Br J Ophthalmol. 1998; 82(12), 1407-1411.

[274] Li W, Hayashida Y, Chen YT, Tseng SC. *Niche regulation of corneal epithelial stem cells at the limbus.* Cell Res. 2007; 17(1), 26-36.

[275] Kim YL, Walsh JT Jr, Goldstick TK, Glucksberg MR. *Variation of corneal refractive index with hydration.* Phys Med Biol. 2004; 49(5), 859-868.

[276] McCally RL, Freund DE, Zorn A, Bonney-Ray J, Grebe R, de la Cruz Z, Green WR. *Light-scattering and ultrastructure of healed penetrating corneal wounds* .Invest Ophthalmol Vis Sci. 2007; 48(1), 157-165.

[277] Bourne WM. *Biology of the corneal endothelium in health and disease.* Eye. 2003; 17(8), 912-918.

[278] Lens A, Langley T, Coyne Nemeth S, Shea C. Ocular Anatomy and Physiology, The Basic Bookshelf for Eyecare Professionals. SLACK Inc. NJ, USA, 1999.

[279] Risse Marsh BC, Massaro-Giordano M, Marshall CM, Lavker RM, Jensen PJ. *Initiation and characterization of keratinocyte cultures from biopsies of normal human conjunctiva.* Exp Eye Res. 2002; 74(1), 61-69.

[280] Cullen AP, Perera SC. *Sunlight and human conjunctival action spectrum*. SPIE Proc. (Ultraviolet Radiation Hazards). 1994; 2134B, 24-30.

[281] Cullen AP. *Photokeratitis and other phototoxic effects on the cornea and conjunctiva.* Int J Toxicol. 2002; 21(6), 455-464.

[282] Stapleton F, Stretton S, Papas E, Skotnitsky C, Sweeney DF. *Silicone hydrogel contact lenses and the ocular surface.* Ocul. Surf. 2006; 4 (1), 24-43.

[283] Ang LPK, Tan DTH. *Ocular surface stem cells and disease: Current Concepts and Clinical Applications.* Ann Acad Med Singapore. 2004; 33(5), 576-580.

[284] Efron N. The Cornea: Its examination in contact lens practice. Oxford: Butterworth-Heinemann, 2001.

[285] Sangwan VS. *Limbal stem cells in health and disease.* Biosci Rep. 2001; 21(4), 385-405.

[286] Schlotzer-Schrehardt U, Kruse FE. *Identification and characterization of limbal stem cells.* Exp Eye Res. 2005; 81(3), 247-264.

[287] Lavker RM, Tseng SC, Sun TT. *Corneal epithelial stem cells at the limbus: looking at some old problems from a new angle.* Exp Eye Res. 2004; 78(3), 433-446.

[288] Lavker RM, Sun TT. *Epithelial stem cells: the eye provides a vision.* Eye. 2003; 17(8), 937-942.

[289] Charukamnoetkanok P. *Corneal stem cells: bridging the knowledge gap.* Semin Ophthalmol. 2006; 21(1), 1-7.

[290] Pajoohesh-Ganji A, Stepp MA. *In search of markers for the stem cells of the corneal epithelium.* Biol Cell. 2005; 97(4), 265-276.

[291] Remington SG, Meyer RA. *Lens stem cells may reside outside the lens capsule: an hypothesis.* Theor Biol Med Model. 2007; 4(1), 22 (Page number not for citation purposes).

[292] Schlotzer-Schrehardt U, Dietrich T, Saito K, Sorokin L, Sasaki T, Paulsson M, Kruse FE. *Characterization of extracellular matrix components in the limbal epithelial stem cell compartment.* Exp Eye Res. 2007; 85(6), 845-860.

[293] Coroneo MT. *The ophthalmohelioses and peripheral light focusing by the anterior eye.* SPIE Proc. (Ultraviolet Radiation Hazards). 1994; 2134B, 31-36.

[294] Ooi JL, Sharma NS, Sharma S, Papalkar D, Oakey M, Dawes P, Coroneo MT. *Ultraviolet fluorescence photography: patterns in established pterygia.* Am J Ophthalmol. 2007; 143(1), 97-101.

[295] Fatt I, Weissman BA. Physiology of the Eye, An Introduction to the vegetative functions, 2nd Ed. Butterworth-Heinneman, MA, USA, 1992.

[296] Remington LA. Clinical Anatomy of the Visual System. Butterworth-Heinemann, USA, 1998.

[297] Sliney DH, Wolbarsht ML. *Future applications of lasers in surgery and medicine: a review.* J R Soc Med. 1989; 82(5): 293–296.

[298] Soderberg PG, Michael R, Merriam JC. *Maximum acceptable dose of ultraviolet radiation: a safety limit for cataract.* Acta Ophthalmol. Scand. 2003; 81(2), 165-169.

[299] Thylefors B, Chylack LT Jr, Konyama K, Sasaki K, Sperduto R, Taylor HR, West S; WHO Cataract Grading Group. *A simplified cataract grading system.* Ophthalmic Epidemiol. 2002; 9(2), 83-95.

[300] Asbell PA, Dualan I, Mindel J, Brocks D, Ahmad M, Epstein S. *Age-related cataract.* Lancet. 2005; 365 (9459), 599-609.

[301] Sliney DH, Fast P, Ricksand A. *Optical radiation hazards analysis of ultraviolet headlamps.* Appl. Opt. 1995; 34(22), 4912-4922.

[302] Sliney DH, Armstrong BC. *Radiometric evaluation of surgical microscope lights for hazards analyses.* Appl. Opt. 1986; 25(12), 1882-1889.

[303] Pitts DG, Cullen AP, Hacker PD. *Ocular effects of ultraviolet radiation from 295 to 365 nm.* Invest Ophthalmol Vis Sci. 1977; 16(10), 932-939.

[304] Smith BT, Belani S, Ho AC. *Ultraviolet and near-blue light effects on the eye.* Int Ophthalmol Clin. 2005; 45(1), 107-115.

[305] Swerdlow AJ. *Epidemiology of chronic disease risks in relation to ultraviolet radiation exposure.* Radiat Prot Dosimetry. 2000; 91(1-3), 19-23.

[306] West SK, Duncan DD, Munoz B, Rubin GS, Fried LP, Bandeen-Roche K, Schein OD. *Sunlight exposure and risk of lens opacities in a population-based study: the Salisbury Eye Evaluation project.* JAMA. 1998; 280(8), 714-718.

[307] Michael R, Wegener A. *Estimation of safe exposure time from an ophthalmic operating microscope with regard to ultraviolet radiation and blue-light hazards to the eye.* J Opt Soc Am A Opt Image Sci Vis. 2004; 21(8), 1388-1392.

[308] Lakkis C, Weidemann K. *Evaluation of the performance of photochromic spectacle lenses in children and adolescents aged 10 to 15 years.* Clin Exp Optom. 2006; 89(4), 246-252.

[309] Zuchlich J. *In vivo measurements of optical properties of the ocular lens.* SPIE Proc. (Ultraviolet Radiation Hazards). 1994; 2134B, 99-112.

[310] Taylor HR, Muñoz B, West S, Bressler NM, Bressler SB, Rosenthal FS. *Visible light and risk of age-related macular degeneration.* Trans Am Ophthalmol Soc. 1990; 88: 163–178.

[311] Mainster MA. *Violet and blue light blocking intraocular lenses: photoprotection versus photoreception.* Br J Ophthalmol. 2006; 90(6), 784-792.

[312] Shah CP, Weis E, Lajous M, Shields JA, Shields CL. *Intermittent and chronic ultraviolet light exposure and uveal melanoma: a meta-analysis.* Ophthalmology. 2005; 112(9), 1599-1607.

[313] Singh AD, Rennie IG, Seregard S, Giblin M, McKenzie J. *Sunlight exposure and pathogenesis of uveal melanoma.* Surv Ophthalmol. 2004; 49(4), 419-428.

[314] Longstreth J, de Gruijl FR, Kripke ML, Abseck S, Arnold F, Slaper HI, Velders G, Takizawa Y, van der Leun JC. *Health risks.* J Photochem Photobiol B. 1998; 46(1-3), 20-39.

[315] van Norren D, van de Kraats J. *Spectral transmission of intraocular lenses expressed as a virtual age.* Br J Ophthalmol. 2007; 91(10), 1374-1375.

[316] Delori FC, Webb RH, Sliney DH. *Maximum permissible exposures for ocular safety (ANSI 2000), with emphasis on ophthalmic devices.* J Opt Soc Am A Opt Image Sci Vis. 2007; 24(5), 1250-1265.

[317] van de Kraats J, van Norren D. *Optical density of the aging human ocular media in the visible and the UV.* J Opt Soc Am A Opt Image Sci Vis. 2007; 24(7), 1842-1857.

[318] Oyster CW. The Human Eye: Structure and Function. Sinauer Associates, Inc. Massachusetts, USA, 1999.

[319] Wittenberg S. *Solar Radiation and the eye – A review of knowledge relevant to eye care.* Am J Optom Physiol Opt. 1986; 63(8), 676-689.

[320] Coroneo MT, *Albedo concentration in the anterior eye: a phenomenon that locates some solar diseases.* Opthalmic Surg. 1990; 21(1), 60-66.

[321] Ooi JL, Sharma NS, Papalkar D, Sharma S, Oakey M, Dawes P, Coroneo MT. *Ultraviolet fluorescence photography to detect early sun damage in the eyes of school-aged children.* Am J Ophthalmol. 2006; 141(2), 294-298.

[322] Coroneo MT, Muller-Stolzenburg NW, Ho A. *Peripheral light focusing by the anterior eye and the ophthalmohelioses.* Ophthalmic Surg. 1991; 22(12), 705-711.

[323] Maloof AJ, Ho A, Coroneo MT. *Influence of corneal shape on limbal light focusing.* Invest Ophthalmol Vis Sci. 1994; 35(5), 2592-2598.

[324] Maloof AJ, Ho A, Coroneo MT. *Peripheral light focusing by the anterior segment.* SPIE Proc. (Ultraviolet Radiation Hazards). 1994; 2134B, 37-42.

[325] Narayanan P, Merriam JC, Vazquez ME, Dillon J. *Experimental model of light focusing of the peripheral cornea.* Invest Ophthalmol Vis Sci. 1996; 37(1), 37-41.

[326] Merriam JC. *The concentration of light in the human lens.* Trans Am Ophthalmol Soc. 1996; 94, 803-918.

[327] Cullen AP, Oriowo OM, Viosin AC. *Anterior eye focusing of peripheral ultraviolet and visible radiation albedo.* Clin Exp Optom. 1997; 80(3), 80-86.

[328] Kwok LS, Kuznetsov VA, Ho A, Coroneo MT. *Prevention of the adverse photic effects of peripheral light-focusing using UV-blocking contact lenses.* Invest Ophthalmol Vis Sci. 2003; 44(4), 1501-1507.

[329] Blue R, Uttamchandani D, Wilson CG. *Optical system for drug detection in the anterior chamber of the eye*. IEE Colloq. Biomedical Applications of Photonics, Savoy Place, London (April 1997)

[330] Blue R, Uttamchandani D, Wilson CG. *Minimally invasive optoelectronic sensing technique for chemical analysis of aqueous humor*. IEE Proc.: Sci., Meas. Technol. 1999; 146(1), 41-46.

[331] Miller J, Wilson CG, Uttamchandani D. *Minimally invasive spectroscopic system for intraocular drug detection*. J. Biomed. Opt. 2002; 7(1), 27-33.

[332] Miller J, Wilson WS, Kek WK, Wilson CG, Uttamchandani D. *Drug detection in the living eye using a novel, minimally invasive optoelectronic system*. IEEE Sensors Journal. 2003; 3(1), 95-101.

[333] Miller J, Wilson WS, Kek WK, Wilson CG, Uttamchandani D. *Spectroscopic detection of a therapeutic drug in the mammalian eye*. IEEE J. Sel. Top. Quantum Electron. 2003; 9(2), 171-176.

[334] Miller J, Wilson WS, Wilson CG, Uttamchandani D. Minimally invasive, direct, real time measurement of drug concentration in the anterior eye. Br. J. Ophthalmol. 2005; 89(9), 1147-1151.

[335] Twelker JD, Harbison SC, Bailey IL. *Peripheral light-focusing: measurement reliability and correlations with ocular dimensions.* Optom Vis Sci. 2005; 82(2), 94-100.

[336] Jaros PA, DeLuise VP. *Pingueculae and Pterygia*. Surv Ophthalmol. 1988; 33(1), 41-49.

[337] Threlfall TJ, English DR. *Sun exposure and pterygium of the eye: a dose-response curve.* Am J Ophthalmol. 1999; 128(3), 280-287.

[338] Cameron ME. Pterygium throughout the world. Springfield, Ill: Charles C Thomas 1965.

[339] Saw SM, Tan D. *Pterygium: prevalence, demography and risk factors*. Ophthalmic Epidemiol. 1999; 6(3), 219-228.

[340] Young AL, Leung GYS, Wong AKK, Cheng LL, Lam DSC. *A randomised trial comparing 0.02% mitomycin C and limbal conjunctival autograft after excision of primary pterygium*. Br J Ophthalmol. 2004; 88(8), 995-997.

[341] Wong TY, Foster PJ, Johnson GJ, Seah SKL, Tan DTH. The prevalence and risk factors for pterygium in an adult Chinese population in Singapore: The Tanjong Pagar survey. Am. J. Ophthalmol. 2001; 131(2), 176-183.

[342] Peiretti E, Dessi S, Mulas C, Abete C, Norfo C, Putzolu M, Fossarello M. *Modulation of cholesterol homeostasis by antiproliferative drugs in human pterygium fibroblasts.* Invest Ophthalmol Vis Sci. 2007; 48(8), 3450-3458.

[343] Lee JK, Kim JC. *Progenitor Cells in Healing after Pterygium Excision.* Yonsei Med J 2007; 48(1), 48-54.

[344] Roberts JE. *Screening for ocular phototoxicity.* Int. J. Toxicol. 2002; 21(6),491-500.

[345] Gies P, Roy CR. *Ocular protection from ultraviolet radiation.* Clin Exp Optom. 1988; 71(1), 21-27.

[346] Zigman S. *Environmental near-UV radiation and cataracts.* Optom Vis Sci. 1995; 72(12), 899-901.

[347] Sliney DH. *How light reaches the eye and its components*. Int. J. Toxicol. 2002; 21(6), 501-509.

[348] Giasson CJ, Quesnel NM, Boisjoly H. *The ABC's of ultraviolet –blocking contact lenses. An ocular panacea for ozone loss?* Int Ophthalmol Clin. 2005; 45(1), 117-139.

[349] Najjar DM, Awwad ST, Zein WM, Haddad WF. *Assessment of the corneal endothelium in acute ultraviolet keratitis.* Med Sci Monit. 2006; 12(5), MT23-5.

[350] Cullen AP. *UV radiation: Contact lenses and the ophthalmohelioses.* Optometry Today. 2005; June 17, 30-34. http://www.optometry.co.uk/articles2005.php
(Accessed 18 April 2008)

[351] Pitts DG. *The human ultraviolet action spectrum*. Am. J. Optom. Physiol. Opt. 1974; 51(12), 946-960.

[352] Kolozsvári L, Nógrádi A, Hopp B, Bor Z. *UV absorbance of the human cornea in the 240- to 400- nm range*. Invest Ophthalmol Vis Sci. 2002; 43(7), 2165-2168.

[353] Radiation Health Handbook. © 1993 National Radiation Laboratory, Ministry of Health, Christchurch, NZ.

[354] Okuno T, Ojima J, Saito H. *Ultraviolet radiation emitted by CO_2 arc welding.* Ann. Occup. Hyg. 2001; 45(7), 597-601.

[355] Karai I, Horiguchi S. *Pterygium in welders.*Br J Ophthalmol. 1984; 68(5), 347-349.

[356] Oliver H, Moseley H, Ferguson J, Forsyth A. *Clustered outbreak of skin and eye complaints among catering staff.* Occup Med (Lond). 2005; 55(2), 149-153.

[357] MacDonald PD, Langley RL, Howell RJ. *Erythema and conjunctivitis: investigation of an outbreak in a school gymnasium caused by unintentional exposure to ultraviolet radiation from metal halide lamps.* J Occup Environ Hyg. 2007; 4(5), D46-49.

[358] Coster D. Pterygium – an ophthalmic enigma. Br. J. Ophthalmol. 1995; 79(4), 304-305.

[359] Di Girolamo N, Tedla N, Kumar RK, McCluskey P, Lloyd A, Coroneo MT, Wakefield D. *Culture and characterisation of epithelial cells from human pterygia.* Br J Ophthalmol. 1999; 83(9), 1077-1082.

[360] Solomon AS. *Pterygium.* Br J Ophthalmol. 2006; 90(6), 665-666.

[361] Chan CM, Chew PT, Alsagoff Z, Wong JS, Tan DT. Vascular patterns in pterygium and conjunctival autografting: a pilot study using indocyanine green anterior segment angiography. Br J Ophthalmol. 2001; 85(3), 350-353.

[362] Lindsay RG, Sullivan L. *Pterygium-induced corneal astigmatism.* Clin Exp Optom. 2001; 84(4), 200-203.

[363] Song YS, Ryu YH, Choi SR, Kim JC. *The involvement of adult stem cells originated from bone marrow in the pathogenesis of pterygia.* Yonsei Med J. 2005; 46(5), 687-692.

[364] Frau E, Labetoulle M, Lautier-Frau M, Hutchinson S, Offret H. *Corneo-conjunctival autograft transplantation for pterygium surgery.* Acta Ophthalmol. Scand. 2004; 82(1), 59-63.

[365] Tomidokoro A, Miyata K, Sakaguchi Y, Samejima T, Tokunaga T, Oshika T. *Effects of pterygium on corneal spherical power and astigmatism.* Ophthalmology. 2000; 107(8), 1568-1571.

[366] Read SA, Collins MJ, Carney LG. *A review of astigmatism and its possible genesis.* Clin Exp Optom. 2007; 90(1), 5-19.

[367] Zhang M, Bian F, Wen C, Hao N. *Inhibitory effect of curcumin on proliferation of human pterygium fibroblasts.* J Huazhong Univ Sci Technolog Med Sci. 2007; 27(3), 339-342.

[368] Ibechukwu BI. *Simultaneous pterygium and intraocular surgery.* Br J Ophthalmol. 1990; 74(5), 265-266.

[369] Touhami A, Di Pascuale MA, Kawatika T, Del Valle M, Rosa RH Jr, Dubovy S, Tseng SC. *Characterisation of myofibroblasts in fibrovascular tissues of primary and recurrent pterygia.* Br J Ophthalmol. 2005; 89(3), 269-274.

[370] Maheshwari S. *Pterygium-induced corneal refractive changes.* Indian J Ophthalmol. 2007; 55(5), 383-386.

[371] Peiretti E, Dessi S, Mulas MF, Abete C, Galantuomo MS, Fossarello M. *Fibroblasts isolated from human pterygia exhibit altered lipid metabolism characteristics.* Exp Eye Res. 2006; 83(3), 536-542.

[372] Nolan TM, DiGirolamo N, Sachdev NH, Hampartzoumian T, Coroneo MT, Wakefield D. *The role of ultraviolet irradiation and heparin-binding epidermal growth factor-like growth factor in the pathogenesis of pterygium*. Am J Pathol. 2003; 162(2), 567-574.

[373] Pang Y, Rose T. *Rapid growth of pterygium after photorefractive keratectomy*. Optometry. 2006; 77(10), 499-502.

[374] Reid TW. Dushku N. *Pterygia and limbal epithelial cells: Relationship and molecular mechanisms.* Prog. Retin. Eye Res. 1996; 15(2), 297-329.

[375] Di Girolamo N, Kumar RK, Coroneo MT, Wakefield D. *UVB-mediated induction of interleukin-6 and -8 in pterygia and cultured human pterygium epithelial cells.* Invest Ophthalmol Vis Sci. 2002; 43(11), 3430-3437.

[376] Taylor HR. Pterygium (Ch. 3 DH Sliney). Kugler Publications, The Hague, The Netherlands. 2000.

[377] McCarty CA, Fu CL, Taylor HR. *Epidemiology of pterygium in Victoria, Australia.* Br J Ophthalmol. 2000; 84(3), 289-292.

[378] Di Girolamo N, Wakefield D, Coroneo MT. *UVB-mediated induction of cytokines and growth factors in pterygium epithelial cells involves cell surface receptors and intracellular signaling.* Invest Ophthalmol Vis Sci. 2006; 47(6), 2430-2437.

[379] Khoo J, Saw SM, Banerjee K, Chia SE, Tan D. *Outdoor work and the risk of pterygia: a case-control study.* Int Ophthalmol. 1998; 22(5), 293-298.

[380] Chui J, Di Girolamo N, Coroneo MT, Wakefield D. *The role of substance p in the pathogenesis of pterygia.* Invest Ophthalmol Vis Sci. 2007; 48(10), 4482-4489.

[381] Yan QC, Wang XL, Bai QH, Wang W, Gao Q, Zhang JS, Liu Y, Liu R. *Relationship between the morbidity of pterygium and the duration of ultraviolet rays exposure in Sanya, China.* Chin Med J (Engl). 2006; 119(15), 1308-1310.

[382] Armstrong BK, Kricker A. *The epidemiology of UV induced skin cancer.* J Photochem Photobiol B. 2001; 63(1-3), 8-18.

[383] Hirst LW, Sebban A, Chant D. *Pterygium recurrence time.* Ophthalmology. 1994; 101(4), 755-758.

[384] Hirst LW. *The Treatment of Pterygium*. Surv. Ophthalmol. 2003; 48(2), 145-180.

[385] Karukonda SR, Thompson HW, Beuerman RW, Lam DS, Wilson R, Chew SJ, Steinemann TL. *Cell cycle kinetics in pterygium at three latitudes.* Br J Ophthalmol 1995; 79(4), 313-317.

[386] Tayanc E, Akova Y, Yilmaz G, Aydin P. *Anterior segment indocyanine green angiography in pterygium surgery with conjunctival autograft transplantation.* Am J Ophthalmol. 2003; 135(1), 71-75.

[387] Zhang F, Löfgren S, Söderberg PG. *Interaction of anaesthetic drugs and UV-B irradiation in the anterior segment of the rat eye.* Acta Ophthalmol Scand. 2007; 85(7), 745-752.

[388] Mukesh BN, Le A, Dimitrov PN, Ahmed S, Taylor HR, McCarty CA. *Development of cataract and associated risk factors: the Visual Impairment Project.* Arch Ophthalmol. 2006; 124(1), 79-85.

[389] McCarty CA, Taylor HR. *Recent developments in vision research: light damage in cataract.* Invest Ophthalmol Vis Sci. 1996; 37(9), 1720-1723.

[390] Toh T, Morton J, Coxon J, Elder MJ. *Medical treatment of cataract.* Clin Experiment Ophthalmol. 2007; 35(7), 664-671.

[391] Rochtchina E, Mitchell P, Coroneo M, Wang JJ, Cumming RG. *Lower nasal distribution of cortical cataract: the Blue Mountains Eye Study.* Clin Experiment Ophthalmol. 2001; 29(3), 111-115.

[392] Sasaki H, Kawakami Y, Ono M, Jonasson F, Shui YB, Cheng HM, Robman L, McCarty C, Chew SJ, Sasaki K. *Localization of cortical cataract in subjects of diverse races and latitude.* Invest Ophthalmol Vis Sci. 2003; 44(10), 4210-4214.

[393] Kwok LS, Coroneo MT. *Temporal and spatial growth patterns in the normal and cataractous human lens*. Exp. Eye Res. 2000; 71(3), 317-322.

[394] Taylor HR, West SK, Rosenthal FS, Munoz B, Newland HS, Abbey H, Emmett EA. *Effect of ultraviolet radiation on cataract formation.* N Engl J Med. 1988; 319(22), 1429-1433.

[395] Belkin M. *Ultraviolet eye damage: The epidemiological evidence.* SPIE Proc. (Ultraviolet Radiation Hazards). 1994; 2134B, 13-18.

[396] Harvey B. *UV and eye protection.* Optician. 2006; 232(6068), 17-24.

[397] Loeffler KU, Sastry SM, McLean IW. *Is age-related macular degeneration associated with pinguecula or scleral plaque formation?* Curr Eye Res. 2001; 23(1), 33-37.

[398] Bergmanson JPG, Soderberg PG. *The significance of ultraviolet radiation for eye diseases. A review with comments on the efficacy of UV-blocking contact lenses.* Ophthalmic Physiol Opt. 1995; 15(2), 83-91.

[399] Hoover HL. *Solar ultraviolet irradiation of human cornea, lens, and retina: equations of ocular irradiation.* Appl Opt. 1986; 25(3), 359-368.

[400] Citek K. *Anti-reflective coatings reflect ultraviolet radiation.* Optometry. 2008; 79(3), 143-148.

[401] Tuchinda C, Srivannaboon S, Lim HW. *Photoprotection by window glass, automobile glass, and sunglasses.* J Am Acad Dermatol. 2006; 54(5), 845-854.

[402] http://www.sunglasses-shop.co.uk/designer-sunglasses/oakley.asp
(Accessed 18 April 2008)

[403] Dain SJ. *Sunglasses and sunglass standards.* Clin Exp Optom. 2003; 86(2), 77-90.

[404] Rosenthal FS, Bakalian AE, Taylor HR. *The effect of prescription-eyewear on ocular exposure to ultraviolet radiation.* Am J Public Health. 1986; 76(10), 1216–1220.

[405] Sheedy JE, Edlich RF. *Ultraviolet eye radiation: the problem and solutions.* J Long Term Eff Med Implants. 2004; 14(1), 67-71.

[406] Sakamoto Y, Kojima M, Sasaki K. *Effectiveness of eyeglasses for protection against ultraviolet rays.* Jpn. J Ophthalmol. 1999; 43(6), 566-567.

[407] Vajdic CM, Kricker A, Giblin M, McKenzie J, Aitken J, Giles GG, Armstrong BK. *Sun exposure predicts risk of ocular melanoma in Australia.* Int J Cancer. 2002; 101(2), 175-182.

[408] Walsh JE, Koehler LV, Fleming DP, Bergmanson JPG. *Novel method for determining hydrogel and silicone hydrogel contact lens transmission curves and their spatially specific ultraviolet radiation protection factors.* Eye Contact Lens. 2007; 33(2), 58-64.

[409] Webb AR. *UV instrumentation for field and forest research.* Agric For Meteorol. 1993; 120(1-4), 27-38.

[410] Sydenham MM, Collins MJ, Hirst LW. *Measurement of ultraviolet radiation at the surface of the eye.* Invest Ophthalmol Vis Sci. 1997; 38(8):1485-1492.

[411] Diffey BL, Tate TJ, Davis A. *Solar dosimetry of the face: the relationship of natural ultraviolet radiation exposure to basal cell carcinoma localisation.* Phys Med Biol. 1979; 24(5), 931-939.

[412] Rosenthal FS, Safran M, Taylor HR. *The ocular dose of ultraviolet radiation from sunlight exposure.* Photochem Photobiol. 1985; 42(2), 163-171.

[413] Rosenthal FS, Phoon C, Bakalian AE and Taylor HR. *The ocular dose of ultraviolet radiation to outdoor workers.* Invest Ophthalmol Vis Sci. 1988; 29(4), 649-656

[414] Gies P, Javorniczky J, Roy C, Henderson S. *Measurements of the UVR protection provided by hats used at school.* Photochem Photobiol. 2006; 82(3), 750-754.

[415] Kimlin M, Parisi A. *Usage of real-time ultraviolet radiation data to modify the daily erythemal exposure of primary schoolchildren.* Photodermatol Photoimmunol Photomed. 2001; 17(3), 130-135.

[416] Downs N, Parisi A. *Three dimensional visualisation of human facial exposure to solar ultraviolet.* Photochem Photobiol Sci. 2007; 6(1), 90-98.

[417] Guy C, Diab R, Martincigh B. *Ultraviolet radiation exposure of children and adolescents in Durban, South Africa.* Photochem Photobiol. 2003; 77(3), 265-270.

[418] Gies P, Wright J. *Measured solar ultraviolet radiation exposures of outdoors workers in Queensland in the building and construction industry.* Photochem Photobiol. 2003; 78(4), 342-348.

[419] McLaren K, Watson W, Sanfilippo P, Collins M, Sydenham M, Hirst L. *Contact Lens Dosimetry of solar ultraviolet radiation.* Clin Exp Optom. 1997; 80(6), 204-210.

[420] Davis A, Deane GH, Diffey BL. *Possible dosimeter for ultraviolet radiation.* Nature. 1976; 261(5556), 169-170.

[421] Parisi AV, Wilson CA. *Pre-vitamin D effective ultraviolet transmission through clothing during simulated wear.* Photodermatol Photoimmunol Photomed. 2005; 21(6), 303-310.

[422] Lindgren G, Diffey BL, Larko O. *Basal cell carcinoma of the eyelids and solar ultraviolet radiation exposure*. Br J Ophthalmol. 1998; 82(12), 1412-1415.

[423] Fleming RA, Wong CF, Thomas BW. *Statistical variation in experiments for measurements of human UV exposure*. SPIE Proc. (Ultraviolet Radiation Hazards). 1994; 2134B, 86-91.

[424] Diffey BL. Ultraviolet Radiation in Medicine. Medical Physics Handbook 11. Bristol, Adam Hilger. 1982.

[425] Knuschke P, Barth J. *Biologically weighted personal UV dosimetry.* J Photochem Photobiol B. 1996; 36(1), 77-83.

[426] Sisto R, Lega D, Militello A. *The calibration of personal dosemeters used for evaluating exposure to solar UV in the workplace.* Radiat Prot Dosimetry. 2001; 97(4), 419-422.

[427] Webb AR. UVB Instrumentation and Applications. Taylor & Francis, UK. 1998.

[428] Kollias N, Baqer A, Sadiq I, Gillies R, Ou-Yang H. *Measurement of solar UVB variations by polysulphone film.* Photochem Photobiol. 2003; 78(3), 220-224.

[429] Driscoll CMH. *Dosimetry Methods for UV Radiation*. Radiat Protect Dosimetry. 1997; 72(3), 217-222.

[430] Webb AR. *Measuring UV radiation: a discussion of dosimeter properties, uses and limitations.* J. Photochem. Photobiol. B. 1995; 31(1-2), 9-13.

[431] Rocco Casale G, Borra M, Colosimo A, Colucci M, Militello A, Siani AM, Sisto R. *Variability among polysulphone calibration curves.* Phys Med Biol. 2006; 51(17), 4413-4427.

[432] Thieden E. *Sun exposure behaviour among subgroups of the Danish population. Based on personal electronic UVR dosimetry and corresponding exposure diaries.* Dan Med Bull. 2008; 55(1), 47-68.

[433] Sliney DH. *Measurement of Photobiological Exposure of Ocular Tissues.* Symposium Abstract: Biologic Effects of Light (No. 41). Photodermatol Photoimmunol Photomed. 2001; 17(3), 138-148.

[434] Krane K. Modern Physics. John Wiley & Sons, Inc. USA, 1983.

[435] Hunt T, Harrison N. *Ultraviolet Radiation: Current Instrumentation and Methodology.* National Physical Laboratory Report COEM 26, Middlesex, UK, 1999.

[436] Atkins P, de Paula J. *Physical chemistry for the life sciences*. Oxford University Press, Oxford, United Kingdom, 2006.

[437] Glickman RD. *Phototoxicity to the Retina: Mechanisms of Damage.* Int J Toxicol. 2002; 21(6), 473-490.

[438] Meschede D. Optics, Light and Lasers: The practical approach to modern aspects of photonics and laser physics. Wiley-VCH. Weinheim, Germany, 2004.

[439] Fischer-Cripps AC. The Physics Companion. IOP Publishing Ltd, UK, 2003.

[440] Band YB. Light and Matter. Electromagnetism, Optics, Spectroscopy and Lasers. John Wiley & Sons Ltd., England, 2006.

[441] Halliday D, Resnick R. Fundamentals of Physics, Third Edition. John Wiley and Sons, Inc. USA 1988.

[442] Smith FG, King TA. Optics and Photonics. An Introduction. John Wiley and Sons Ltd. England, 2000.

[443] Hecht J. Understanding Fiber Optics (4th Ed). Prentice-Hall, USA, 2002

[444] Sliney DH. *Epidemiological studies of sunlight and cataract: the critical factor of ultraviolet exposure geometry*. Ophthalmic Epidemiol. 1994; 1(2), 107-119.

[445] Sliney DH. *UV radiation ocular exposure dosimetry.* J Photochem Photobiol B. 1995; 31(1-2), 69-77.

[446] Sakamoto Y, Kojima M, Emori Y, Sasaki K. *Ultraviolet dosimetry utilizing a mannequin model.* Dev Ophthalmol. 1997; 27, 50-55.

[447] Walsh JE, Bergmanson JPG, Wallace D, Saldaña G, Dempsey H, McEvoy H, Collum LMT. *Quantification of the ultraviolet radiation (UVR) field in the human eye in vivo using novel instrumentation and the potential benefits of the UVR blocking hydrogel contact lens*. Br. J. Ophthalmol. 2001; 85(9), 1080-1085.

[448] McEvoy H, Walsh JE. *Quantification of the UV light field at the human eye.* BSc Thesis, Dublin Institute of Technology, 1999.

[449] Rubinstein MP. *Applications of contact lens devices in the management of corneal disease.* Eye. 2003; 17(8), 872-876.

[450] www.cantor-nissel.co.uk
(Accessed 18 April 2008)

[451] Hill JC, Maske R. *Pathogenesis of pterygium.* Eye. 1989; 3 (Pt. 2), 218-226.

[452] http://www.srrb.noaa.gov/highlights/sunrise/gen.html
(Accessed 18 April 2008)

[453] Robledo L, Soler A. *Estimation of global illuminance on inclined surfaces for clear skies.* Energy Conversion and Management. 2003; 44(15), 2455-2469.

[454] Sliney DH. *Photoprotection of the eye - UV radiation and sunglasses.* J Photochem Photobiol B. 2001; 64(2-3),166-75.

[455] Introduction to Visual Optics. Tunnacliffe, AH. Association of British Dispensing Opticians. 1993.

[456] Westheimer G. *Specifying and controlling the optical image on the human retina.* Prog Retin Eye Res. 2006; 25(1), 19-42.

[457] http://www.oceanoptics.com/Products/dh2000.asp
(Accessed 18 April 2008)

[458] Walsh JE, Kavanagh KY, Fennell S, Murphy J, Harmey M. *Fibre-optic micro-spectrometers for biomedical sensing.* Trans. Meas. Sci. 2000; 22(5), 355-369.

[459] Zuchlich JA. *Ultraviolet induced damage in the primate cornea and retina.* Curr Eye Res. 1984; 3(1), 27-34.

[460] Ambach W, Blumthaler M, Schöpf T, Ambach E, Katzgraber F, Daxecker F, Daxer A. *Spectral transmission of the optical media of the human eye with respect to keratitis and cataract formation.* Doc Ophthalmol. 1994; 88(2), 165-173.

[461] Boettner EA, Wolter JR. *Transmission of the ocular media.* J Investigative Ophthalmology and Visual Science. 1962;1;776-783

[462] McLaren JW, Brubaker RF. *Measurement of transmission of ultraviolet and visible light in the living rabbit cornea.* Curr Eye Res. 1996;15(4), 411-421.

[463] van den Berg TJ, Tan KE. *Light transmittance of the human cornea from 320 to 700 nm for different ages.* Vision Res. 1994; 34(11), 1453–1456.

[464] Merriam JC, Löfgren S, Michael R, Söderberg P, Dillon J, Zheng L, Ayala M. *An action spectrum for UV-B radiation and the rat lens.* Invest Ophthalmol Vis Sci. 2000; 41(9), 2642-2647.

[465] Dillon J, Zheng L, Merriam JC, Gaillard ER. *The optical properties of the anterior segment of the eye: Implications for cortical cataract.* Exp. Eye Res. 1999; 68(6), 785-795.

[466] Walsh JE, Bergmanson JP, Koehler LV, Doughty MJ, Fleming DP, Harmey JH. *Fibre optic spectrophotometry for the in vitro evaluation of ultraviolet radiation (UVR) spectral transmittance of rabbit corneas.* Physiol Meas. 2008; 29(3), 375-388.

Appendix I

G5842 Specs

Appendix II

SPIE paper

Appendix III

RPD paper

Appendix IV

Eye & CL paper

Appendix V

Physiol Meas paper